ABSTRACT

Title of dissertation: ANALYSIS OF FLUCTUATIONS IN SEMICONDUCTOR DEVICES

Petru Andrei, Doctor of Philosophy, 2004

Dissertation directed by: Professor Isaak D. Mayergoyz
Department of Electrical and Computer Engineering

The random nature of ion implantation and diffusion processes as well as inevitable tolerances in fabrication result in random fluctuations of doping concentrations and oxide thickness in semiconductor devices. These fluctuations are especially pronounced in ultrasmall (nanoscale) semiconductor devices when the spatial scale of doping and oxide thickness variations become comparable with the geometric dimensions of devices. In the disseration, the effects of these fluctuations on device characteristics are analyzed by using a new technique for the analysis of random doping and oxide thickness induced fluctuations. This technique is universal in nature in the sense that it is applicable to any transport model (drift-diffusion, semiclassical transport, quantum transport etc.) and it can be naturally extended to take into account random fluctuations of the oxide (trapped) charges and channel length.

The technique is based on linearization of the transport equations with respect to the fluctuating quantities. It is computationally much (a few orders of magnitude) more efficient than the traditional Monte-Carlo approach and it yields information on the sensitivity of fluctuations of parameters of interest (e.g. threshold voltage, small-signal parameters, cut-off frequencies, etc.) to the locations of doping and oxide thickness fluctuations. For this reason, it can be very instrumental in the design of fluctuation-resistant structures of semiconductor devices.

Quantum mechanical effects are taken into account by using the density-gradient model as well as through self-consistent Poisson-Schrödinger computations. Special attention is paid to the presenting of the technique in a form that is suitable for implementation on commercial device simulators. The numerical implementation of the technique is discussed in detail and numerous computational results are presented and compared with those previously published in literature.

ANALYSIS OF FLUCTUATIONS IN

SEMICONDUCTOR DEVICES

by

Petru Andrei

Dissertation submitted to the Faculty of Graduate School of the
University of Maryland, College Park in partial fulfillment
of the requirements for the degree of
Doctor of Philosophy
2004

Advisory Committee:

Professor Isaak D. Mayergoyz, Chair
Professor Martin C. Peckerar
Assistant Professor Reza Ghodssi
Professor Perinkulam S. Krishnaprasad
Professor Howard C. Elman

DEDICATION

To my loving mother

and

to my wife

ACKNOWLEDGEMENTS

I would like to thank Prof. Isaak D. Mayergoyz, who introduced me to the challenging field of semiconductor device modeling and who proposed the main idea and the general outline of the technique of analysis of fluctuations in semiconductor devices, which is developed in this dissertation. He encouraged me to work my way through the fascinating subject of semiconductor physics and gave me the possibility to write my dissertation in this area. I would also like to thank him for guiding me through and spending a lot of time supporting me.

I also wish to thank the professors who taught and encouraged me during my studies: Prof. Martin Peckerar for his advice and discussions concerning semiconductor device physics, Profs. Alexandru Stancu and Hans Hauser for guiding me during my B.S. and M.S. degrees, and Prof. Iulian Leahu for the love and devotion he gave me for physics and science in general.

I would also like to thank the committee members for my dissertation defense, Professors Isaak D. Mayegoyz, Martin C. Peckerar, Reza Ghodssi, Perinkulam S. Krishnaprasad, and Howard C. Elman for their time and effort in reviewing my dissertation.

Thanks to my family and friends, who morally supported me during this long journey. I would like to extend a loving thank to my wife, Simona. Though we lived

apart for such a long time, you have been there for me and helped me whenever I needed. Thank you so very, very much.

College Park, February 2004

Petru Andrei

TABLE OF CONTENTS

LIST OF TABLES

LIST OF FIGURES

Chapter 1

Introduction

The continuous demand for high operating frequencies and low power consumption makes the semiconductor industry move towards smaller and smaller device dimensions [1], [2]. However, the reduction of the minimum feature size of semiconductor devices is accompanied by numerous technological problems that need to be overcome for further progress in the areas of Very-Large-Scale-Integration (VLSI) and Ultra-Large-Scale-Integration (ULSI) circuits [3]-[8]. Such a problem that has become increasingly important in the last years is related to the random doping and geometric dimensions induced fluctuations in ultrasmall semiconductor devices. The goal of this dissertation is to present a new and fast method for the analysis of these fluctuations. The numerical techniques developed throughout the dissertation can be easily implemented on commercial device simulators and be used for the design of fluctuation-resistant structures of semiconductor devices.

1.1 Statement and importance of the problem

It has been observed that the parameters of ultrasmall semiconductor devices (threshold voltages, gain factors, cut-off frequencies, etc.) fluctuate appreciably from one device to another. These fluctuations are due to the fact that it is very difficult, if not impossible, to fabricate devices that have the same atomic configuration. In ideal devices, the doping concentration should be controlled with maximum precision, the junctions and semiconductor/oxide interfaces should be perfectly defined, and the interface and fixed oxide charges should be negligible or very well localized and measured. However, none of these problems can be completely solved during the fabrication process:

a) Due to the stochastic nature of ion implantation and diffusion processes, the doping locations and concentrations cannot be exactly controlled and, consequently, the doping profiles of the devices are not identical. For example, in a uniformly doped MOSFET with channel length and width of 50 nm and dopant concentration of 10^{18} cm^{-3}, the average number of dopant atoms in the depletion region is approximately $N = 100$. The actual number fluctuates from device to device, with standard deviation $\sigma_N = \sqrt{N} = 10$, which represents a significant fraction of the average number N [see Figure 1.1 (a)]. The fluctuations of the total number of dopant atoms translate into fluctuations of device parameters (threshold voltage, terminal characteristics, etc.) that affect have a negative effect on the reliability and yield of VLSI and ULSI circuits [9]-[19].

b) The geometrical lengths of semiconductor devices (channel length, oxide thickness, device width, etc.) also fluctuate due to the inaccuracy of lithography techniques and oxide growing processes [Figure 1.1 (b)]. The surfaces of the semiconductor-oxide interfaces are not perfectly flat and they are characterized by an intrinsic roughness with an autocorrelation length that depends on the fabrication process [20]-[32]. Even for very carefully grown oxide layers, the roughness of the oxide surface is approximately 0.2 nm, which represents a significant fraction of the average oxide thickness that can be as low as 2 nm in modern MOSFET device.

c) The gate polysilicon line edge roughness (LER) is caused by tolerances in the lithography and etching processes and is considered to place significant limits on further scaling of the devices [33]-[41]. The edge roughness is typically on the order of 5 nm almost independently of the type of lithography used in production and represents an important fraction of the gate length in ultrasmall devices. LER (also known as gate patterning) affects most device parameters such as threshold voltage and terminal currents.

d) The fixed and interface charges are very difficult to control during the fabrication processes and seem to be strongly correlated with the aspect and irregularities of the oxide-semiconductor interface. Individual interface defects near the silicon/oxide interface can cause trapping of carrier charges and local modulation of mobility and channel conductance, which result in fluctuations of the gate and drain currents [42]-[56]. These fluctuations are usually called

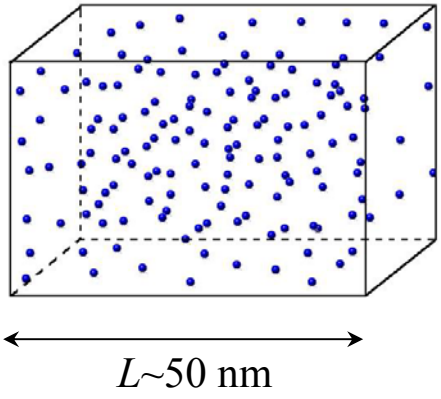

(a)

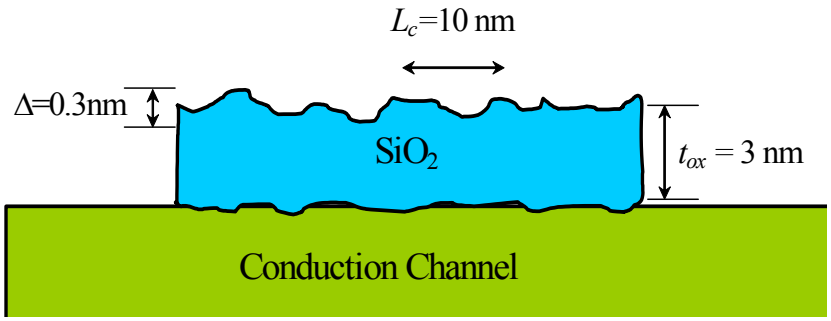

(b)

Figure 1.1: Due to the stochastic nature of diffusion and implantation processes the doping concentration is a random variable (a). The roughness of the oxide surfaces and the irregularities of the interfaces can be characterized by roughness Δ and correlation length L_c.

random telegraph signals (RTS) and have a great impact on the stability of analog and digital circuits.

In addition to the aforementioned effects, one should take into consideration the oxide permittivity fluctuations, as well as the dislocations and irregularities of the semiconductor lattice. All these fluctuations and defects affect the threshold voltages and the frequency characteristics of devices.

Random fluctuations in semiconductor devices are especially pronounced in small devices, where the spatial scales of these fluctuations are comparable with the characteristic dimensions of the devices. For example, in the case of large metal-oxide-semiconductor field-effects transistor (MOSFET) devices (i.e. with channel length larger than 1 μm), random doping fluctuations are averaged out by the large volume of the semiconductor device and their effects can be neglected in most applications. However, for small devices (i.e. with channel length of the order of hundreds or tens of nanometers), the position and concentration of dopant atoms strongly influence the values of intrinsic parameters of the MOSFET. Similarly, random oxide roughness induced fluctuations are not important for devices with thick oxide layers (in which the oxide thickness is at least one order of magnitude larger than the oxide roughness), but can affect the functionality of the devices with thin oxide layers.

The fluctuations of threshold voltages and terminal characteristics can be critical for the proper functioning of analog circuits [57]-[60]. For example, in differential low-noise amplifiers, a mismatch of 1% of the characteristics of input transistors can make the amplifiers nonoperational. In digital circuits, the fluctuations of threshold

voltages should be as small as possible in order to improve the static noise margins (SNM) of logic circuits. Large fluctuations of threshold voltages would lead to the deterioration of the SNM for static random-access memory (SRAM) and read-only memory (ROM) cells and would strongly decrease the reliability of complimentary metal-oxide semiconductor (CMOS) gates [61]-[64]. Given the importance of random doping and random geometrical dimensions induced effects, an accurate analysis of fluctuations in ultrasmall semiconductor devices is very important for further progress in the area of semiconductor device technology.

1.2 Current state of research

There are few methods for the analysis of fluctuations in semiconductor devices. Most of these methods are based on the statistical (Monte-Carlo) technique and their basic idea and limitations are presented in the following subsections.

1.2.1 The Monte-Carlo methods

The existing techniques for the analysis of fluctuations in ultrasmall semiconductor devices [65]-[71] are based on generating numerous random realizations (samples) and solving the transport equations for each such realization. In this way, statistics of physical parameters of interest are accumulated and then used for the evaluation of variances of those parameters. These techniques (known as the Monte-Carlo techniques) are purely statistical in nature and, therefore, computationally very expensive and subject to statistical errors. To illustrate this fact, consider the

computation of the standard deviation of some parameter A of the device. For example, this parameter can be the threshold voltage or the subthreshold current of a MOSFET device, the current, the gain factor, or the cut-off frequency of a BJT device. If we compute the values of parameter A for each individual device and denote them by A_i, the average value of A can be calculated by using the formula:

$$\langle A \rangle = \frac{\sum_{i=1}^{N} A_i}{N}, \tag{1.1}$$

where N is the total number of devices simulated. The standard deviation of parameter A can be estimated by using:

$$\sigma_A = \sqrt{\frac{\sum_{i=1}^{N} \left(A_i - \langle A \rangle \right)^2}{N-1}} \tag{1.2}$$

The accuracy in the computation of the standard deviation depends on the total number of realizations N. It can be shown that the values A_i are distributed approximately according to a Gaussian distribution function and the relative error in the computation of σ_A by using formula (1.2) is $1/\sqrt{2N}$. Table 1.1 presents the dependence of the relative error in the estimation of σ_A with formula (1.2) on the total number of samples simulated. We can see that the total number of samples N increases considerably if high accuracy in the computation of σ_A is required. Usually, N = 200 devices are simulated and the values of the standard deviations are reported with a relative error of 5%.

Another parameter of interest that characterizes the distribution of A_i is the "shift" of parameter A, which is defined as:

$$\Delta A = A_0 - \langle A \rangle . \tag{1.3}$$

In the last equation, A_0 is the value of A computed by assuming that the doping concentration and geometric lengths are constant and equal to their average values. It is worthwhile noticing that the origin of the shift ΔA is the nonlinearity of the transport equations and it can have either positive or negative values.

The Monte-Carlo methods have been applied extensively to the computation of standard deviations and shifts of parameters in semiconductor devices. Most of the work done in the past has focused on the computation of the standard deviation of threshold voltage [10], [13], [30], [32], [65]-[71] and capacitances [72] in MOSFET devices.

Number of devices simulated (N)	Relative error in the estimation of σ_A
50	10%
200	5%
500	3.2%
1000	2.2%
5000	1%

Table 1.1: Relative errors in the determination of σ_A as a function of the total number of devices simulated. The calculations are done by using formula (1.2).

1.2.2 Limitations of the Monte-Carlo methods

The Monte-Carlo methods have certain disadvantages and limitations that reduce considerably the area of applicability of these techniques:

a) These methods are computationally very expensive since the same device-level simulations have to be performed many times. The total computation time for the Monte-Carlo methods increases linearly with the total number of devices simulated and can be very long if high accuracy of final results is required. For instance, if the time for the computation of frequency characteristics of a 3–dimensional (3-D) MOSFET is about one hour, it follows that the total time for simulating 200 devices is of the order of weeks. This time is impractically long for normal applications. For this reason, the Monte-Carlo methods have mostly been used for the calculation of fluctuations of threshold voltages and not too much effort has been paid to the analysis of fluctuations of more complex parameters, such as small-signal parameters and cut-off frequencies.

b) The Monte-Carlo methods are subject to statistical errors. As we can see from Table 1.1, these errors are relatively large if a small number of devices are simulated. Errors can be reduced solely by increasing the total number of devices simulated, which results in even longer computation times.

c) The computation of shift ΔA is subject to large numerical errors because it is obtained by extracting a quantity from another close quantity that cannot be computed accurately [see equation (1.3)]. Hence, the values of the threshold voltage shifts published in literature do not agree even as order of magnitude.

d) The process of generating different devices for the Monte-Carlo methods is rather complicated. For example, in the case of random oxide roughness induced fluctuations in MOSFET devices, the mechanism for generating the semiconductor/oxide interfaces involves the inverse Fourier transform of the power spectrum of the autocorrelation function (ACF) of oxide thickness fluctuations. This approach is appropriate for sufficiently "smooth" ACFs (like the Gaussian ACF), but unsuitable for more realistic ACFs (like the exponential ACF), because of the high frequency content in the power spectrum.

e) The doping distributions of randomly generated devices are usually highly irregular in space and very fine meshes are needed to resolve the fast spatial doping fluctuations. This fact further increases the computation time for each individual device.

The aforementioned drawbacks can be overcome by increasing the total computation time for simulations. Since the Monte-Carlo methods are computationally very expensive, they have been implemented mostly on multiprocessor systems by using parallel programming techniques.

In this dissertation, an entirely different approach to the evaluation of variances of intrinsic device parameters is developed [73]-[80]. This approach, henceforth referred as the linearization approach, is based on linearization of the transport equations and completely circumvents the calculations for numerous devices. It requires only the knowledge of variances of fluctuating doping concentrations and, in this sense, it is a "second-moment characterization" technique. As a result, this

technique is computationally much more efficient than the Monte-Carlo methods. In addition, it yields the information on sensitivity of the variances of the physical quantities of interest to doping locations. For these reasons, the linearization technique can be instrumental in the design of fluctuation-resistant structures of semiconductor devices.

1.3 Outline

This dissertation is organized as follows. Chapter 2 presents the basic idea of the new technique for the analysis of fluctuations in semiconductor devices. Special attention is paid to the computation of standard deviations of threshold voltages in ultrasmall MOSFET devices induced by random doping and random oxide roughness fluctuations. Numerous numerical results are presented and compared with results obtained by other authors with the Monte-Carlo methods.

The linearization technique presented in Chapter 2 is adjusted in Chapter 3 to the computation of the standard deviation of I-V characteristics and transconductance. In the last part of this chapter, the algebra of superposition coefficients is developed and used to compute the fluctuations of subthreshold voltage characteristics (gate-voltage swing) of MOSFET devices.

Chapter 4 extends the techniques presented in the previous chapter to the analysis of fluctuations of frequency characteristics of semiconductor devices. The first part of the chapter focuses on the analysis of fluctuations of admittance matrix parameters (y-parameters). The algebra of superposition coefficients is then used for

the computation of variances of other small signal parameters such as *h*, *z*, *g*-parameters, current and voltage gains, maximum available and unilateral gains, and cut-off frequencies.

Chapter 5 presents a detailed analysis of the quantum mechanical induced effects on the fluctuations in semiconductor devices. Two different approaches are used for the computation of standard deviations of different parameters. In the first part of the chapter, standard deviations are computed by using the first-order perturbation technique of the Schrödinger equation. In the second part, standard deviations are determined with the Density-Gradient model that is carefully calibrated against self-consistent Poisson-Schrödinger calculations. Numerous numerical results are presented and compared with classical computations.

Finally, conclusions and further work are presented in Chapter 6.

Chapter 2

Analysis of fluctuations of threshold voltages

In this chapter we present the linearization technique for the analysis of fluctuations in semiconductor devices. The first part of the chapter presents the fundamentals of the method for the calculation of the standard deviation of threshold voltage V_T in MOSFET devices. Two definitions of threshold voltage are considered in this analysis: the "current" definition (Sections 2.1 and 2.2) and the "complete inversion" definition of threshold voltage (Section 2.3). The shift of threshold voltage is discussed in Section 2.4. Finally, different methods for the suppression of fluctuations of threshold voltage in MOSFET devices are presented in Section 2.5.

2.1 Linearization technique for the analysis of fluctuations in semiconductor devices

In this section we present the basic idea of the method for the computation of the fluctuations induced by random doping and oxide thickness fluctuations in MOSFET devices. We focus mainly on the computation of fluctuations of threshold voltage, but

the same basic idea can be applied to the computation of other fluctuating parameters in semiconductor devices, such as currents, small-signal parameters, and cut-off frequencies. Special consideration is given to presenting the method in matrix form, which makes it suitable for numerical implementation on standard semiconductor device simulators. Throughout this section we adopt the "current definition" of the threshold voltage [81], whereby V_T is defined as the gate potential for which the drain to source current is $I_T = 10^{-8} W/L$, where W and L are the channel width and length, respectively.

2.1.1 General considerations

In general, threshold voltage can be written as a function of doping concentration $\boldsymbol{D}$ and oxide thickness $\boldsymbol{t}$:

$$V_T = V_T(\boldsymbol{D}, \boldsymbol{t}). \tag{2.1}$$

In equation (2.1), we have considered that the doping concentration is a function of position. Hence, if the region of the semiconductor device is spatially discretized into N cells, the doping concentration must be specified as an N-dimensional column vector $\boldsymbol{D}$:

$$\boldsymbol{D} = \begin{bmatrix} D_1 \\ D_2 \\ \cdots \\ D_N \end{bmatrix}. \tag{2.2}$$

Similar observations apply to the oxide thickness $\boldsymbol{t}$, which can be written as a column vector whose components are the local values of the oxide thickness at different locations on the semiconductor-oxide interface (see Figure 2.1):

$$\boldsymbol{t} = \begin{bmatrix} t_1 \\ t_2 \\ \dots \\ t_{N_{OX}} \end{bmatrix}. \tag{2.3}$$

However, the dimension of vector $\boldsymbol{t}$ [which is denoted by N_{OX} in equation (2.3)] is usually much smaller than the dimension of the doping vector, because the oxide region usually contains less discretization points than the semiconductor region.

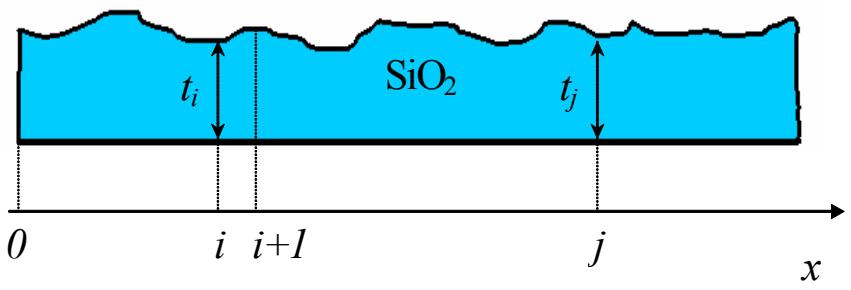

Figure 2.1: Cross-section through the oxide layer.

The doping concentration and the oxide thickness are random quantities and can be written as the sum of their respective average values ($\boldsymbol{D}_0$ and $\boldsymbol{t}_0$) and fluctuations ($\tilde{\boldsymbol{D}}$ and $\tilde{\boldsymbol{t}}$):

$$\boldsymbol{D} = \boldsymbol{D}_0 + \tilde{\boldsymbol{D}} \tag{2.4}$$

and

$$\boldsymbol{t} = \boldsymbol{t_0} + \tilde{\boldsymbol{t}}\,, \tag{2.5}$$

where by definition, the expected values of $\tilde{\boldsymbol{D}}$ and $\tilde{\boldsymbol{t}}$ are equal to zero. The basic idea for the computation of threshold voltage fluctuations is to linearize equation (2.1) with respect to the fluctuating quantities. In the first-order approximation, the fluctuations of threshold voltage can be written as follows:

$$\tilde{V}_T = \frac{\partial V_T}{\partial \boldsymbol{D}}\tilde{\boldsymbol{D}} + \frac{\partial V_T}{\partial \boldsymbol{t}}\tilde{\boldsymbol{t}} = \sum_i \gamma_{V_T}^{D_i}\tilde{D}_i + \sum_j \gamma_{V_T}^{t_j}\tilde{t}_j\,, \tag{2.6}$$

where $\gamma_{V_T}^{D_i} = \dfrac{\partial V_T}{\partial D_i}$ and $\gamma_{V_T}^{t_j} = \dfrac{\partial V_T}{\partial t_j}$ are the so-called doping and oxide thickness superposition coefficients. These coefficients show how sensitive the threshold voltage is to the fluctuations of doping concentration and oxide thickness at specific locations in the device. It is customary to assume that the doping densities at different locations are independent random variables. This allows us to derive the following expression for the variance of the threshold voltage:

$$\sigma_{V_T}^2 = \sum_i \left(\gamma_{V_T}^{D_i}\right)^2 \sigma_{D_i}^2 + \sum_{i,j} \gamma_{V_T}^{t_i}\gamma_{V_T}^{t_j} ACF\left(i,j\right), \tag{2.7}$$

where $\sigma_{D_i}^2$ represents the variance of D_i and $ACF\left(i,j\right)$ is the autocorrelation function of the oxide thickness, which is defined as follows:

$$ACF\left(i,j\right) = \left\langle \left(t_i - \left\langle t_i \right\rangle\right)\cdot\left(t_j - \left\langle t_i \right\rangle\right)\right\rangle = \left\langle \tilde{t}_i \cdot \tilde{t}_j \right\rangle, \tag{2.8}$$

where $\langle t \rangle$ stands for the average oxide thickness. This function can be measured directly by using atomic force microscopy experiments [21]-[24]. In most cases, $ACF(i,j)$ is approximated by an exponential or Gaussian distribution function.

As we proceed to determine $\sigma_{D_i}^2$, let us remark that the total number N_i of dopant atoms in the *i*th discretization cell of volume ΔV_i is a random variable with Poisson distribution; the rationale behind this assumption will be provided later on in this section. In the case of Poisson distributions, the expected value and the variance coincide. Hence, we have:

$$\sigma_{N_i}^2 = N_{0i} = D_{0i}\Delta V_i, \tag{2.9}$$

where, D_{0i} is the average doping concentration in volume ΔV_i. By using this fact, we derive:

$$\sigma_{D_i}^2 = \left(\frac{1}{\Delta V_i}\right)^2 \sigma_{N_i}^2 = \frac{D_{0i}}{\Delta V_i}. \tag{2.10}$$

By using equations (2.7) and (2.10), the variance of the threshold voltage can now be computed as follows:

$$\boxed{\sigma_{V_T}^2 = \sum_i \left(\gamma_{V_T}^{D_i}\right)^2 \frac{D_{0i}}{\Delta V_i} + \sum_{i,j} \gamma_{V_T}^{t_i} \gamma_{V_T}^{t_j} ACF(i,j)}. \tag{2.11}$$

Thus, the problem of computing threshold voltage variance is reduced to the computation of superposition coefficients. It is important to note that the effects of random doping fluctuations can be separated in formula (2.11) from the effects of random oxide thickness fluctuations. If we denote the variance of V_T induced by

random doping fluctuations by $\sigma^2_{V_T}[DF]$ and the variance of V_T induced by random oxide thickness fluctuations by $\sigma^2_{V_T}[OTF]$, we can write:

$$\sigma^2_{V_T} = \sigma^2_{V_T}[DF] + \sigma^2_{V_T}[OTF]. \tag{2.12}$$

The first term is related to the fluctuations of the doping concentration, while the second term is related to the fluctuations of the oxide thickness. The two terms are uncorrelated in the first-order approximation. This fact was also observed by Asenov *et al*. [41] by performing a large number of simulations for devices with different oxide thickness and doping distributions.

It should be noted that the superposition coefficients are mesh dependent. Therefore, it is convenient to introduce the doping ($S^{D_i}_{V_T}$) and oxide thickness ($S^{t_i}_{V_T}$) "sensitivity coefficients," which are defined as:

$$S^{D_i}_{V_T} = \left(\frac{\gamma^{D_i}_{V_T}}{\Delta V_i} \right)^2 \tag{2.13}$$

and

$$S^{t_i}_{V_T} = \left(\frac{\gamma^{t_i}_{V_T}}{\Delta S_i} \right)^2, \tag{2.14}$$

respectively. In formula (2.14), ΔS_i is the transversal area of the ith discretization cell on the oxide/semiconductor interface. Equation (2.11) now reads as follows:

$$\sigma^2_{V_T} = \sum_i \left(S^{D_i}_{V_T} \right)^2 D_{0i} \Delta V_i + \sum_{i,j} S^{t_i}_{V_T} S^{t_j}_{V_T} \Delta S_i \Delta S_j ACF(i,j). \tag{2.15}$$

The Poisson distribution of the number of dopant atoms $N_{i,j}$ in volume $\Delta V_{i,j}$ can be justified by using the following reasoning. Let $n_{i,j}$ be the total number of sites

available for occupation by dopant atoms in volume $\Delta V_{i,j}$ and let p be the probability of occupation of each of these sites. It is assumed that the doping process is such that this probability is the same for all sites. It follows that $N_{i,j}$ is a random variable with binomial distribution. If the occupation probability p is relatively small, while the total number $n_{i,j}$ of available sites is very large and the product $pn_{i,j} \gg 1$, the binomial distribution can be approximated quite accurately by the Poisson distribution. In the case of very small volumes $\Delta V_{i,j}$, when the assumption of very large $n_{i,j}$ does not hold, the binomial distribution for $N_{i,j}$ should be used instead of the Poisson distribution. According to the binomial distribution, we have:

$$\sigma^2_{N_{i,j}} = N^0_{i,j}(1-p) = D^0_{i,j}\Delta V_{i,j}(1-p), \tag{2.16}$$

where the occupation probability p can be deduced from the expression $N^0_{i,j} = n_{i,j}p$. As a result, factor $(1-p)$ will appear in (2.9)-(2.11). However, $n_{i,j}$ is usually much larger than $N^0_{i,j}$ and, consequently, p is rather small. Therefore, (2.16) reduces to formula (2.9).

Finally, it should be noted that equations similar to (2.1)-(2.16) can be written for most of the other fluctuating parameters of semiconductor devices. If by A we denote some generic parameter of the device (e.g. saturation current, cut-off frequency, transconductance, etc), then the fluctuations of this parameter can be written as linear functions of the doping and oxide thickness fluctuations:

$$\tilde{A} = \frac{\partial A}{\partial \boldsymbol{D}}\tilde{\boldsymbol{D}} + \frac{\partial A}{\partial \boldsymbol{t}}\tilde{\boldsymbol{t}} = \sum_i \gamma_A^{D_i}\tilde{D}_i + \sum_j \gamma_A^{t_j}\tilde{t}_j\,, \tag{2.17}$$

where $\gamma_A^{D_i}$ and $\gamma_A^{t_i}$ are the doping and oxide thickness superposition coefficients of A. The variance of parameter A can be computed by using the more general equation:

$$\sigma_A^2 = \sum_i \left(\gamma_A^{D_i}\right)^2 \frac{D_{0i}}{\Delta V_i} + \sum_{i,j} \gamma_A^{t_i} \gamma_A^{t_j} ACF(i,j). \tag{2.18}$$

2.1.2 Computation of superposition coefficients

As stated in the previous section, σ_{V_T} can be computed directly if we know the values of the superposition coefficients. Hence, next we introduce the method for the computation of threshold voltage superposition coefficients. In order to make it suitable for numerical implementation on standard semiconductor device simulators, this method is presented in compact matrix form.

For the sake of brevity, the discretized transport equations are written in vector form [82]:

$$\boldsymbol{F}(\boldsymbol{X}, \boldsymbol{D}, \boldsymbol{t}, V_G) = 0, \tag{2.19}$$

where $\boldsymbol{F}$ is a nonlinear vector function of the unknown "state" vector $\boldsymbol{X}$, vectors $\boldsymbol{D}$ and $\boldsymbol{t}$, as well as gate voltage V_G. If the transport model is the drift-diffusion model, the state vector can be written as follows:

$$\boldsymbol{X} = \begin{bmatrix} \boldsymbol{\varphi} \\ \boldsymbol{n} \\ \boldsymbol{p} \end{bmatrix}, \tag{2.20}$$

where $\boldsymbol{\varphi}$ is the vector of mesh-point values of the electric potential, while $\boldsymbol{n}$ and $\boldsymbol{p}$ are the vectors of mesh-point values of the electron and hole densities, respectively. If

the transport model is the Density-Gradient (DG) model, the expression for the state vector is:

$$\boldsymbol{X} = \begin{bmatrix} \boldsymbol{\varphi} \\ \boldsymbol{n} \\ \boldsymbol{p} \\ \boldsymbol{\psi}_n \\ \boldsymbol{\psi}_p \end{bmatrix}, \tag{2.21}$$

where $\boldsymbol{\varphi}$, $\boldsymbol{n}$, and $\boldsymbol{p}$ have the same meaning as before and $\boldsymbol{\psi}_n$ and $\boldsymbol{\psi}_p$ are the quasi-Fermi potentials. Finally, if the Poisson-Schrödinger equations are used to describe the statistics in the semiconductor device, the state vector has the form:

$$\boldsymbol{X} = \begin{bmatrix} \boldsymbol{\varphi} \\ E_1 \\ \dots \\ E_l \\ \dots \\ \boldsymbol{\Psi}_1 \\ \dots \\ \boldsymbol{\Psi}_l \\ \dots \end{bmatrix}, \tag{2.22}$$

where $E_1, \dots\ E_l, \dots$ are the energy eigenvalues and $\boldsymbol{\Psi}_1, \dots\ \boldsymbol{\Psi}_l, \dots$ are the energy eigenvectors of the Hamiltonian operator.

If $\tilde{\boldsymbol{X}}$ denotes the fluctuations of the state variable and $\tilde{V}_G$ the fluctuations of the gate potential, in the first-order approximation we can write:

$$\hat{\boldsymbol{F}}_{\boldsymbol{X}}\tilde{\boldsymbol{X}} + \hat{\boldsymbol{F}}_{\boldsymbol{D}}\tilde{\boldsymbol{D}} + \hat{\boldsymbol{F}}_{\boldsymbol{t}}\tilde{\boldsymbol{t}} + \boldsymbol{F}_{V_G}\tilde{V}_G = 0, \tag{2.23}$$

where $\hat{\boldsymbol{F}}_{\boldsymbol{X}}$, $\hat{\boldsymbol{F}}_{\boldsymbol{D}}$, $\hat{\boldsymbol{F}}_{\boldsymbol{t}}$, and $\boldsymbol{F}_{V_G}$ are the derivatives of $\boldsymbol{F}$ with respect to $\boldsymbol{X}$, $\boldsymbol{D}$, $\boldsymbol{t}$, and V_G, respectively. All derivatives are computed at the given dc bias point and by assuming

constant (non-fluctuating) values of the doping concentration and oxide thickness. The drain current can also be written as a function of the state vector and doping concentration:

$$I = I\left(\boldsymbol{X}\right). \tag{2.24}$$

At threshold voltage the drain current is constant and we have:

$$0 = \tilde{I} = I_{\boldsymbol{X}}^{t}\tilde{\boldsymbol{X}}\,, \tag{2.25}$$

where $I_{\boldsymbol{X}}^{t}$ is the transpose of the gradient of I with respect to $\boldsymbol{X}$. Equations (2.23) and (2.25) are coupled equations with unknowns $\tilde{\boldsymbol{X}}$ and $\tilde{V}_T = \tilde{V}_G$. In order to decouple them, we multiply equation (2.23) from the left by $I_{\boldsymbol{D}}\hat{\boldsymbol{F}}_{\boldsymbol{X}}^{-1}$ and use the constraint (2.25). After a few rearrangements we obtain the following equation for the fluctuations of threshold voltage:

$$\tilde{V}_T = -\frac{\boldsymbol{g}^t \cdot \hat{\boldsymbol{F}}_{\boldsymbol{D}}}{\boldsymbol{g}^t \cdot \boldsymbol{F}_{V_G}} \cdot \tilde{\boldsymbol{D}} - \frac{\boldsymbol{g}^t \cdot \hat{\boldsymbol{F}}_{\boldsymbol{t}}}{\boldsymbol{g}^t \cdot \boldsymbol{F}_{V_G}} \cdot \tilde{\boldsymbol{t}}\,, \tag{2.26}$$

where $\boldsymbol{g}^t$ is the transpose of column vector $\boldsymbol{g}$, which is the solution of the following linear system of equations:

$$\hat{\boldsymbol{F}}_{\boldsymbol{X}}^{t}\boldsymbol{g} = I_{\boldsymbol{X}}\,, \tag{2.27}$$

where $\hat{\boldsymbol{F}}_{\boldsymbol{X}}^{t}$ denotes the transpose of matrix $\hat{\boldsymbol{F}}_{\boldsymbol{X}}$. By comparing equations (2.6) and (2.26) it can be inferred that the superposition coefficients of the threshold voltage are given by the equations:

$$\gamma_{V_T}^{D_i} = -\frac{\left(\boldsymbol{g}^t \cdot \hat{\boldsymbol{F}}_{\boldsymbol{D}}\right)_i}{\boldsymbol{g}^t \cdot \boldsymbol{F}_{V_G}} \tag{2.28}$$

and

$$\gamma_{V_T}^{t_j} = -\frac{\left(\boldsymbol{g}^t \cdot \hat{\boldsymbol{F}}_{\boldsymbol{t}}\right)_j}{\boldsymbol{g}^t \cdot \boldsymbol{F}_{V_G}}. \tag{2.29}$$

The most expensive computational task related to the calculation of these coefficients is to solve linear system (2.27). For 2-D simulations this system can be solved numerically by using the classical Gauss-Seidel method [83], [84]. However, for 3-D simulations the computation time and memory requirements would increase considerably if the Gauss-Seidel method is used, so other procedures are needed to solve (2.27). In our simulations, we took advantage of the diagonal dominance of matrix $\hat{\boldsymbol{F}}_{\boldsymbol{X}}$ and we solved it efficiently by using the Successive Over-Relaxation (SOR) method.

As far as the numerical implementation of the method is concerned, it is important to note that most of the matrices and vectors in (2.26) and (2.27) are sparse and their elements can be computed easily. For example, most of the components of vector $\boldsymbol{F}_{V_G}$ in (2.26) are equal to zero because $\boldsymbol{F}$ has only few equations which are related to V_G (usually these equations result from the discretization of the boundary conditions in the transport equations). The same observation can be made about the elements of matrix $\hat{\boldsymbol{F}}_{\boldsymbol{t}}$, since the oxide discretization region contains a small number of mesh-points compared with the semiconductor discretization region. Matrix $\hat{\boldsymbol{F}}_{\boldsymbol{D}}$ can also be computed easily because, at room temperature, the doping enters linearly in the Poisson equations.

2.2 Analysis of fluctuations of the threshold voltage by using the "current" definition

The technique presented in the previous section was numerically implemented and used to compute the fluctuations of V_T devices induced by the random doping and random oxide roughness in MOSFET. In this section we report the numerical results obtained by using this technique and compare them with results previously published in literature [66], [68]. These two papers have been selected for comparison because they report the results of the most extensive numerical simulations performed by using purely statistical approaches. Throughout the simulations, the classical drift-diffusion model is used; the transport equations are discretized by using the finite difference scheme.

In the first-order approximation, the threshold voltage fluctuations induced by doping fluctuations are independent of those induced by random oxide thickness, so they can be analyzed separately. These cases are presented in the following two subsections.

2.2.1 Random dopant-induced fluctuations

In the case of random-dopant induced fluctuations, the standard deviation of the threshold voltage can be written as [see equation (2.11)]:

$$\sigma_{V_T}[DF] = \sqrt{\sum_i \left(\gamma_{V_T}^{D_i}\right)^2 \frac{D_{0i}}{\Delta V_i}} \,. \tag{2.30}$$

This formula can be further simplified in the case of two-dimensional simulations, which are appropriate for wide devices. In this case, the volume of the *i*th discretization cell can be written as:

$$\Delta V_i = W \Delta S_i , \tag{2.31}$$

where W and ΔS_i are the width and the cross-sectional area of the *i*th mesh cell, respectively. Formulas (2.30) and (2.31) imply that:

$$\sigma_{V_T}[DF] = \sqrt{\frac{1}{W}\sum_i \left(\gamma_{V_T}^{D_i}\right)^2 \frac{D_{0i}}{\Delta S_i}} . \tag{2.32}$$

Note that the standard deviation of the threshold voltage is inversely proportional to the square root of the device width. Previously, this result was extracted after extensive numerical computations of three dimensional problems. It is remarkable that we obtain this result analytically by using a two dimensional model of MOSFET.

First, we report the results of the threshold voltage variances computed for a MOSFET device with channel length $L = 50$ nm, channel width $W = 50$ nm, and oxide thickness $t = 3$ nm. These results are compared to those presented in [66] for two average doping values $D_0 = 8.6 \cdot 10^{17}$ cm^{-3} and $D_0 = 4.3 \cdot 10^{17}$ cm^{-3}. Our computations produce the values σ_{V_T} =32 mV and σ_{V_T} =22 mV, while the computations presented in [66] produce the values σ_{V_T} = 29 mV and σ_{V_T} = 23 mV, respectively.

The results for the standard deviations of threshold voltage obtained for the 50 nm channel length MOSFET device (MOS A) are presented in Figure 2.2(a) and compared with those obtained by Asenov *et al.* [68] for various oxide thicknesses. In Ref. [68], σ_{V_T} is computed by simulating N = 200 MOSFET devices, which implies

statistical errors of about $1/\sqrt{2N} = 5\%$. The vertical bars in Figure 2.2(a) correspond to the absolute value of these errors and they show the range in which σ_{V_T} lies with a probability of 68%. There is very good agreement between our results and those obtained by using the statistical method in the case of classical computations.

Figure 2.2(b) presents the standard deviation of threshold voltage as a function of the doping concentration in the channel for two MOSFET devices: MOS A and MOS B (see the Appendix). In the case of the retrograde doping profile (MOS B), the doping concentrations indicated along the horizontal axis correspond to the doping concentration at a distance of 20 nm from the oxide, while the concentration at the surface is 10 times smaller than this value. It is remarkable that the variance of threshold voltage for the 30 nm channel device (MOS B) is smaller than the threshold voltage variance for the 50 nm channel device (MOS A) due to the improved doping configuration. The retrograde doping profile not only suppresses the short-channel effects, but also behaves like an epitaxial layer of smaller concentration that causes σ_{V_T} to decrease. More details about MOSFET structures that considerably reduce the fluctuations of threshold voltage will be provided in the last section of this chapter.

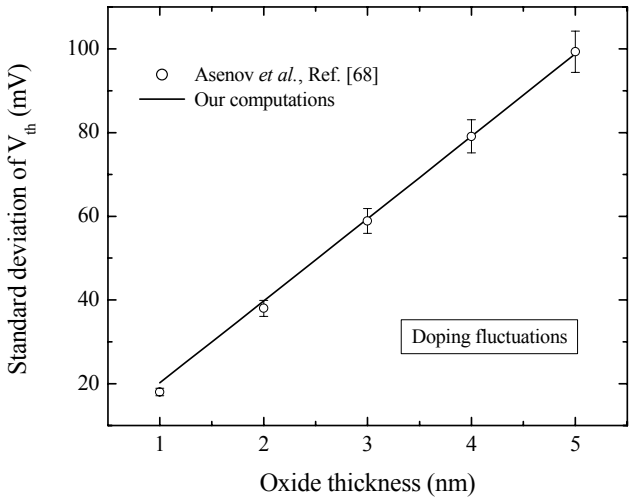

(a)

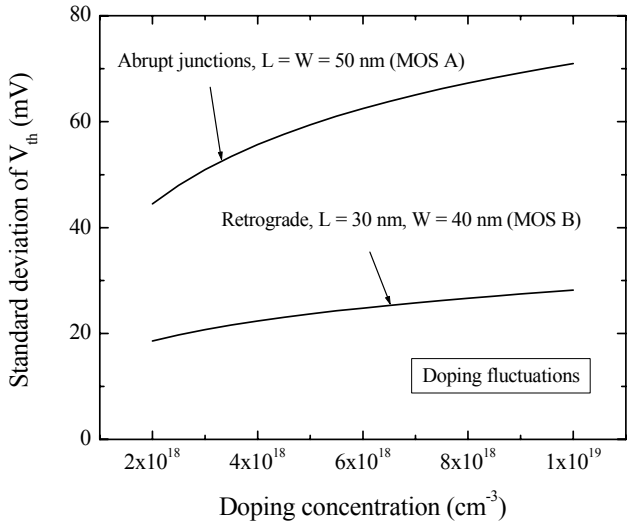

(b)

Figure 2.2 Standard deviation of threshold voltage as a function of oxide thickness (a) and average doping concentration in the channel (b).

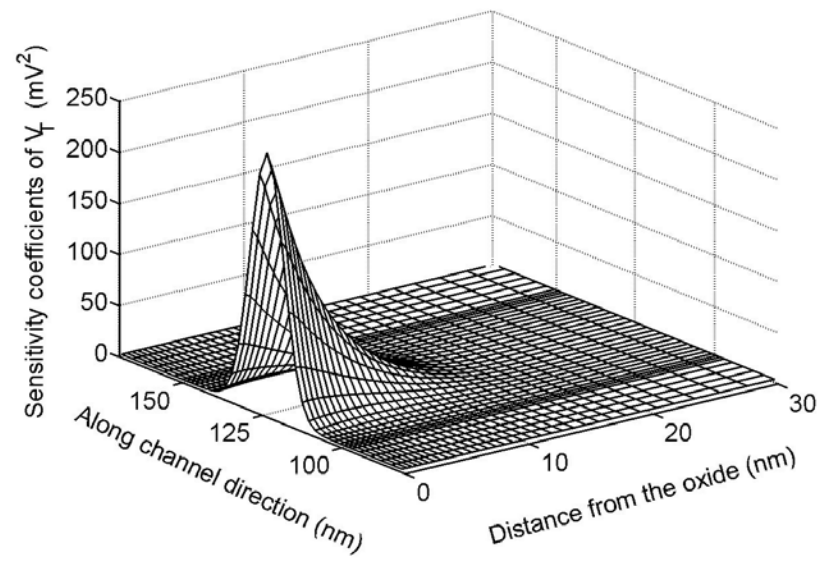

(a)

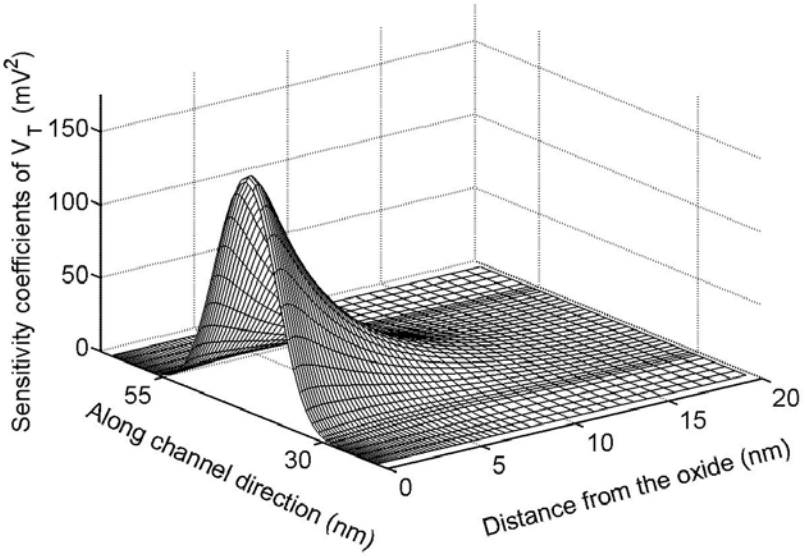

(b)

Figure 2.3: Doping sensitivity coefficients of threeshold voltage for the 50 nm channel length (MOS A) and 25 nm channel length MOSFET devices (MOS C).

One of the major advantages of the linearization method is that it provides information on the sensitivity of the variance of the threshold voltage to different locations of the doping fluctuations. Figure 2.3 presents the values of the sensitivity coefficients for the 50 nm (MOS A) and 25 nm (MOS C) channel length MOSFET devices. We observe that the most sensitive region to the fluctuations of threshold voltage is the immediate proximity of the semiconductor/oxide interface. Therefore, in order to reduce these fluctuations, the doping concentration in the region close to the semiconductor/oxide interface should be controlled with maximum precision.

2.2.2 Random oxide roughness induced fluctuations

Over the past years, threshold voltage fluctuations induced by random oxide thickness variations have not received the same attention as random doping induced fluctuations. However, our simulation experiments show that the two effects are equally important. In this section, the doping concentration is considered constant (non-fluctuating) and only the fluctuations of V_T induced by random oxide thickness are analyzed.

In the case of random-dopant induced fluctuations, the standard deviation of the threshold voltage can be written as [see equation (2.11)]:

$$\sigma_{V_T}\left[OTF\right] = \sqrt{\sum_{i,j} \gamma_{V_T}^{t_i} \gamma_{V_T}^{t_j} ACF\left(i,j\right)}\,. \tag{2.33}$$

The oxide surface was initially characterized by a Gaussian autocorrelation function:

$$ACF\left(r\right) = \Delta^2 e^{-\frac{r^2}{L_c^2}}\,. \tag{2.34}$$

where Δ is the roughness of the surface, L_c is the correlation length of the fluctuations, and r is the spatial distance measured at the surface of the oxide. However, more recent measurements made with the help of atomic force microscopy (AFM) show that the *ACF* of the oxide thickness fluctuations is better described by an exponential distribution function [22]:

$$ACF(r) = \Delta^2 e^{-\frac{r}{L_c}}. \tag{2.35}$$

Roughness can be accurately measured experimentally and the reported values range between 0.15 nm and 0.5 nm for SiO_2 surfaces. Since the standard deviation of V_T increases linearly with Δ [see equations (2.33)-(2.35)], we assume that roughness has a constant value of $\Delta = 0.15$ nm; for any other Δ, the standard deviation of V_T can be easily computed by using appropriate scaling. The correlation length depends mostly on the fabrication process and it is more difficult to measure experimentally. The values of L_c measured by using AFM vary from 10 nm to 25 nm and the simulations presented in this section take this uncertainty into account by presenting results for the whole range of variation of L_c.

Figures 2.4 (a) and (b) present the computed standard deviation of V_T as a function of the channel length for two groups of devices. In the first group [Figure 2.4(a)], devices are scaled down by using the constant field scaling rule [81], according to which the device dimensions and the doping are scaled proportionally, by the same factor. In the second group [Figure 2.4(a)], devices are scaled down by using the constant voltage scaling rule according to which, if dimensions are decreased by a

factor *k,* the doping concentration is increased by k^2. We observe that the values of the standard deviation of V_T are smaller in the case of constant field scaling because of lower doping concentration in the channel. The same effect was observed by Nishinohara *et al*. [65] for random doping induced fluctuations of V_T.

In the case of long channel MOSFET devices, threshold voltage increases linearly with the oxide thickness. For correlation lengths that are large in comparison with the device dimensions, the standard deviation of the threshold voltage can be easily found by using the "inversion" definition of V_T:

$$\sigma_{V_T}\left[OTF\right]_{L_c=\infty} = \frac{\Delta}{\varepsilon_{Ox}}\sqrt{4\varepsilon_{Si}kTN_a \ln\left(\frac{N_a}{n_i}\right)}, \qquad (2.36)$$

where N_a is the average doping concentration in the channel. The standard deviation of V_T computed by using (2.36) is represented in Figures 2.4 (a) and (b) by a dash line. Numerical simulations correctly predict the theoretical value of σ_{V_T} for long channel devices, which proves that the linearization method presented in the previous section calculates the variance of V_T for long devices accurately.

For small MOSFET devices we compare our results with those published in Ref. [32]. For a 30 nm channel length device with abrupt junctions, $N_a = 5\times10^{18}$ cm^{-3}, $t_{ox} = 1.05$ nm, $x_j = 7$ nm, and by assuming constant electron and hole mobilities, as well as long correlation lengths of the oxide thickness fluctuations, our computations give the value $\sigma_{V_T} = 41.5$ mV. This value is in perfect agreement with those reported

in Ref. [32], which was obtained by using the Monte-Carlo technique: $\sigma_{V_T} = (41 \pm 2)$ mV.

We also investigate the dependence of the fluctuations of threshold voltage on the doping concentration in the channel, oxide thickness, and channel length. The results of these simulations are presented in Figures 2.5 (a), (b), and (c), respectively, for MOS C (see the Appendix). The dependence of σ_{V_T} on the doping concentration and oxide thickness can be easily interpreted qualitatively by using equation (2.36). Notice that σ_{V_T} increases approximately like $\sqrt{N_a}$ and it is independent of the oxide thickness. Similar results were obtained by Asenov *et al*. [32] for a 30 nm channel length MOSFET device by using the Monte-Carlo technique. The (in)dependence of σ_{V_T} on the oxide thickness can be proved analytically as follows. If we disregard the depletion effects of the polysilicon region and consider the electric field in the oxide to be uniform, t enters linearly in the transport equations (2.19) through the boundary conditions at the semiconductor-oxide interface [82]:

$$\varphi + t\frac{\varepsilon_{Si}}{\varepsilon_{Ox}}\frac{\partial \varphi}{\partial n} = V_G + \frac{t}{\varepsilon_{Ox}}Q_{it}\,, \tag{2.37}$$

where $\frac{\partial \varphi}{\partial n}$ is the normal derivative of the potential at the boundary and Q_{it} is the interface (trapped) charge density. Since equation (2.37) is linear in *t*, the derivative $\boldsymbol{F_t}$ does not depend on *t*, so the fluctuations of V_T [see equation (2.26)] and σ_{V_T} are independent of the oxide thickness.

Figure 2.6 presents the dependence of σ_{V_T} on the correlation length of oxide thickness fluctuations by using the exponential (2.35) and the Gaussian (2.34) autocorrelation functions. The standard deviation of V_T computed by using the exponential ACF is smaller than the one computed by using the Gaussian ACF for short correlation lengths, but larger for long correlation lengths. This implies that discrepancies in the modeling of oxide surface may appear if the correlation function is not properly chosen. However, for simulation purposes, one can choose either ACF if the correlation length and the roughness are carefully adjusted.

Finally, we present the analysis of threshold voltage sensitivity to local fluctuations of the oxide thickness at different points on the semiconductor-oxide interface. This analysis is especially important in the design of fluctuations-resistant structures. Figure 2.7 presents the (mesh independent) sensitivity coefficients as a function of the (*x, y*) position on the interface. These sensitivity coefficients are defined as $\left(\gamma_{V_T}^{t_j} / \Delta S_j\right)^2$, where ΔS_j is the area of the discretization cell *j* on the surface of the oxide. It can be observed that the threshold voltage is rather sensitive to the fluctuations of oxide thickness in the middle region of the oxide layer, but quite insensitive to the edge fluctuations of the oxide thickness. This effect can have positive implications for the fabrication process of the oxide because the ulterior etching and deposition of polysilicon usually deteriorates the edges of the oxide layer.

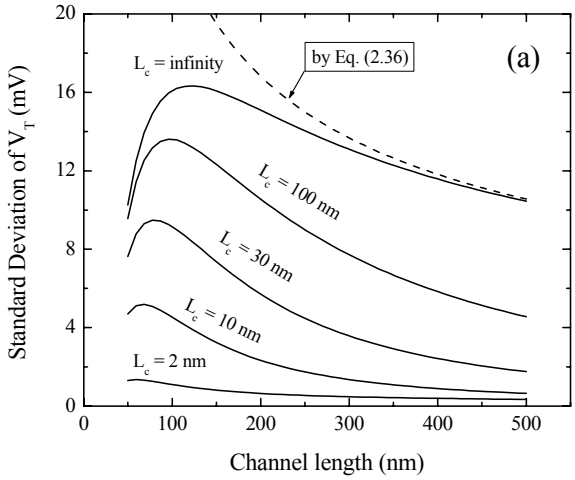

(a)

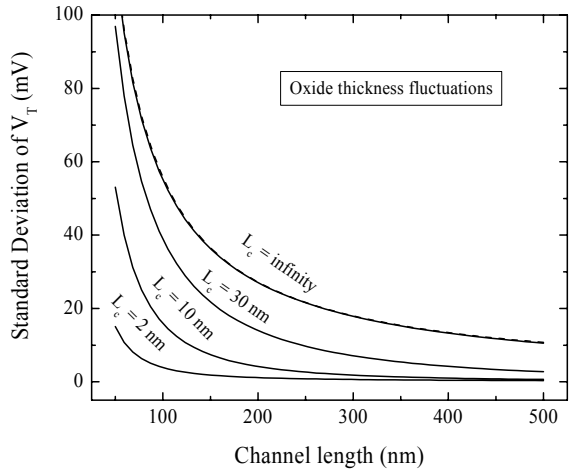

(b)

Figure 2.4: Standard deviation of threshold voltage as a function of the channel length. Constant field scaling rule (a) and constant potential scaling rule (b) are considered in these simulations. Dash lines correspond to computations given by equation (2.36).

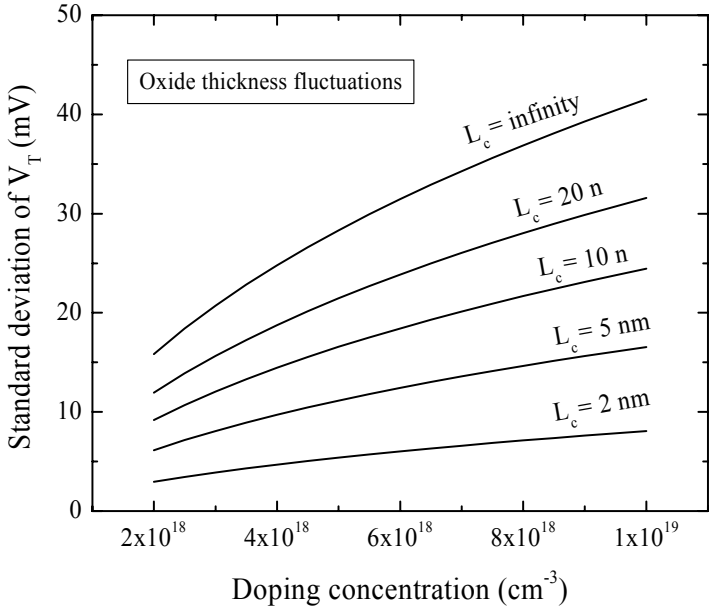
Oxide thickness fluctuations
L_c = infinity
L_c = 20 n
L_c = 10 n
L_c = 5 nm
L_c = 2 nm
Standard deviation of V_T (mV)
Doping concentration (cm^{-3})
0
10
20
30
40
50
$2x10^{18}$
$4x10^{18}$
$6x10^{18}$
$8x10^{18}$
$1x10^{19}$

(a)

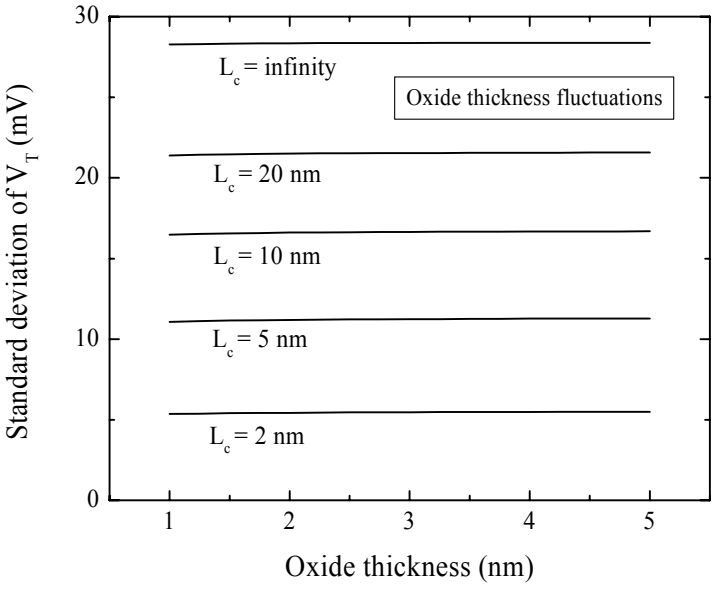
L_c = infinity
Oxide thickness fluctuations
L_c = 20 nm
L_c = 10 nm
L_c = 5 nm
L_c = 2 nm
Standard deviation of V_T (mV)
Oxide thickness (nm)
0
10
20
30
1
2
3
4
5

(b)

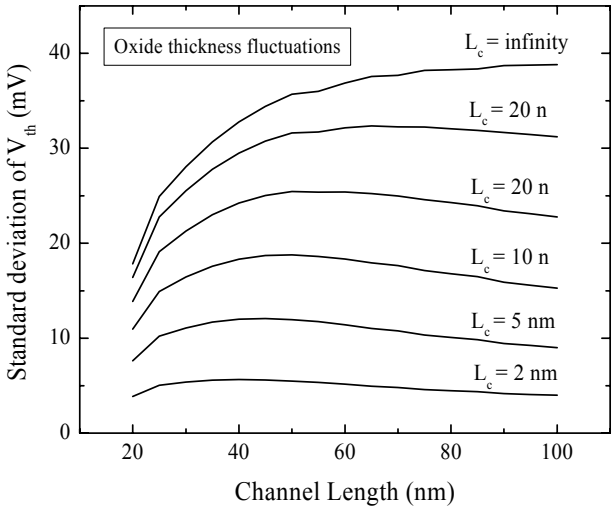

(c)

Figure 2.5: Standard deviation of threshold voltage as a function of the average doping concentration in channel (a), oxide thickness (b), and channel length (c), respectively.

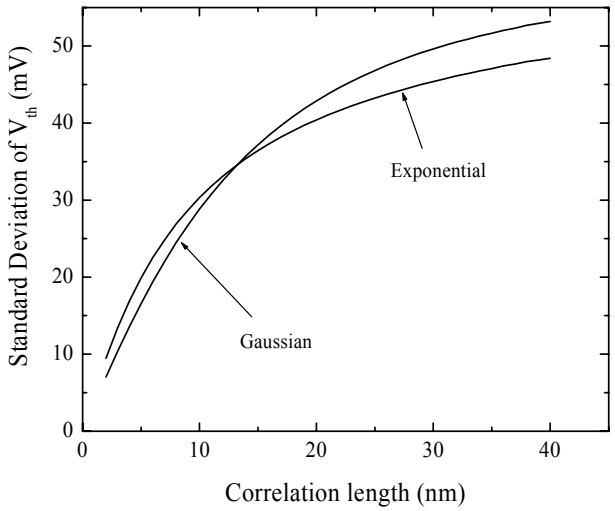

Figure 2.6: Standard deviation of the threshold voltage as a function of the correlation length of oxide roughness fluctuations (classical computations).

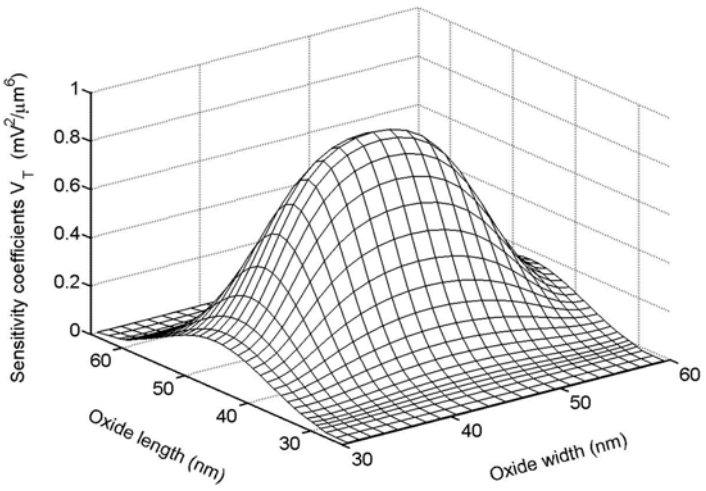

Figure 2.7: Oxide thickness sensitivity coefficients for threeshold voltage (30x40 nm MOSFET device).

2.3 Analysis of fluctuations of threshold voltage by using the "complete inversion" definition

In the first two sections of this chapter, the "current definition" of threshold voltage was adopted for the calculation of the variance of V_T. This approach involved the linearization of the transport equations (e.g. the Poisson equation and current continuity equations in the case of the drift-diffusion model) around the average values of the state variables. A much simpler way to compute the fluctuations of threshold voltage in semiconductor devices is to use the complete inversion definition of V_T. This approach is computationally much more efficient, since it requires only the linearization of the Poisson equation. It can be regarded as a particular case of the

general method presented in the previous section but, due to its particular relevance, this section will be entirely devoted to it.

To clearly emphasize the main idea of the method, we focus on the two-dimensional model of MOSFET and adopt the "theoretical" ("textbook") definition of the threshold voltage as the gate voltage at which the onset of complete inversion occurs [81].

The inversion phenomena can be studied by using the following nonlinear Poisson equation for electric potential φ:

$$\nabla^2\varphi = \frac{qn_i}{\varepsilon_s}\left(e^{\frac{\varphi}{V_{th}}} - e^{-\frac{\varphi}{V_{th}}}\right) - \frac{qD}{\varepsilon_s}, \tag{2.38}$$

Here, n_i is the intrinsic electron density, V_{th} is the thermal voltage equal to $\frac{kT}{q}$, and D is the doping, while other symbols in (2.38) have their usual meaning.

Equation (2.38) is the nonlinear Poisson equation because the densities of mobile electrons and holes are potential dependent and equal to $n_i e^{\frac{\varphi}{V_{th}}}$ and $n_i e^{-\frac{\varphi}{V_{th}}}$, respectively. It is worth stressing that the nonlinear Poisson equation (2.38) is valid at equilibrium (or close to equilibrium) conditions for both the drift-diffusion and the semiclassical transport models. In this sense, the threshold voltage variance calculations based on the nonlinear Poisson equation are insensitive to the specific choice of the transport model.

In the pure inversion regime of MOSFET devices, the solution of the nonlinear Poisson equation is subject to the following boundary conditions [82] (see Figure 2.8):

1. zero Dirichlet boundary conditions on ohmic contacts C_k:

$$\varphi_k = 0\,, \tag{2.39}$$

2. zero Neumann boundary conditions on the artificial boundaries C^k:

$$\frac{\partial \varphi}{\partial \nu} = 0\,, \tag{2.40}$$

3. mixed (impedance) type boundary on oxide-semiconductor interface C_0:

$$\varphi + t\frac{\varepsilon_s}{\varepsilon_d}\frac{\partial \varphi}{\partial \nu} = V_G + \frac{\lambda}{\varepsilon_d}Q_{it}\,, \tag{2.41}$$

where t is the oxide thickness, ε_d is the oxide permittivity, V_G is the applied gate voltage, and Q_{it} is the interface (trapped) or oxide charge density.

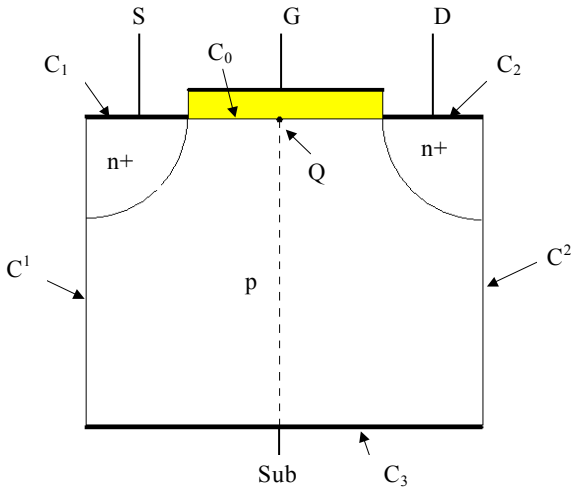

Figure 2.8: MOSFET device.

The electric potential distribution within the device is determined by solving the boundary value problem described by the system of equations (2.38)-(2.41). For

the given device geometry, this distribution depends on doping D and applied gate voltage V_G. As mentioned in the Introduction, in the p-region (substrate) doping D fluctuates from point to point and from one device to another. For this reason, doping can be treated as a random field. We represent this random field in the form [73]:

$$D = D_0 + \tilde{D}\,, \quad \left\langle \tilde{D} \right\rangle = 0 \tag{2.42}$$

where symbol "$\langle\ \rangle$" stands for the expected (mean) value.

If doping fluctuations are realized on very fine spatial scales (in comparison with device dimensions), then averaging (homogenization) phenomenon occurs and the potential distribution is by and large insensitive to doping fluctuations. However, if doping fluctuations occur on spatial scales more or less comparable with device dimensions, they may cause noticeable fluctuations $\tilde{\varphi}$ of the electric potential, as well as a pronounced "shift" φ_{sh} in the average value of φ. These effects can be mathematically expressed as follows [73]:

$$\varphi = \varphi_0 + \varphi_{sh} + \tilde{\varphi}\,, \quad \left\langle \tilde{\varphi} \right\rangle = 0\,. \tag{2.43}$$

Here, φ_0 is the electric potential in the case when the effect of doping fluctuations is negligible. This potential satisfies the following nonlinear Poisson equation:

$$\nabla^2 \varphi_0 = \frac{q n_i}{\varepsilon_s}\left(e^{\frac{\varphi_0}{V_T}} - e^{-\frac{\varphi_0}{V_T}} \right) - \frac{q D_0}{\varepsilon_s}\,. \tag{2.44}$$

Normally, φ_{sh} and $\tilde{\varphi}$ are relatively small; it does not make sense to manufacture devices with large fluctuations. Therefore, the perturbation ("small signal analysis") technique can be employed to derive the following equation for $\varphi_{sh} + \tilde{\varphi}$ from (2.38):

$$\nabla^2\left(\varphi_{sh}+\tilde{\varphi}\right)=\frac{2qn_i}{\varepsilon_s V_T}\left(\cosh\frac{\varphi_0}{V_T}\right)\left(\varphi_{sh}+\tilde{\varphi}\right)-\frac{q\tilde{D}}{\varepsilon_s}. \tag{2.45}$$

By taking the average of both sides of equation (2.45) and using the fact that $\left\langle\tilde{\varphi}\right\rangle=0$ and $\left\langle\tilde{D}\right\rangle=0$, we obtain:

$$\nabla^2\varphi_{sh}=\frac{2qn_i}{\varepsilon_s V_T}\left(\cosh\frac{\varphi_0}{V_T}\right)\varphi_{sh}. \tag{2.46}$$

Next, we subtract equation (2.46) from equation (2.45), to arrive at the following equation for potential fluctuations $\tilde{\varphi}$:

$$\nabla^2\tilde{\varphi}-\frac{2qn_i}{\varepsilon_s V_T}\left(\cosh\frac{\varphi_0}{V_T}\right)\tilde{\varphi}=-\frac{q\tilde{D}}{\varepsilon_s}. \tag{2.47}$$

It is clear that $\tilde{\varphi}$ satisfies the following boundary conditions:

$$\tilde{\varphi}\big|_{C_k}=0,\quad \left.\frac{\partial\tilde{\varphi}}{\partial\nu}\right|_{C^k}=0,\quad \left.\left(\tilde{\varphi}+t\frac{\varepsilon_s}{\varepsilon_d}\frac{\partial\tilde{\varphi}}{\partial\nu}\right)\right|_{C_0}=\tilde{V}_G, \tag{2.48}$$

where $\tilde{V}_G$ stands for the gate voltage fluctuations. These fluctuations are introduced in order to compensate for the doping fluctuations and to maintain the "same" inversion conditions. In deriving boundary condition (2.48) from boundary condition (2.41), the fluctuations of oxide thickness t and trapped charges Q_{it} were neglected. These fluctuations will be taken into account later on.

It is convenient to express the solution of boundary value problem (2.47)-(2.48) in terms of the Green function, which is defined as the solution of the following boundary value problem [73]:

$$\nabla^2 G - \frac{2qn_i}{\varepsilon_s V_T}\left(\cosh\frac{\varphi_0}{V_T}\right)G = -\delta(Q-M), \tag{2.49}$$

$$G_{C_k} = 0, \qquad \left.\frac{\partial G}{\partial \nu}\right|_{C^k} = 0, \tag{2.50}$$

$$\left(G + t\frac{\varepsilon_s}{\varepsilon_d}\frac{\partial G}{\partial \nu}\right)\Bigg|_{C_0} = 0, \tag{2.51}$$

where $\delta(Q-M)$ is the Dirac delta function.

By using the above definition of the Green function, the following integral representation for the solution of the boundary value problem (2.47)-(2.48) can be derived:

$$\tilde{\varphi}(Q) = \frac{q}{\varepsilon_s}\int_{\Omega} G(Q,M)\,d(M)\,d\Omega_M + \gamma(Q)\tilde{V}_G, \tag{2.52}$$

where

$$\gamma(Q) = \frac{\varepsilon_d}{\varepsilon_s t}\int_{C_0} G(Q,M)\,d\Gamma_M\ . \tag{2.53}$$

Threshold voltage V_T of MOSFET devices can be defined as the gate voltage $V_G = V_T$ at which a minimum mobile electron density on the oxide interface is equal to the mobile hole density in the bulk p-region at zero bias voltages, i.e. before the inversion. For the sake of brevity, this definition will henceforth be referred to as the "inversion" definition of threshold voltage. The minimum electron density is usually achieved at the middle point Q of the semiconductor-oxide interface. It can be easily shown that the required electron density is attained when the electric potential $\varphi(Q)$ takes the following value:

$$\varphi(Q) = \frac{kT}{q} \ln \frac{D_0}{n_i} . \tag{2.54}$$

Thus, threshold voltage is the gate voltage $V_T = V_G$ for which condition (2.54) is satisfied.

We now define fluctuations $\tilde{V}_T$ of the threshold voltage as the fluctuations of the gate voltage that compensate for the doping fluctuations and keep the value of the electric potential at middle point Q constant and equal to the value specified by formula (2.54). In other words, if we substitute $\tilde{V}_T$ for $\tilde{V}_G$ in equation (2.52), then at the middle point, $\tilde{\varphi}(Q) = 0$. This leads to the following expression:

$$\tilde{V}_T = -\frac{q}{\varepsilon_s \gamma(Q)} \int_\Omega G(Q,M)\, d(M)\, d\Omega_M . \tag{2.55}$$

By squaring formula (2.55) and performing statistical averaging on both sides, we derive the following expression for the variance $\sigma^2_{V_T}$ of the threshold voltage:

$$\sigma^2_{V_T} = \left(\frac{q}{\varepsilon_s \gamma(Q)} \right)^2 \int_\Omega \int_\Omega G(Q,M) G(Q,P) K_D(M,P)\, d\Omega_P d\Omega_M , \tag{2.56}$$

where $K_D(M,P)$ is the autocovariance function of random field D. For the sake of further discussions, it is convenient to write the last formula in the discretized form:

$$\sigma^2_{V_T} = \alpha^2 \sum_{i,j} \sum_{m,n} G^{i_0,j_0}_{i,j} G^{i_0,j_0}_{m,n} K^{i,j}_{m,n} \Delta S_{i,j} \Delta S_{m,n} , \tag{2.57}$$

where: $\alpha = q/\varepsilon_s \gamma(Q)$, index pair (i_0, j_0) corresponds to point Q, index pairs (i, j) are used for the numeration of other mesh points, while other notations have their usual meaning.

It is customary to assume that doping densities at different locations are independent random variables. This implies that:

$$K_{m,n}^{i,j} = \delta_{m,n}^{i,j}\sigma_{D_{i,j}}^2 , \tag{2.58}$$

where $\delta_{m,n}^{i,j}$ is the Kronecker delta and $\sigma_{D_{i,j}}^2$ is the variance of $D_{i,j}$.

By substituting formula (2.58) into equation (2.57), we arrive at:

$$\sigma_{V_T}^2 = \alpha^2 \sum_{i,j} \left(G_{i,j}^{i_0,j_0} \Delta S_{i,j} \right)^2 \sigma_{D_{i,j}}^2 . \tag{2.59}$$

By using equation (2.10), (2.59) can be written as:

$$\sigma_{V_T}^2 = \sum_{i,j} \lambda_{i,j} D_{i,j}^0 , \tag{2.60}$$

where $\lambda_{i,j}$ are the doping superposition coefficients of the threshold voltage and:

$$\lambda_{i,j} = \left(\alpha G_{i,j}^{i_0,j_0} \right)^2 \frac{\Delta S_{i,j}}{W}, \tag{2.61}$$

where W is the width of the device.

Thus, the problem of evaluating the variance of the threshold voltage is reduced to the calculation of $\lambda_{i,j}$. This can be accomplished in two steps. First, we solve the nonlinear Poisson equation (2.44) with boundary conditions (2.39)-(2.41) to find V_G and the distribution of φ_0 for which the condition (2.54) is satisfied. Then we use this distribution of φ_0 to solve a discretized version of boundary value problem (2.49)-(2.51) and to find mesh point values of the Green function and coefficients $\lambda_{i,j}$. The numerical solution of the nonlinear Poisson equation (as well as of the discretized boundary value problem (2.49)-(2.51)) can be determined by using the globally convergent techniques presented in [85].

In describing the fundamentals of the method, we neglected fluctuations of oxide thickness and trapped charges. These fluctuations can be taken into account by modifying boundary condition (2.48) as follows:

$$\left(\tilde{\varphi}+t_0\frac{\varepsilon_s}{\varepsilon_d}\frac{\partial\tilde{\varphi}}{\partial\nu}\right)\Bigg|_{C_0}=\tilde{V}_G+\frac{t_0}{\varepsilon_s}\tilde{Q}_{it}+\tilde{t}\left(\frac{Q_{it}^0}{\varepsilon_s}-\frac{\varepsilon_s}{\varepsilon_d}\frac{\partial\varphi_0}{\partial\nu}\right). \tag{2.62}$$

Here, t_0 and Q_{it}^0 are the expected values of oxide thickness and interface (trapped) charges, $\tilde{t}$ and $\widetilde{Q}_{it}$ are their fluctuations, while φ_0 has the same meaning as before.

This modification of the interface boundary condition leads to the following modification of formula (2.52):

$$\tilde{\varphi}(Q)=\frac{q}{\varepsilon_s}\int_{\Omega}G(Q,M)d(M)d\Omega_M$$

$$+\gamma(Q)\tilde{V}_G+\beta(Q)\tilde{\Delta}+\frac{\Delta_0}{\varepsilon_s}\int_{C_0}G(Q,M)\tilde{Q}_{it}(M)d\Gamma_M\,, \tag{2.63}$$

where

$$\beta(Q)=\frac{\varepsilon_d}{\varepsilon_s t_0}\int_{C_0}G(Q,M)\left[\frac{Q_{it}^0(M)}{\varepsilon_s}-\frac{\varepsilon_s}{\varepsilon_d}\frac{\partial\varphi_0}{\partial\nu}(M)\right]d\Gamma_M\,. \tag{2.64}$$

By repeating the line of reasoning that led to the derivation of formula (2.60), we arrive at the following expression:

$$\sigma_{V_T}^2=\sum_{i,j}\lambda_{i,j}D_{i,j}^0+\left(\frac{\beta}{\gamma}\right)^2\sigma_{ox}^2+\left(\frac{t_0}{\varepsilon_s\gamma}\right)^2{\sum_{i,j}}'\left(G_{i,j}^{i_0,j_0}\Delta l_{i,j}\right)^2\sigma_{Q_{it}}^2\,. \tag{2.65}$$

Here, ${\sum_{i,j}}'$ is the sum over the mesh points that belong to C_0, while σ_{ox}^2 and $\sigma_{Q_{it}}^2$ are the variances of oxide thickness and interface charges, respectively. Formula (2.65)

can be used to compute the standard deviation of the threshold voltage if the superposition coefficients $\lambda_{i,j}$, β, γ, and $G_{i,j}^{i_0,j_0}$ are known.

We will close this section with the presentation of a few sample simulation results obtained for the 50×50 nm MOSFET device (MOS A described in the Appendix). We will focus primarily on the dependence of the threshold voltage variance on channel width, oxide thickness and substrate doping. Figure 2.9(a) presents the dependence of $\sigma_{V_{th}}$ on channel width. Note that σ_{V_T} is inversely proportional to $\sqrt{W}$; the same result was obtained analytically in Section II by using a two dimensional model for MOSFET.

Figure 2.9(b) presents the dependence of σ_{V_T} on oxide thickness t. We observe that σ_{V_T} is directly proportional to t. This result was also observed by Asenov *et al.* [88] by performing a large number of simulation experiments and by using the Monte-Carlo technique to find σ_{V_T}. Figure 2.9 (c) presents the dependence of σ_{V_T} on the substrate doping D_0. We approximated the computed relation $\sigma_{V_T}(D)$ by the power low $\sigma_{V_T}\approx aD^n$ by using the χ^2 criterion. We found that within the doping range presented in Figure 2.9 and within the error margin of ±0.015, the exponent n is equal to 0.406, which is consistent with the results from Ref. [88]. However, it must be noted that the value of n is strongly dependent on the range of doping variations, and we found that it may vary from 0.25 for low doping concentrations (as analytically predicted in Refs. [13] and [16]) to 0.42 for high doping concentrations.

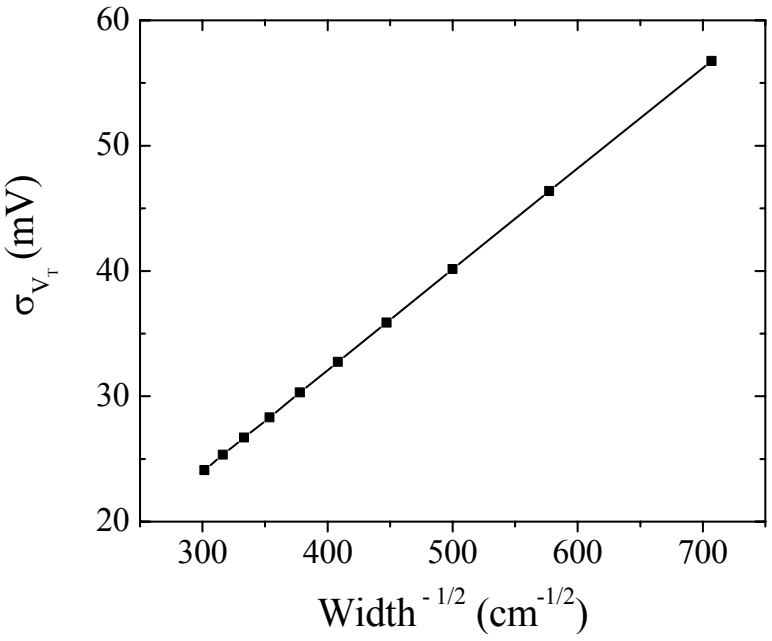
60
50
40
30
20
300
400
500
600
700
σ$_{V_T}$ (mV)
Width $^{-1/2}$ (cm$^{-1/2}$)

(a)

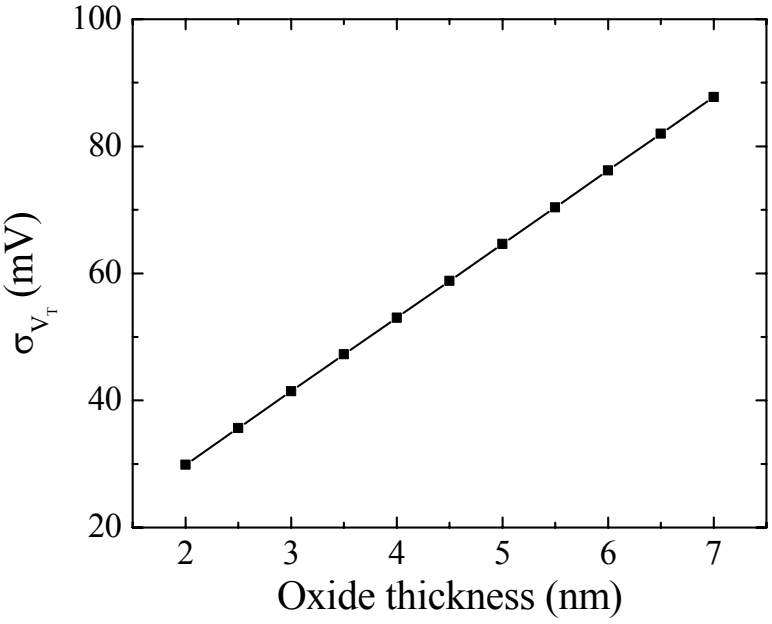
100
80
60
40
20
2
3
4
5
6
7
σ$_{V_T}$ (mV)
Oxide thickness (nm)

(b)

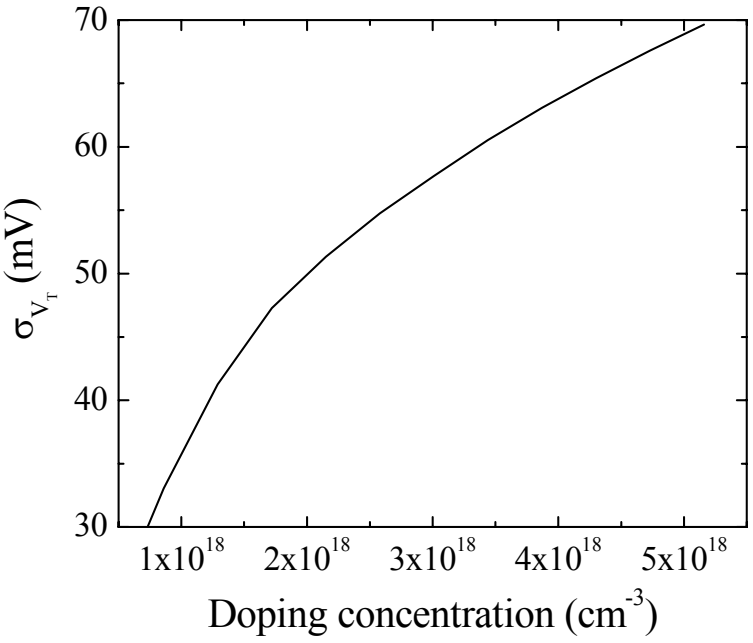

(c)

Figure 2.9: Dependence of standard deviation of threshold voltage on width (a), oxide thickness (b), and average doping concentration in the channel (c). Threshold voltage is defined through the "inversion" of minority carriers.

2.4 Shift of threshold voltage

The expected value of the threshold voltage $\langle V_T \rangle$ is different from the threshold voltage V_T^0 computed by considering constant (non-fluctuating) doping concentration and device dimensions. The difference $\Delta V_T = \langle V_T \rangle - V_T^0$ is usually referred to as the threshold voltage shift [see equation (1.3)]. This shift is very important because threshold voltage is one of the most important characteristics of MOSFET devices and the accuracy of the value we obtain for it is crucial for circuit design.

There is some controversy over the issue of the threshold voltage shift. While the published results of the calculations of the threshold voltage variance for similar devices are in fairly good agreement, the published computational results on the threshold voltage shift differ appreciably. It also appears that there is no consensus in literature with respect to the origin of the threshold voltage shift, or with respect to the possible lowering of (or increase in) the threshold voltage due to doping fluctuations.

It is important to stress that the threshold voltage shift is not directly measurable and that it can only be computed numerically. Usually, this shift is found by computing threshold voltage value V_T^0 by ignoring dopant fluctuations, then computing the mean value of threshold voltage $\langle V_T \rangle$ by averaging numerous calculations performed for various doping realizations, and, finally, by subtracting these two values. Since the threshold voltage shift is small in comparison with the threshold voltage itself, the subtraction of two approximately computed quantities is prone to numerical errors. This may account for the discrepancy in the computational

results of the threshold voltage shift published in literature. Later on in this section, we will present a technique that leads to the direct calculation of the threshold voltage and completely avoids the aforementioned subtraction.

Next, it must be emphasized that the origin of the threshold voltage shift is the nonlinearity of the transport equations. Since the threshold voltage shift is a nonlinear effect, it cannot be accounted for by using the linearized "shift" equation (2.46). Indeed, this equation is homogeneous and this inevitably leads to the zero value for the threshold voltage shift. Thus, it can be concluded that the threshold voltage shift calculations in the framework of the perturbation ("small signal analysis") technique are inherently more complicated than the threshold voltage variance calculations. In other words, "shift" calculations require second-order perturbation analysis.

It is shown below that the lowering of the threshold voltage is most likely to occur as a result of doping fluctuations. To demonstrate this, we assume that electric potential φ at each point of the device is a normally distributed Gaussian random variable with the probability density:

$$\rho(\varphi) = \frac{1}{\sqrt{2\pi}\sigma_{\varphi}} e^{-\frac{(\varphi - \langle\varphi\rangle)}{2\sigma_{\varphi}^2}}, \tag{2.66}$$

where $\langle\varphi\rangle$ stands for the expected value of φ, while σ_{φ}^2 is the variance of φ. This assumption has been demonstrated in literature through extensive numerical simulations [66].

By taking the average on both sides of the nonlinear Poisson equation (2.38) and by using the Gaussian probability density given by equation (2.66) to evaluate the

averages of the exponential terms of equation (2.38), we arrive at the following Poisson equation for $\overline{\varphi}$:

$$\nabla^2\overline{\varphi} = \frac{qn_i}{\varepsilon_s} e^{\frac{\sigma_\varphi^2}{2V_T}} \left(e^{\frac{\overline{\varphi}}{V_T}} - e^{-\frac{\overline{\varphi}}{V_T}} \right) - \frac{qD_0}{\varepsilon_s}. \tag{2.67}$$

By comparing equations (2.38) and (2.67), it can be concluded that equation (2.67) can be construed as the nonlinear Poisson equation for a semiconductor with effective intrinsic electron density equal to:

$$\langle n_i \rangle = n_i e^{\frac{\sigma_\varphi^2}{2V_T}}. \tag{2.68}$$

In other words, it can be asserted that doping fluctuations result in the increase of the effective intrinsic density. Indeed, according to (2.68), we find:

$$\langle n_i \rangle > n_i. \tag{2.69}$$

It can be easily proven that the above assertion is also valid in the case when random variable φ has any distribution density $\rho\left(\langle\varphi\rangle - \varphi\right)$ with even symmetry with respect to $\langle\varphi\rangle$. In this case, the averaged nonlinear Poisson equation (2.38) can be written as follows:

$$\nabla^2 \langle\varphi\rangle = \frac{q\langle n_i \rangle}{\varepsilon_s} \left(e^{\frac{\langle\varphi\rangle}{V_T}} - e^{-\frac{\langle\varphi\rangle}{V_T}} \right) - \frac{qD_0}{\varepsilon_s}, \tag{2.70}$$

where

$$\langle n_i \rangle = 2n_i \int_0^\infty \cosh\left(\frac{z}{V_T}\right) \rho(z)\, dz. \tag{2.71}$$

It is clear from formula (2.71) that inequality (2.69) holds.

The increase in the effective intrinsic density given by formula (2.71) is most likely to lead to the lowering of the threshold voltage. This lowering is the likely effect of random doping fluctuations.

From formula (2.43) we find:

$$\overline{\varphi} = \varphi_0 + \varphi_{sh} . \tag{2.72}$$

By substituting formula (2.72) into equation (2.67) and then subtracting equation (2.44), we arrive at the following nonlinear equation for φ_{sh}:

$$\nabla^2 \varphi_{sh} - \frac{2qn_i}{\varepsilon_s} e^{\frac{\sigma_\varphi^2}{2V_T}} \sinh\left(\frac{\varphi_{sh} + \varphi_0}{V_T} \right) = -\frac{2qn_i}{\varepsilon_s} \sinh\left(\frac{\varphi_0}{V_T} \right). \tag{2.73}$$

Another equation for φ_{sh} can be derived from equation (2.38) by using the second-order perturbation technique. In this derivation, formula (2.43) is substituted into equation (2.38) and the three terms of the Taylor expansion are used in the right-hand side of this equation. By employing the same reasoning as in the previous section, we obtain the following equation for φ_{sh}:

$$\nabla^2 \varphi_{sh} = \frac{2qn_i}{\varepsilon_s} \left[\cosh\left(\frac{\varphi_0}{V_T} \right) \frac{\varphi_{sh}}{V_T} + \sinh\left(\frac{\varphi_0}{V_T} \right) \frac{\varphi_{sh}^2 + \sigma_\varphi^2}{2V_T^2} \right]. \tag{2.74}$$

It can be shown that equations (2.73) and (2.74) are equivalent up to the terms of third-order of smallness with respect to σ_φ and φ_{sh}.

Equation (2.74) [or (2.73)] must be considered with the following boundary conditions:

$$\varphi_{sh}\big|_{C_k} = 0 , \quad \left. \frac{\partial \varphi_{sh}}{\partial \nu} \right|_{C^k} = 0 , \tag{2.75}$$

$$\left(\varphi_{sh} + t \frac{\varepsilon_s}{\varepsilon_d} \frac{\partial \varphi_{sh}}{\partial \nu} \right) \Bigg|_{C_0} = V_G^{sh} . \tag{2.76}$$

The threshold voltage shift V_T^{sh} is defined as the value of V_G^{sh} at which φ_{sh} at the middle point Q equals zero. This condition together with formulas (2.74)-(2.76) define the approach to threshold voltage shift calculations. The distinct feature of this approach is that the threshold voltage shift is computed directly, and no subtraction of $\overline{V}_T$ and V_{T0} is required. The most computationally expensive part of this approach is the calculation of σ_φ^2 at all mesh points. We perform these calculations by using the algorithm that was developed in the previous section for σ_T^2 calculations. The numerical solution of equation (2.74) can be somewhat simplified by neglecting the term with φ_{sh}^2. This term is usually small in comparison with the first (linear) term in the right-hand side of (2.74). If necessary the term with φ_{sh}^2 can be accounted for through iterations.

Our discussion of threshold voltage shift calculations is based on the nonlinear Poisson equation (2.38). These calculations are relevant to the definition of the threshold voltage as the gate voltage at which the onset of complete inversion occurs. However, the main idea of the above discussion can be carried out within the framework of the "current" definition of the threshold voltage adopted in the first section of this chapter. This can be done by using the second-order perturbation technique for discretized transport equation (2.19) and by computing the threshold voltage shift from the condition that $I_{SD}^{sh} = 0$. This analysis is conceptually straightforward and mimics the reasoning presented in this section.

2.5 Suppression of random doping fluctuations of threshold voltage

A relatively easy way to reduce the fluctuations of threshold voltage without a major change in the MOSFET architecture is the appropriate tailoring of the channel doping profile. One can see from equation (2.30) that, in order to decrease the standard deviation of V_T, the absolute values of superposition coefficients $\gamma_{V_T}^i$ and the average doping concentrations D_{0i} should be decreased. However, as we will show in the following, the superposition coefficients are more or less independent of the characteristics of the MOSFET devices and the only way to reduce $\sigma_{V_T}^2$ is to decrease the values of the doping concentration in the conduction channel. A common method to decrease these values – and thus, to enhance the dopant fluctuation immunity – is to introduce a thin, low-doped epitaxial layer immediately below the interface [87], [88] (see Figure 2.10).

Figure 2.11 presents the results of the calculation of σ_{V_T} as a function of thickness d_{epi} of the epitaxial layer for a MOSFET device with $L = 50$ nm, $W = 50$ nm, $t = 3$ nm, $D_0^{epi} = 10^{15}$ cm^{-3} and $D_0^{bulk} = 5 \cdot 10^{18}$ cm^{-3}. We observe that the fluctuations of the threshold voltage are substantially reduced by the presence of the epitaxial layer. Figure 2.11 also presents the results obtained in Ref. [88] by using the Monte-Carlo techniques. It is clear that our results are in a reasonably good agreement with those published in Ref. [88].

As argued before, one of the major advantages of the linearization method is that it provides information on the sensitivity of the variance of threshold voltage to

different locations of the doping fluctuations (for example, see Figure 2.3). It is interesting that the sensitivity coefficients of the threshold voltage are quite insensitive to the presence of the epitaxial layer. Figure 2.12 presents the sensitivity coefficients of the threshold voltage for two values of the thickness of the epitaxial layer. One can observe that the sensitivity coefficients are "weakly" dependent on the actual value of the bulk doping concentration. This fact suggests that the computed sensitivity coefficients can be immediately used to estimate the appropriate thickness of the epitaxial layer. In this respect, the linearization technique yields information that can be instrumental in the design of random dopant fluctuation-resistant structures.

Finally, it should be noted that the retrograde MOSFET simulated in Figure 2.2(b) can be regarded as a fluctuation resistant structure, because the low dopant concentration next to the oxide/semiconductor interface behaves like an epitaxial layer. For this reason, the displayed values of the standard deviation of the threshold voltage have smaller values for the retrograde MOSFET than for the abrupt junction MOSFET with no epitaxial layer, even though the overall geometrical dimensions are smaller.

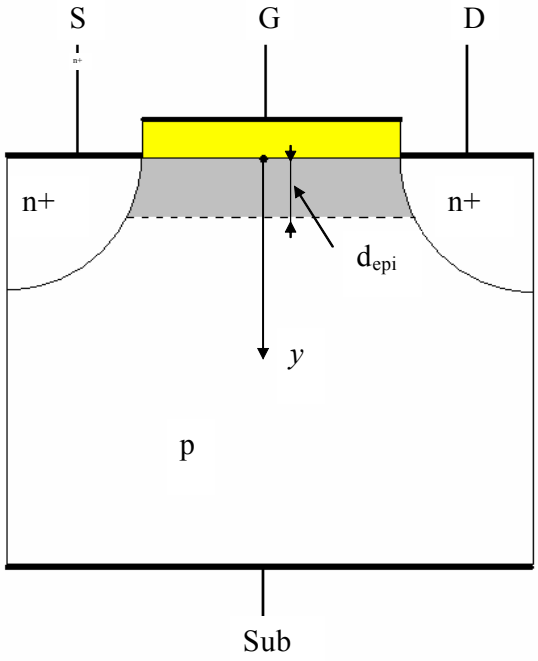

(a)

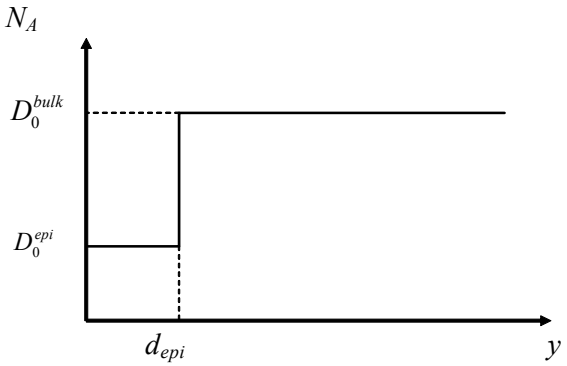

(b)

Figure 2.10: MOSFET device with epitaxial layer (a) and corresponding doping profile (b).

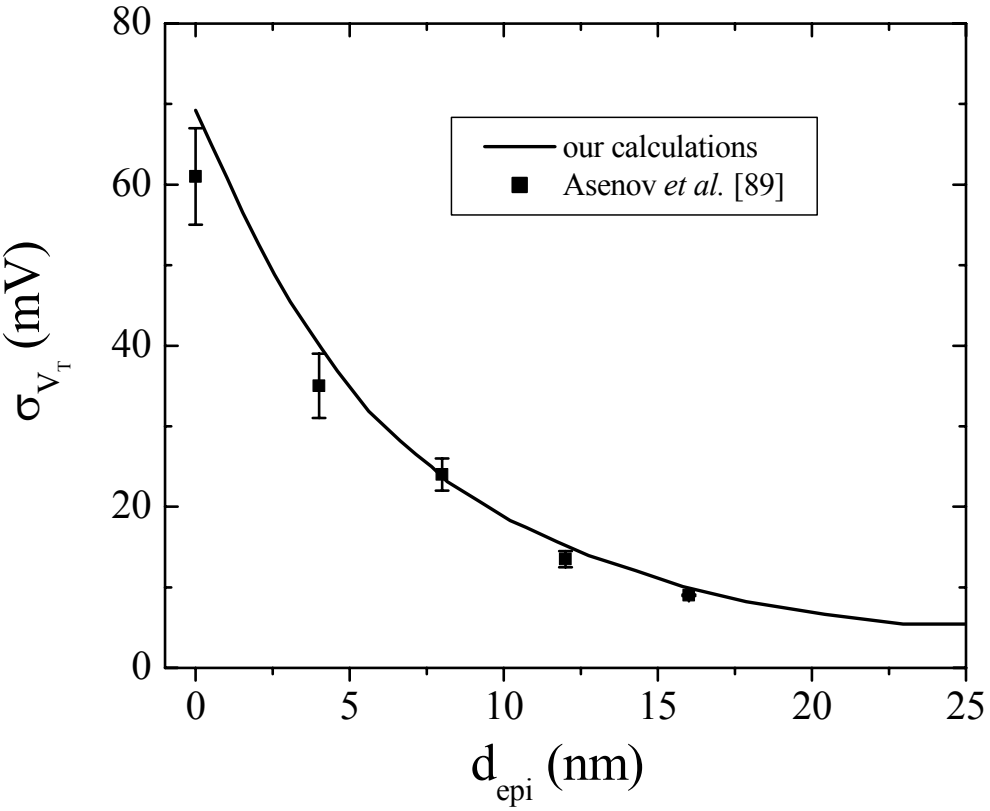

Figure 2.11: Dependence of standard deviation of threshold voltage on thickness of epitaxial layer.

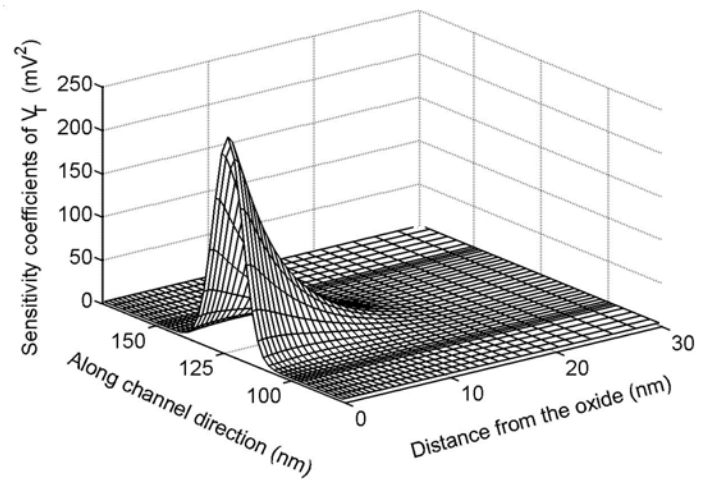

(a)

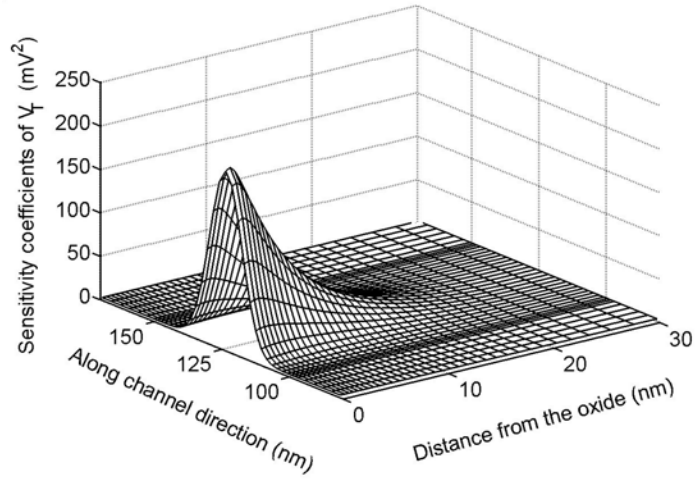

(b)

Figure 2.12: Spatial distribution of doping sensitivity coefficients of V_T for (a) $d_{epi} = 10$ nm and (b) $d_{epi} = 20$ nm. Distribution of sensitivity coefficients is practically insensitive to thickness of epitaxial layer (see Figure 2.3 for the case $d_{epi} = 0$ nm, i.e. no epitaxial layer).

Chapter 3

Analysis of fluctuations of terminal characteristics

This chapter is devoted to the analysis of fluctuations of terminal characteristics in semiconductor devices. The first two sections of the chapter deal with the analysis of I-V characteristics and transconductance in semiconductor devices, respectively. The algebra of superposition coefficients is then introduced and applied to the computation of fluctuations of subthreshold voltage characteristics. Special consideration is given to the analysis of the standard deviation of subthreshold currents and gate-voltage swings in ultrasmall MOSFET devices.

3.1 Fluctuations of I-V characteristics

The study of the fluctuations of I-V characteristics is extremely important for both digital and analog applications. In this section, the linearization method that was introduced for the computation of fluctuations in semiconductor devices in the previous chapter is applied to the computation of variances of terminal currents.

Let us denote the current through terminal α of the semiconductor device by I_α. In order to compute the superposition coefficients of I_α it is convenient to write terminal currents as explicit functions of state vector $\boldsymbol{X}$ and doping concentration $\boldsymbol{D}$:

$$I_\alpha = I^\alpha\left(\boldsymbol{X},\boldsymbol{D}\right). \tag{3.1}$$

The fluctuations of terminal currents can be found by linearizing (3.1) with respect to the fluctuating quantities:

$$\tilde{I}_\alpha = \left(I_{\boldsymbol{X}}^\alpha\right)^t \tilde{\boldsymbol{X}} + \left(I_{\boldsymbol{D}}^\alpha\right)^t \tilde{\boldsymbol{D}}, \tag{3.2}$$

where $I_{\boldsymbol{X}}^\alpha$ and $I_{\boldsymbol{D}}^\alpha$ are the derivatives of I^α with respect to the state variable and doping concentration, while superscript *t* denotes the transpose of the given vector. Since the gate potential is constant, we can write $\tilde{V}_G = 0$ and solve equations (2.23) and (3.2) for the fluctuations of the terminal current:

$$\tilde{I}_\alpha = -\left[\boldsymbol{g}_\alpha^t \cdot \hat{\boldsymbol{F}}_{\boldsymbol{D}} - \left(I_{\boldsymbol{D}}^\alpha\right)^t\right]\cdot \tilde{\boldsymbol{D}} - \left(\boldsymbol{g}_\alpha^t \cdot \hat{\boldsymbol{F}}_t\right)\cdot \tilde{\boldsymbol{t}}, \tag{3.3}$$

where $\boldsymbol{g}_\alpha^t$ is the transpose of column vector $\boldsymbol{g}_\alpha$ and can be found by solving the following linear system of equations:

$$\hat{\boldsymbol{F}}_{\boldsymbol{X}}^t \boldsymbol{g}_\alpha = I_{\boldsymbol{X}}, \tag{3.4}$$

where $\hat{\boldsymbol{F}}_{\boldsymbol{X}}^t$ denotes the transpose of matrix $\hat{\boldsymbol{F}}_{\boldsymbol{X}}$. By comparing (2.18) and (3.3), it can be inferred that the superposition coefficients of the terminal current are given by the following formulas:

$$\gamma_{I_\alpha}^{D_i} = -\left(\boldsymbol{g}_\alpha^t \cdot \hat{\boldsymbol{F}}_{\boldsymbol{D}}\right)_i + \left(I_{\boldsymbol{D}}^\alpha\right)_i^t \tag{3.5}$$

and

$$\gamma_{I_\alpha}^{t_i} = -\left(\boldsymbol{g}_\alpha^t \cdot \hat{\boldsymbol{F}}_t \right)_i . \tag{3.6}$$

The standard deviation of terminal currents can be calculated by using the formulas [see equation (2.18)]:

$$\sigma_{I_\alpha}^2 = \sum_i \left(\gamma_{I_\alpha}^{D_i} \right)^2 \frac{D_{0i}}{\Delta V_i} + \sum_{i,j} \gamma_{I_\alpha}^{t_i} \gamma_{I_\alpha}^{t_j} ACF\left(i, j\right). \tag{3.7}$$

The most expensive computational effort in the calculation of these coefficients is to solve the linear system (3.4). For 2-D simulations we solve this system by using the classical Gauss-Seidel method, while for 3-D simulations we solve it by using the Successive Over-Relaxation (SOR) technique.

Figures 3.2 (a) and (b) summarize our calculations of the variance of saturation currents performed for MOS C (see the Appendix for technical specifications). Figure 3.2(a) exhibits the saturation currents along with the standard deviation of these currents presented by "error bars" computed for various bias conditions. Figure 3.2(b) gives the mesh-independent "sensitivity" coefficients of the drain current. In these calculations we use the model of mobility described in Refs. [89] and [90].

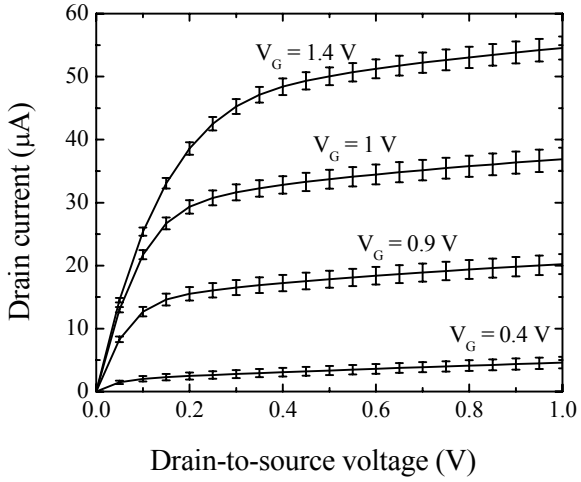

Figure 3.1: Drain current and standard deviation of drain current. Simulations made for MOS C (see the Appendix for technical specifications).

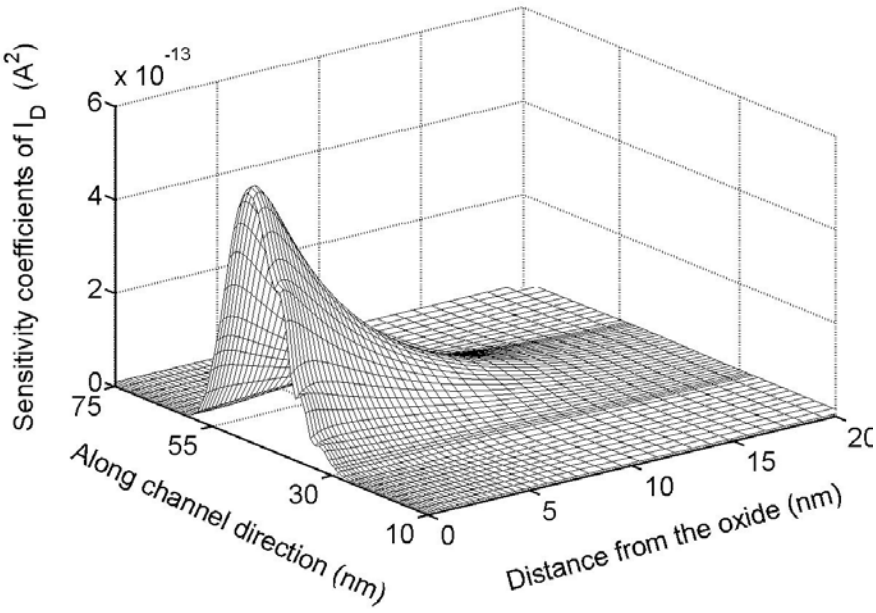

Figure 3.2: Distribution of sensitivity coefficients of drain current for MOS C ($V_{DS} = 1.2\ V$ and $V_{GS} = 0.8\ V$).

3.2 Fluctuations of transconductance

This section presents the basic idea of the method for the calculation of the variance of transconductance in MOSFET devices. It should be noted that similar techniques can also be applied to the computation of variances of other small-signal parameters (e.g. *z*-parameters, hybrid parameters, etc.)

Transconductance is defined as follows:

$$g_m = \left.\frac{i_D}{v_G}\right|_{v_D=0}, \tag{3.8}$$

where i_D represents the small-signal terminal current through the drain, and v_G and v_D are the small-signal potentials on the gate and drain, respectively. In order to find g_m, transport equation (2.19) is linearized around the dc bias values $(\boldsymbol{X}_0, V_{G0})$. If we denote by $\boldsymbol{x}_G$ the infinitesimal change in the state variable induced by v_G, we can write:

$$\hat{\boldsymbol{F}}_{\boldsymbol{X}}\boldsymbol{x}_G + \boldsymbol{F}_{V_G} v_G = 0, \tag{3.9}$$

where the notations have their usual meaning. Current i_D is a linear function of $\boldsymbol{x}_G$, which can be found by linearizing the expression for drain current $I^D(\boldsymbol{X})$ with respect to state variable $\boldsymbol{X}$. This linearization eventually leads to the following expression for transconductance:

$$g_m = \frac{1}{v_G} I_X^D \cdot \boldsymbol{x}_G. \tag{3.10}$$

In the rest of this section we focus on the computation of the standard deviation of transconductance. To simplify our discussion, let us assume that the

effects of the oxide thickness fluctuations are negligible and take into consideration only the random doping fluctuations. As mentioned previously, doping $\boldsymbol{D}$ should be treated as a random field:

$$\boldsymbol{D} = \boldsymbol{D}_0 + \tilde{\boldsymbol{D}}\,,\ \left\langle \tilde{\boldsymbol{D}} \right\rangle = 0\,, \tag{3.11}$$

where $\left\langle \tilde{\boldsymbol{D}} \right\rangle$ denotes the expected value of $\tilde{\boldsymbol{D}}$ and $\boldsymbol{D}_0$ is the average value of the doping. When the fluctuations of the doping occur on very fine spatial scales in comparison with device dimension, the state variables are insensitive to doping fluctuations due to homogenization phenomena. However, for very small devices, doping fluctuations occur on spatial scales comparable with device dimensions and usually induce shifts and fluctuations in the state variable $\boldsymbol{X}$. It is useful to separate the shifts and fluctuations of the dc bias variables from the shifts and fluctuations of the ac components:

$$\boldsymbol{X} = \boldsymbol{X}_0 + \boldsymbol{X}_0^{sh} + \tilde{\boldsymbol{X}}_0 + \boldsymbol{x}_G + \boldsymbol{x}_G^{sh} + \tilde{\boldsymbol{x}}_G\,, \tag{3.12}$$

where $\left\langle \tilde{\boldsymbol{X}}_0 \right\rangle = \left\langle \tilde{\boldsymbol{x}}_G \right\rangle = 0$. By substituting equations (3.11) and (3.12) into transport equation (2.19), as well as by taking into account that $V_G = V_{G0} + v_G$, we obtain:

$$\boldsymbol{F}\left(\boldsymbol{X}_0 + \boldsymbol{X}_0^{sh} + \tilde{\boldsymbol{X}}_0 + \boldsymbol{x}_G + \boldsymbol{x}_G^{sh} + \tilde{\boldsymbol{x}}_G,\ \boldsymbol{D}_0 + \tilde{\boldsymbol{D}},\ V_{G0} + v_G\right) = 0\,. \tag{3.13}$$

To find the variance of transconductance, equation (3.12) is linearized with respect to $\boldsymbol{x}_G$ and to fluctuations $\tilde{\boldsymbol{X}}_0$ and $\tilde{\boldsymbol{x}}_G$. This linearization is justified by the fact that the variances of nonlinear functions of random variables (unlike their "shifted" values) can be determined from linearized equations. Careful linearization of equation

(3.12) reveals that $\boldsymbol{X}_0^{sh}$ and $\boldsymbol{x}_G^{sh}$ are equal to zero within the framework of the first-order approximation (linearization), while $\tilde{\boldsymbol{X}}_0$ and $\tilde{\boldsymbol{x}}_G$ satisfy the following equations:

$$\begin{cases} \hat{\boldsymbol{F}}_{\boldsymbol{X}} \tilde{\boldsymbol{X}}_0 = -\hat{\boldsymbol{F}}_{\boldsymbol{D}} \tilde{\boldsymbol{D}}, \\ \hat{\boldsymbol{F}}_{\boldsymbol{X}} \tilde{\boldsymbol{x}}_G + \hat{\boldsymbol{B}} \tilde{\boldsymbol{X}}_0 = 0. \end{cases} \tag{3.14}$$

In the last equation, $\hat{\boldsymbol{B}}$ is a matrix defined by:

$$\hat{\boldsymbol{B}} = \sum_{i=1}^{3N} \hat{\boldsymbol{F}}_{\boldsymbol{X},X_i} x_{G,i} \,, \tag{3.15}$$

where $\hat{\boldsymbol{F}}_{\boldsymbol{X},X_i} = \dfrac{\partial \hat{\boldsymbol{F}}_{\boldsymbol{X}}}{\partial X_i}$, while X_i and $x_{G,i}$ denote the *i*th component of vectors $\boldsymbol{X}$ and $\boldsymbol{x}_G$, respectively. Matrix $\hat{\boldsymbol{B}}$ is computed at dc bias point $\left(\boldsymbol{X_0}, \boldsymbol{D_0}, V_{G0}\right)$. In the derivation of equation (3.15) it has been taken into account that the doping enters the Poisson equation as a linear term, so the second derivative of the transport equations with respect to the doping disappears. The summation in equation (3.15) is over all *N* mesh points and for each state variable (i.e. the electric potential, the electron and hole concentrations).

The fluctuations of transconductance are caused by fluctuations $\tilde{\boldsymbol{x}}_G$, and can be evaluated by using an equation similar to (3.10):

$$\tilde{g}_m = \frac{1}{v_G} \left\langle I_X^D, \tilde{\boldsymbol{x}}_G \right\rangle + \frac{1}{v_G} \left\langle I_{XX}^D \tilde{\boldsymbol{X}}_0, \boldsymbol{x}_G \right\rangle, \tag{3.16}$$

where I_{XX}^D is the Hessian matrix of the drain current.

It is apparent from equations (3.14) and (3.16) that $\tilde{\boldsymbol{X}}_0$ and $\tilde{\boldsymbol{x}}_G$ are linear with respect to $\tilde{\boldsymbol{D}}$, while $\tilde{g}_m$ is linear with respect to $\tilde{\boldsymbol{X}}_0$ and $\tilde{\boldsymbol{x}}_G$. Consequently, fluctuations of the transconductance can be represented as linear functions of doping fluctuations:

$$\tilde{g}_m = \sum_{i=1}^{N} \gamma_{g_m}^i \tilde{D}_i \,, \tag{3.17}$$

where the sum is taken over all mesh-points. The variance of g_m can now be computed by using a formula similar to (2.18):

$$\sigma_{g_m}^2 = \sum_{i=1}^{N} \left(\gamma_{g_m}^i\right)^2 \frac{D_{0i}}{\Delta V_i} \,. \tag{3.18}$$

The numerical implementation of the computation of variances of transconductance consists of two parts:

(1) computation of superposition coefficients $\gamma_{g_m}^i$, and

(2) computation of variance of g_m by using equation (3.18).

Note that, according to (3.17), a specific coefficient $\gamma_{g_m}^i$ is equal to the value of $\tilde{g}_m$ when $\tilde{D}_i = 1$ and $\tilde{D}_j = 0$, $j \neq i$. This suggests that each element $\gamma_{g_m}^i$ can be found from equation (3.17) after solving the linearized equations (3.14) with respect to $\tilde{\boldsymbol{x}}_G$. To find all superposition coefficients, this approach requires solving the two systems (3.14) of 3*N* equations each, for *N* different right hand sides, which is computationally very expensive. It turns out that there exists a mathematical trick that substantially simplifies these computations and reduces them to solving two linear systems of equations for only one right hand side. In order to explain this trick, consider the formal solution of equation (3.14):

$$\begin{cases} \tilde{\boldsymbol{X}}_0 = -\hat{\boldsymbol{F}}_X^{-1}\left(\hat{\boldsymbol{F}}_D\tilde{\boldsymbol{D}}\right), \\ \tilde{\boldsymbol{x}}_G = \hat{\boldsymbol{F}}_X^{-1}\hat{\boldsymbol{B}}\hat{\boldsymbol{F}}_X^{-1}\left(\hat{\boldsymbol{F}}_D\tilde{\boldsymbol{D}}\right). \end{cases} \tag{3.19}$$

By substituting these formulas into (3.16) and by considering $v_G = 1$, we find:

$$\tilde{g}_m = \left\langle I_X^D, \tilde{\boldsymbol{x}}_G \right\rangle + \left\langle I_{XX}^D \tilde{\boldsymbol{X}}_0, \boldsymbol{x}_G \right\rangle = \left\langle I_X^D, \hat{\boldsymbol{F}}_X^{-1}\hat{\boldsymbol{B}}\hat{\boldsymbol{F}}_X^{-1}\hat{\boldsymbol{F}}_D\tilde{\boldsymbol{D}} \right\rangle - \left\langle I_{XX}^D \hat{\boldsymbol{F}}_X^{-1}\left(\hat{\boldsymbol{F}}_D\tilde{\boldsymbol{D}}\right), \boldsymbol{x}_G \right\rangle$$

$$= \left\langle \left(\hat{\boldsymbol{F}}_X^t\right)^{-1}\hat{\boldsymbol{B}}^t\left(\hat{\boldsymbol{F}}_X^t\right)^{-1} I_X^D, \hat{\boldsymbol{F}}_D\tilde{\boldsymbol{D}} \right\rangle - \left\langle \left(\hat{\boldsymbol{F}}_X^t\right)^{-1}\left(I_{XX}^D\right)^t \boldsymbol{x}_G, \hat{\boldsymbol{F}}_D\tilde{\boldsymbol{D}} \right\rangle, \tag{3.20}$$

where superscript "*t*" denotes the transpose of a matrix. By introducing the notation

$$\boldsymbol{f} = \left(\hat{\boldsymbol{F}}_X^t\right)^{-1}\hat{\boldsymbol{B}}^t\left(\hat{\boldsymbol{F}}_X^t\right)^{-1} I_X^D - \left(\hat{\boldsymbol{F}}_X^t\right)^{-1}\left(I_{XX}^D\right)^t \boldsymbol{x}_G, \tag{3.21}$$

equation (3.20) can be written as follows:

$$\tilde{g}_m = \left\langle \boldsymbol{f}, \hat{\boldsymbol{F}}_D\tilde{\boldsymbol{D}} \right\rangle, \tag{3.22}$$

while the derivatives of the drain current can be computed by using:

$$I_X^D = \hat{\boldsymbol{F}}_X^t\left(\hat{\boldsymbol{B}}^t\right)^{-1}\left(\hat{\boldsymbol{F}}_X^t\boldsymbol{f} + I_{XX}^D\boldsymbol{x}_G\right). \tag{3.23}$$

By introducing the vector

$$\boldsymbol{g} = \left(\hat{\boldsymbol{B}}^t\right)^{-1}\left(\hat{\boldsymbol{F}}_X^t\boldsymbol{f} + I_{XX}^D\boldsymbol{x}_G\right), \tag{3.24}$$

equation (3.23) can be split as follows:

$$\begin{cases} \hat{\boldsymbol{F}}_X^t\boldsymbol{g} = I_X^D, \\ \hat{\boldsymbol{F}}_X^t\boldsymbol{f} = \hat{\boldsymbol{B}}^t\boldsymbol{g} - I_{XX}^D\boldsymbol{x}_G. \end{cases} \tag{3.25}$$

The first equation in (3.25) must be solved for $\boldsymbol{g}$ and the second equation for $\boldsymbol{f}$. Then, the values of $\tilde{g}_m$ can be computed from equation (3.22) for as many vectors $\tilde{\boldsymbol{D}}$

as needed. It is obvious that by solving equations (3.25) and by using formula (3.22), numerous solutions of system (3.14) can be avoided.

The algorithm for the calculation of transconductance variance can be summarized as follows:

(1) First, transport equation (2.19) is solved to find the dc bias conditions throughout the device.

(2) Second, equation (3.9) is solved and formula (3.10) is used to find the value of transconductance.

(3) Then, matrix $\hat{\boldsymbol{B}}$ is constructed by using formula (3.15) and equations (3.25) are solved for $\boldsymbol{g}$ and $\boldsymbol{f}$.

(4) Next, formula (3.22) is used to find the values of the superposition coefficients:

$$\gamma_{g_m}^{i} = \left\langle \boldsymbol{f}, \hat{\boldsymbol{F}}_{\boldsymbol{D}} \boldsymbol{\delta}^{(i)} \right\rangle, \tag{3.26}$$

where $\boldsymbol{\delta}^{(i)}$ is a vector that has the *i*th component equal to 1, while all other components are equal to zero.

(5) Finally, the variance of transconductance is found from equation (3.18).

In our simulations, the transport equations have been discretized by using the finite-difference method. The Sharfetter-Gummel finite difference scheme has been applied to the discretization of current-continuity equations. Gummel's block iteration method has been used in order to decouple the Poisson and drift-diffusion equations. The decoupled nonlinear Poisson and current continuity equations have been solved by using the iterative techniques discussed in [85] and [86]. These iterative techniques

are globally convergent and can be implemented with modest computer memory requirements. The numerical solution of equations (3.9) has been performed by using the standard LU factorization techniques and the Gauss-Seidel type iterative techniques that exploit the "diagonal dominance" of the matrix equation structure. Similar numerical techniques have been used to find the solution of coupled equations (3.25). Our calculations revealed that the LU decomposition techniques are more efficient for 2-D problems, while the iterative techniques are significantly faster in 3-D simulations.

Finally, it should be noted that equations similar to (3.14)-(3.26) can be written for the computation of the standard deviation of transconductance induced by random oxide thickness fluctuations. The only modification to equations (3.14)-(3.26) is that the doping concentration vector $\boldsymbol{D}$ should be replaced with the oxide thickness vector $\boldsymbol{t}$.

3.3 Algebra of superposition coefficients

In this section we discuss a powerful technique that will allow us to compute the superposition coefficients of many device parameters very efficiently. Let us consider some parameter C of the device that can be written as a function of two other parameters A and B:

$$C = f\left(A, B\right). \tag{3.27}$$

We assume that parameters A and B fluctuate from one device to another due to random doping oxide thickness fluctuations. Such an example will be analyzed in the

next section, where the gate-voltage swing of a MOSFET device is written as a function of the drain current and transconductance by using the formula $S = \frac{I_D}{g_m} \ln 10$.

Now, let us show that if we know the superposition coefficients of parameters *A* and *B*, we can compute the superposition coefficients of *C* by using simple transformation relations.

All parameters (A, B, and C) can be expressed (in the first-order approximation) as the sum of their average values and some fluctuating terms, which are induced by the random doping concentration and oxide roughness:

$$A = A_0 + \sum_{i=1}^{N} \gamma_A^{D_i} \tilde{D}_i + \sum_{i=1}^{N_{ox}} \gamma_A^{t_i} \tilde{t}_i \,, \tag{3.28}$$

$$B = B_0 + \sum_{i=1}^{N} \gamma_B^{D_i} \tilde{D}_i + \sum_{i=1}^{N_{ox}} \gamma_B^{t_i} \tilde{t}_i \,, \tag{3.29}$$

and

$$C = C_0 + \sum_{i=1}^{N} \gamma_C^{D_i} \tilde{D}_i + \sum_{i=1}^{N_{ox}} \gamma_C^{t_i} \tilde{t}_i \,. \tag{3.30}$$

By introducing equations (3.28)-(3.30) in (3.27), we obtain:

$$C_0 + \sum_{i=1}^{N} \gamma_C^{D_i} \tilde{D}_i + \sum_{i=1}^{N_{ox}} \gamma_C^{t_i} \tilde{t}_i = f\left[A_0 + \sum_{i=1}^{N} \gamma_A^{D_i} \tilde{D}_i + \sum_{i=1}^{N_{ox}} \gamma_A^{t_i} \tilde{t}_i,\; B_0 + \sum_{i=1}^{N} \gamma_B^{i} \tilde{D}_i + \sum_{i=1}^{N_{ox}} \gamma_B^{t_i} \tilde{t}_i \right]$$

$$\simeq f\left(A_0, B_0\right) + \frac{\partial f}{\partial A}\left(A_0, B_0\right)\left(\sum_{i=1}^{N} \gamma_A^{i} \tilde{D}_i + \sum_{i=1}^{N_{ox}} \gamma_A^{t_i} \tilde{t}_i \right) + \frac{\partial f}{\partial B}\left(A_0, B_0\right)\left(\sum_{i=1}^{N} \gamma_B^{i} \tilde{D}_i + \sum_{i=1}^{N_{ox}} \gamma_B^{t_i} \tilde{t}_i \right), \tag{3.31}$$

where we have taken into account that parameter fluctuations are assumed to be small. Since $C_0 = f\left(A_0, B_0\right)$, equation (3.31) leads to:

$$\sum_{i=1}^{N}\gamma_C^{D_i}\tilde{D}_i+\sum_{i=1}^{N_{ox}}\gamma_C^{t_i}\tilde{t}_i=$$

$$=\frac{\partial f}{\partial A}(A_0,B_0)\left(\sum_{i=1}^{N}\gamma_A^i\tilde{D}_i+\sum_{i=1}^{N_{ox}}\gamma_A^{t_i}\tilde{t}_i\right)+\frac{\partial f}{\partial B}(A_0,B_0)\left(\sum_{i=1}^{N}\gamma_B^i\tilde{D}_i+\sum_{i=1}^{N_{ox}}\gamma_B^{t_i}\tilde{t}_i\right). \quad (3.32)$$

Equation (3.32) is valid for any doping and oxide thickness configurations. This implies:

$$\gamma_C^{D_i}=\frac{\partial f}{\partial A}(A_0,B_0)\gamma_A^{D_i}+\frac{\partial f}{\partial B}(A_0,B_0)\gamma_B^{D_i} \quad (3.33)$$

and

$$\gamma_C^{t_i}=\frac{\partial f}{\partial A}(A_0,B_0)\gamma_A^{t_i}+\frac{\partial f}{\partial B}(A_0,B_0)\gamma_B^{t_i}. \quad (3.34)$$

Equations (3.33) and (3.34) can be used to compute the superposition coefficients of parameter C if we know the superposition coefficients of A and B. It is clear that these equations can be easily extended to the case when parameter C depends on more than two variables (e.g. $C=f(A_1,A_2,...)$). In this case, the sums in (3.33) and (3.34) should be taken over all variables A_1, A_2,… .

In the end of this section, let us consider two examples which will later be used for the computation of the gain voltage swing and frequency characteristics.

(1) Consider parameter C that can be written as $C=\frac{A}{B}$. Direct application of formula (3.33) leads to:

$$\gamma_C^{D_i}=\frac{A_0}{B_0}\left(\frac{\gamma_A^{D_i}}{A_0}-\frac{\gamma_B^{D_i}}{B_0}\right). \quad (3.35)$$

(2) Consider now parameter $C = |Q| = |A + jB|$, where $j = \sqrt{-1}$. By using the same technique we can find that:

$$\gamma_C^{D_i} = \frac{A_0 \gamma_A^{D_i} + B_0 \gamma_B^{D_i}}{\sqrt{A_0^2 + B_0^2}} = \frac{\mathrm{Re}\left(Q_0^* \gamma_Q^{D_i}\right)}{|Q_0|}, \tag{3.36}$$

where $\gamma_Q^{D_i}$ are the superposition coefficients of $Q = A + jB$.

In formulas (3.35) and (3.36), $\gamma_C^{D_i}$ are the doping superposition coefficients of parameter C. Similar formulas can be written for the oxide thickness superposition coefficients. As a first application of the algebra of superposition coefficients, we consider in the following section the computation of fluctuations of subthreshold voltage characteristics.

3.4 Fluctuations of subthreshold voltage characteristics

The subthreshold regime of MOSFET devices is usually characterized by the subthreshold current I_{SUB} and the gate-voltage swing (S-factor). Due to the exponential dependence of the subthreshold current on the surface potential [91], [92], the subthreshold region is particularly sensitive to doping profile fluctuations, and both I_{SUB} and the S-factor are strongly dependent on the fluctuations of the doping in the channel. Therefore, special attention must be paid to the characterization of fluctuations in the subthreshold voltage region. This section presents the method for the calculation of the variance of subthreshold currents and gate-voltage swing.

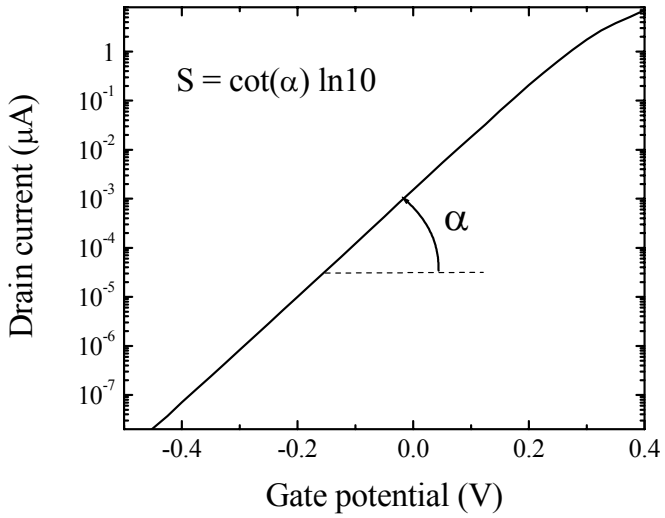

Figure 3.3: Subthreshold current for MOS C (see the Appendix for technical specifications). Drain-to-source voltage is V_{DS} = 0.5 V.

The gate-voltage swing is defined by the formula:

$$S = \frac{dV_G}{d\left(\log_{10} I_D\right)} \tag{3.37}$$

and can be interpreted as the change of gate potential required to decrease the drain current by one decade (see Figure 3.3). Equation (3.37) can be written in a more convenient form, as a function of the subthreshold current (I_{SUB}) and transconductance (g_m):

$$S = \frac{I_{SUB}}{g_m} \ln 10 \,. \tag{3.38}$$

Note that the superposition coefficients of the subthreshold current ($\gamma^i_{I_{SUB}}$) and transconductance ($\gamma^i_{g_m}$) can be identified with the methods presented in sections 3.1

and 3.2. Therefore, the algebra of superposition coefficients [see equation (3.35)] can be readily applied to calculate the superposition coefficients of the gate-voltage swing by using the following equation:

$$\gamma_S^i = \frac{I_{SUB0}}{g_{m0}}\left(\frac{\gamma_{I_{SUB}}^i}{I_{SUB0}} - \frac{\gamma_{g_m}^i}{g_{m0}}\right)\ln 10 . \qquad (3.39)$$

Equations (3.39) and (2.18) have been applied to the computation of the standard deviation of the gate-voltage swing for MOSFET devices.

The sensitivity coefficients of the subthreshold current are represented in Figure 3.4(a) for MOS C (see the Appendix for technical specifications). In these simulations, the source and the base were grounded, while $V_D = 0.1$ V and $V_G = 0$ V. One can easily see that the fluctuations of the doping at different locations inside the semiconductor device contribute differently to the fluctuations of subthreshold current. The most sensitive region (the region that by and large contributes to the fluctuations of I_{SUB}) is located in the conduction channel and in the close proximity of the oxide-semiconductor interface. In order to suppress the fluctuations of the subthreshold current in MOSFET devices, we need to control the doping concentration in the conduction channel as much as possible.

Figure 3.4(b) presents the values of the sensitivity coefficients of the gate-voltage swing for the same MOSFET device as in Figure 3.4(a). In contrast with the sensitivity coefficients of I_{SUB}, in this case, the most sensitive regions are located at the drain and source junctions, and in the vicinity of the dioxide interface.

The standard deviation of the gate-voltage swing is heavily dependent on the bias conditions. This fact is apparent from Figure 3.5, where the values of the gate-voltage swing are presented by continuous lines, while their standard deviations are shown by vertical bars. Note from this figure that there are significant fluctuations of the gate-voltage swing for relatively large (close to threshold voltage) values of the gate voltage. The standard deviations of these fluctuations decrease for low values of the gate and the drain-to-source voltage.

We have also investigated the dependence of the fluctuations of the subthreshold voltage swing on the average doping concentration and oxide thickness. Figure 3.6(a) presents the dependence of S on the doping concentration N_a. We can see that for large values of the doping concentration, the fluctuations of the gate-voltage swing are approximately constant. For small values of the average doping concentration, the gate voltage becomes comparable to the value of the threshold voltage and, consequently, the average value and the standard deviation of the gate-voltage swing increase.

Figure 3.6(b) presents the dependence of the gate-voltage swing on the thickness of the oxide layer. We can see that S and σ_S increase almost linearly with the oxide thickness. Similar linear dependences on the oxide thickness have also been observed for the standard deviations of the threshold voltage and saturation current, as well as for certain small-signal parameters.

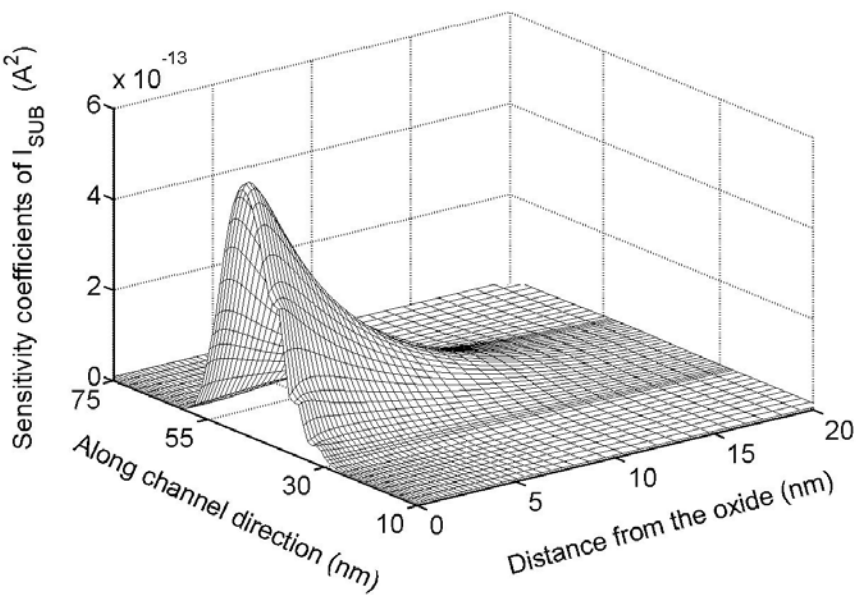

(a)

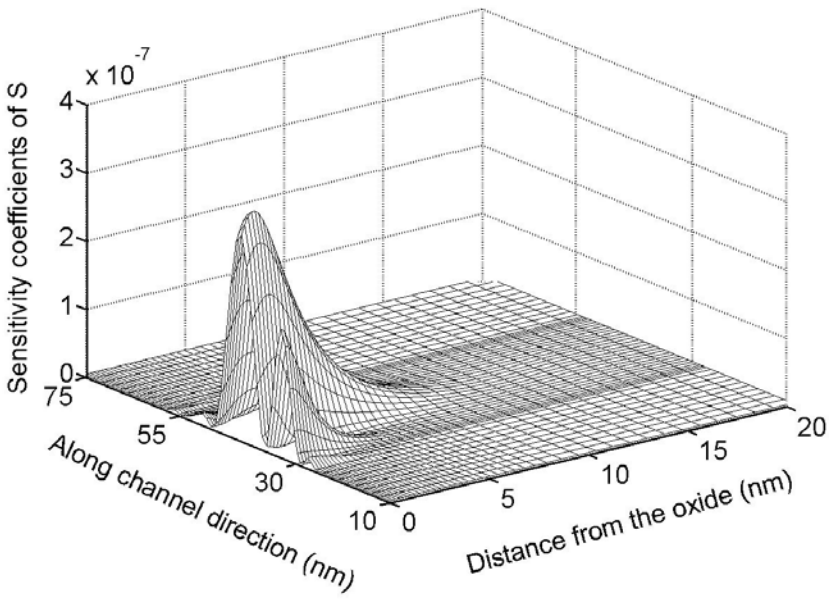

(b)

Figure 3.4: Sensitivity coefficients of subthreshold current (a) and gate-voltage swing (b) for MOS C (V_G = 0 V and V_{DS} = 1.2 V).

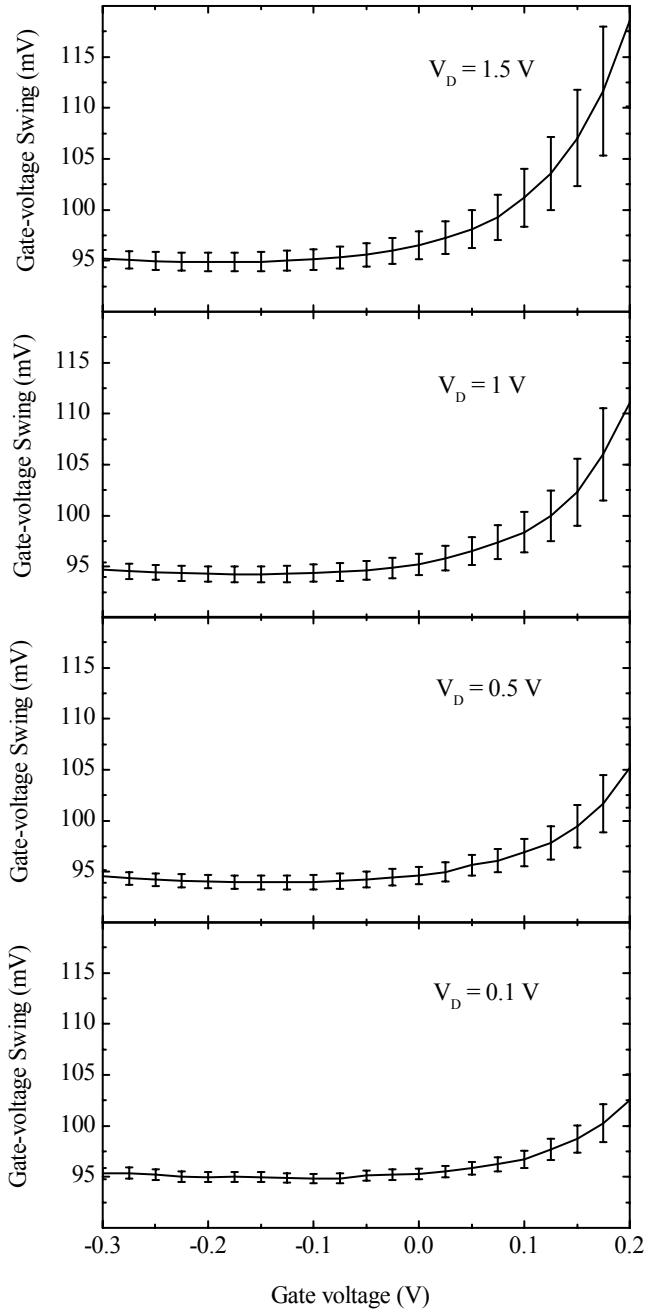

Figure 3.5: Gate-voltage swing of MOS C as function of gate voltage for different values of drain-to-source voltage: V_D=0.1 V, 0.5 V, 1 V, and 1.5 V. Vertical bars indicate standard deviations.

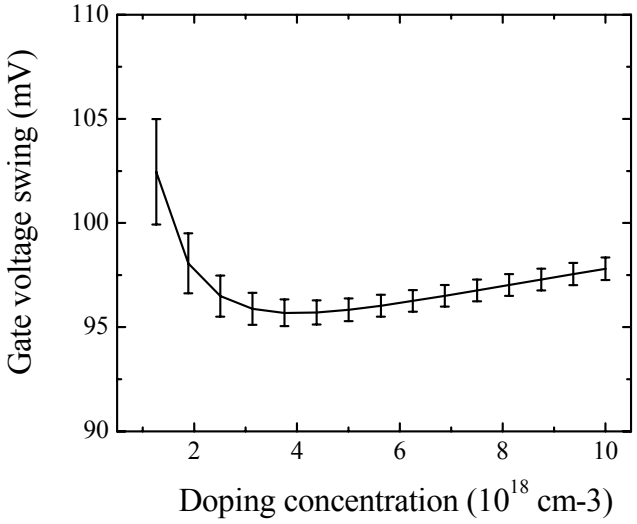

(a)

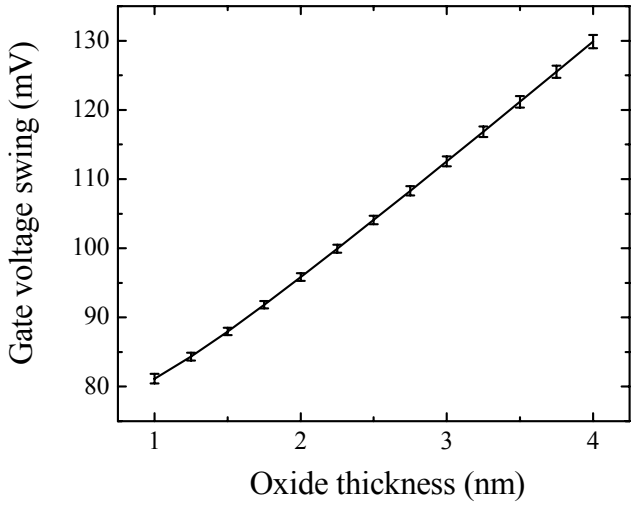

(b)

Figure 3.6: Gate-voltage swing as function of average doping concentration in channel (a) and oxide thickness (b) for MOS C. Vertical bars indicate standard deviations of gate-voltage swing.

Chapter 4

Analysis of fluctuations of frequency characteristics

This chapter is devoted to the analysis of fluctuations of frequency characteristics in semiconductor devices. The main emphasis is placed on the analysis of small-signal parameters (Sections 4.1 and 4.2), gain factors (Section 4.3), and cut-off frequencies (Section 4.4). However, techniques similar to the ones presented in this chapter can be applied to the analysis of fluctuations of other frequency characteristics of semiconductor devices.

4.1 Fluctuations of admittance parameters (*y*-parameters)

In this section we introduce the technique for the calculation of variances of admittance matrix elements (i.e. variances of *y*-parameters). This technique closely mimics the method for the analysis of fluctuations of transconductance that was presented in Section 3.2.

The admittance matrix elements for an *N*-terminal device are defined as follows [93]:

$$y_{\beta\alpha} = \left.\frac{i_\beta}{v_\alpha}\right|_{v_\gamma = 0,\ \gamma \neq \beta}, \ \alpha, \beta, \gamma = 1,..,N, \tag{4.1}$$

where i_β and v_α represent the small-signal phasor terminal current and potential at terminals β and α, respectively. In the case of MOSFET, instead of subscripts α, β, and γ, subscript G will be used for gate, D for drain, S for source, and B for body.

We find the variances of *y*-parameters in three steps:

(1) First, we solve the transport equations and find the dc bias point.

(2) Then, we solve the linearized transport equations and find the values of *y*-parameters.

(3) Finally, we find the superposition coefficients and the variances of *y*-parameters.

Each of these steps is discussed below.

A. Finding dc bias point

The first step in the evaluation of variances of *y*-parameters is to solve the transport equations and to find the dc bias point of the device. To this end, consider the spatially discretized transport equations [82] in the form:

$$\frac{d}{dt}\boldsymbol{J}(\boldsymbol{X}) + \boldsymbol{F}(\boldsymbol{X}, \boldsymbol{D}, V_\alpha, V_\beta, ...) = 0, \tag{4.2}$$

where $\boldsymbol{F}$ is a nonlinear vector function of the unknown "state" vector $\boldsymbol{X}$, doping vector $\boldsymbol{D}$, and terminal potentials, while $\boldsymbol{J}$ is a vector function which depends on $\boldsymbol{X}$

only. If the transport model is the drift-diffusion model, then state vector $\boldsymbol{X}$ consists of three vectors $\boldsymbol{\varphi}$, $\boldsymbol{n}$, and $\boldsymbol{p}$, whose components are the mesh-point values of the electric potential, electron and hole densities, respectively. In equation (4.2), we have separated the explicit time-dependent part of the transport equations (which in the case of the drift-diffusion model comes from the terms $\partial n/\partial t$ and $\partial p/\partial t$ in the current transport equations) from the time-independent part $\boldsymbol{F}$. In the computations of dc bias conditions, equations (4.2) are reduced to:

$$\boldsymbol{F}\left(\boldsymbol{X_0}, \boldsymbol{D_0}, V_{\alpha 0}, V_{\beta 0}, \ldots\right) = 0 . \tag{4.3}$$

Given some doping distribution $\boldsymbol{D_0}$ and the bias voltages $V_{\alpha 0}, V_{\beta 0}, \ldots$, equation (4.3) can be solved to find the state vector $\boldsymbol{X_0}$.

B. Finding the values of *y*-parameters

The second step is to find the values of the admittance matrix elements (*y*-parameters). It is customary to assume that a sinusoidal voltage of infinitesimal amplitude v_α is applied to the α-terminal, while all other terminals are kept at constant dc potentials:

$$V_\alpha = V_{\alpha 0} + v_\alpha e^{j\omega t} . \tag{4.4}$$

This will induce ac perturbations in the state variables:

$$\boldsymbol{X} = \boldsymbol{X}_0 + \boldsymbol{x}_\alpha e^{j\omega t} , \tag{4.5}$$

The governing equations for the ac component of the state variables $\boldsymbol{x}_\alpha$ can be found by linearizing equation (4.2) around the dc bias values $\boldsymbol{X}_0$ and $V_{\alpha 0}$ [94]:

$$\left(j\omega \hat{\boldsymbol{J}}_X + \hat{\boldsymbol{F}}_X\right)\boldsymbol{x}_\alpha + \boldsymbol{F}_{V_\alpha} v_\alpha = 0 , \tag{4.6}$$

In this equation, $\hat{\boldsymbol{J}}_X$ and $\hat{\boldsymbol{F}}_X$ are the Jacobian matrices of $\boldsymbol{J}$ and $\boldsymbol{F}$ computed with respect to variable $\boldsymbol{X}$ (and evaluated at the dc bias point), while $\boldsymbol{F}_{V_\alpha} = \dfrac{\partial \boldsymbol{F}}{\partial V_\alpha}$. In general, $\hat{\boldsymbol{J}}_X$ and $\hat{\boldsymbol{F}}_X$ are $3N \times 3N$ sparse matrices, where N is the number of mesh points.

The current through the $\beta-$terminal is given by some function $I^\beta(\boldsymbol{X})$. In the first-order approximation, the ac component of the current is:

$$i_\beta = \nabla I^\beta\big|_{X_0} \cdot \boldsymbol{x}_\alpha = \left\langle \nabla I^\beta\big|_{X_0}, \boldsymbol{x}_\alpha^* \right\rangle = \left\langle I_X^\beta, \boldsymbol{x}_\alpha^* \right\rangle, \tag{4.7}$$

where $\langle\ \rangle$ stands for the inner product, $I_X^\beta = \nabla I^\beta\big|_{X_0}$, and $\boldsymbol{x}_\alpha^*$ is the complex conjugate of $\boldsymbol{x}_\alpha$. The admittance matrix elements can now be written as:

$$y_{\beta\alpha} = \frac{1}{v_\alpha}\left\langle I_X^\beta, \boldsymbol{x}_\alpha^* \right\rangle. \tag{4.8}$$

This equation can be used to calculate the values of admittance matrix elements.

C. Finding the variances of *y*-parameters

To simplify the discussion, let us assume that the effects of the oxide thickness fluctuations are negligible and let us take into consideration only the random doping fluctuations:

$$\boldsymbol{D} = \boldsymbol{D}_0 + \tilde{\boldsymbol{D}},\ \left\langle \tilde{\boldsymbol{D}} \right\rangle = 0, \tag{4.9}$$

where $\left\langle \tilde{\boldsymbol{D}} \right\rangle$ denotes the expected value of $\tilde{\boldsymbol{D}}$, and $\boldsymbol{D}_0$ is the average value of the doping. The random doping fluctuations will induce fluctuations $\tilde{\boldsymbol{X}}_0$ and $\tilde{\boldsymbol{x}}_\alpha$ in the dc

and ac components of the state variables, respectively. We use a procedure similar to the one used for the derivation of system (3.14), to shown that:

$$\begin{cases} \hat{\boldsymbol{F}}_{\boldsymbol{X}}\tilde{\boldsymbol{X}}_0 = -\hat{\boldsymbol{F}}_{\boldsymbol{D}}\tilde{\boldsymbol{D}}, \\ \hat{\boldsymbol{A}}\tilde{\boldsymbol{x}}_\alpha + \hat{\boldsymbol{B}}\tilde{\boldsymbol{X}}_0 = 0, \end{cases} \tag{4.10}$$

where the following matrix notations have been adopted:

$$\hat{\boldsymbol{A}} = j\omega\hat{\boldsymbol{J}}_{\boldsymbol{X}} + \hat{\boldsymbol{F}}_{\boldsymbol{X}}, \tag{4.11}$$

$$\hat{\boldsymbol{B}} = \sum_{i=1}^{3N}\left(j\omega\hat{\boldsymbol{J}}_{\boldsymbol{X},X_i} + \hat{\boldsymbol{F}}_{\boldsymbol{X},X_i}\right)x_{\alpha,i}. \tag{4.12}$$

Here: $\hat{\boldsymbol{J}}_{\boldsymbol{X},X_i} = \dfrac{\partial\hat{\boldsymbol{J}}_{\boldsymbol{X}}}{\partial X_i}$, $\hat{\boldsymbol{F}}_{\boldsymbol{X},X_i} = \dfrac{\partial\hat{\boldsymbol{F}}_{\boldsymbol{X}}}{\partial X_i}$, while X_i and $x_{\alpha,i}$ denote the ith component of vectors $\boldsymbol{X}$ and $\boldsymbol{x}_\alpha$, respectively. Both matrices $\hat{\boldsymbol{A}}$ and $\hat{\boldsymbol{B}}$ are computed at the dc bias point $\left(\boldsymbol{X_0}, \boldsymbol{D_0}, V_{\alpha 0}\right)$.

Once system (4.10) is solved for $\tilde{\boldsymbol{x}}_\alpha$, we can find the fluctuations of admittance matrix elements by using the formula $\tilde{y}_{\beta\alpha} = \dfrac{1}{v_G}\left\langle I_{\boldsymbol{X}}^{\beta}, \tilde{\boldsymbol{x}}_\alpha^* \right\rangle + \dfrac{1}{v_G}\left\langle I_{\boldsymbol{XX}}^{\beta}\tilde{\boldsymbol{X}}_0, \boldsymbol{x}_\alpha^* \right\rangle$, where $I_{\boldsymbol{XX}}^{\beta}$ is the Hessian matrix of the current through terminal β. The last equation is linear with respect to $\tilde{\boldsymbol{X}}_0$ and $\tilde{\boldsymbol{x}}_\alpha$ while, according to equations (4.10), $\tilde{\boldsymbol{X}}_0$ and $\tilde{\boldsymbol{x}}_\alpha$ are linear with respect to $\tilde{\boldsymbol{D}}$. This means that $\tilde{y}_{\beta\alpha}$ can also be evaluated as a linear combination of the fluctuations of doping at different mesh-points:

$$\tilde{y}_{\beta\alpha} = \sum_{i=1}^{N}\gamma_{\beta\alpha}^{i}\tilde{D}_i, \tag{4.13}$$

where $\gamma^i_{\beta\alpha}$ are the superposition coefficients of $y_{\beta\alpha}$. Assuming that $\tilde{D}_i$ are independent Poisson random variables and by using the relation between the variance and the expected value of the Poisson random variable [95] (see Section 3.2), the variance of $y_{\beta\alpha}$ can be evaluated as:

$$\sigma^2_{y_{\beta\alpha}} = \sum_{i=1}^{N} \left(\gamma^i_{\beta\alpha}\right)^2 \sigma^2_{D_i} = \sum_{i=1}^{N} \left(\gamma^i_{\beta\alpha}\right)^2 \frac{D_{0i}}{\Delta V_i} = \sum_{i=1}^{N} S^i_{\beta\alpha} \Delta N_{0i}\,, \tag{4.14}$$

where D_{0i} is the average value of the doping at mesh point *i,* ΔN_{0i} is the expected number of doping ions in volume ΔV_i, and $S^i_{\beta\alpha}$ are the "sensitivity" coefficients, which are defined as:

$$S^i_{\beta\alpha} = \left(\frac{\gamma^i_{\beta\alpha}}{\Delta V_i}\right)^2. \tag{4.15}$$

The problem of the computation of variances of *y*-parameters is reduced to the computation of superposition coefficients. It is apparent from formula (4.13) that the coefficient $\gamma^i_{\beta\alpha}$ is equal to the value of $\tilde{y}_{\beta\alpha}$ when $\tilde{D}_i = 1$ and $\tilde{D}_j = 0$, $j \neq i$. Thus, in order to find all *N* superposition coefficients, we have to solve the linear systems (4.10) *N* times, for different right hand sides $\tilde{\boldsymbol{D}}$. However, we observe that the same mathematical trick that was used for the computation of the superposition coefficients of transconductance (see Section 3.2) can be applied for the computation the of superposition coefficients of $\gamma_{\beta\alpha}$. By using the same line of reasoning as in Section 3.2, we can write:

$$\gamma^i_{\beta\alpha} = \left\langle \boldsymbol{f}, \left(\hat{\boldsymbol{F}}_{\boldsymbol{D}} \boldsymbol{\delta}^{(i)}\right)^* \right\rangle, \tag{4.16}$$

where, by definition, $\boldsymbol{\delta}^{(i)}$ is a vector whose ith component is one while all other components are equal to zero and $\boldsymbol{f}$ is the solution of the following system of linear equations:

$$\begin{cases} \hat{\boldsymbol{A}}^t \boldsymbol{g} = I_X^\beta, \\ \hat{\boldsymbol{F}}_X^t \boldsymbol{f} = \hat{\boldsymbol{B}}^t \boldsymbol{g} - I_{XX}^\beta \boldsymbol{x}_\alpha. \end{cases} \tag{4.17}$$

The first equation in (4.17) must be solved for $\boldsymbol{g}$ and the second equation for $\boldsymbol{f}$. Then, the values of the superposition coefficients can be computed by using formula (4.16).

The algorithm for the calculation of admittance matrix variances can be summarized as follows:

(1) First, the nonlinear equations (4.3) are solved to find the dc bias conditions throughout the device.

(2) Second, equations (4.6) are solved and formulas (4.8) are used to find the values of the admittance matrix elements.

(3) Then, matrices $\hat{\boldsymbol{A}}$ and $\hat{\boldsymbol{B}}$ are constructed by using formulas (4.11) and (4.12), respectively, and equations (4.17) are solved for $\boldsymbol{g}$ and $\boldsymbol{f}$.

(4) Then, formula (4.16) is used to find the values of the superposition coefficients.

(5) Finally, the variances of the admittance elements are found from equation (4.14).

This algorithm has been implemented and applied to the computation of the admittance matrix variance for MOSFET devices. It is worth noting that the most computationally expensive steps in the algorithm are (1) and (2), which take about

90% of the total computation time. Steps (3), (4), and (5) take about 10% of the total computation time.

Figure 4.1 presents the sensitivity coefficients of *y*-parameters for the 25 nm channel length MOSFET device described in the Appendix (MOS C). The channel extends between 30 nm and 55 nm, while the drain and the source regions correspond to $x > 55$ nm and $x < 30$ nm, respectively. The bias point in these simulations is given by $V_S = V_B = 0$ V, $V_G =$ 0.8 V, and $V_D =$ 1.2 V, while the operating frequency is 10 GHz. One can easily see that the fluctuations of the doping at different locations inside the semiconductor device contribute differently to the fluctuations of *y*-parameters. In most cases, the most sensitive regions are located in the conduction channel and in the direct proximity of the oxide-semiconductor interface. For example, the main cause of the fluctuations of $\mathrm{Im}(y_{GG})$ (gate capacitance) and $\mathrm{Re}(y_{DD})$ are the fluctuations of the doping concentration in the middle of the conduction channel. In the case of other admittance matrix parameters, there are two distinct regions that contribute to the fluctuations of these elements: the first one is located in the middle of the conduction channel and the other one is localized close to the drain-channel junction.

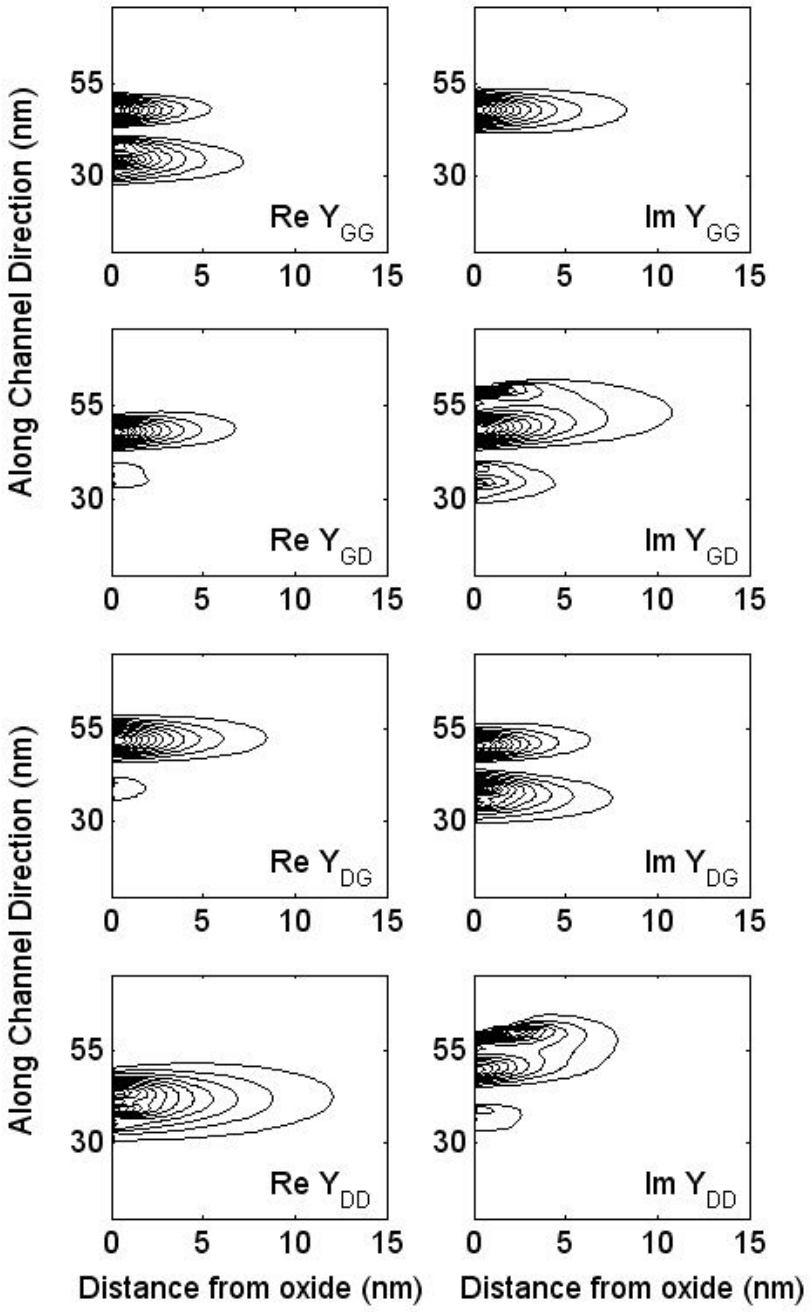

Figure 4.1: Contour plot representation of sensitivity coefficients for *y*-parameters (MOS C).

4.2 Fluctuations of other small-signal parameters

The algebra of superposition coefficients presented in Section 3.3 allows for the direct computation of variances of other small-signal parameters, once the superposition coefficients of *y*-parameters are found. Consider, for example, the computation of variances of impedance parameters (*z*-parameters) that are related to *y*-parameters as follows:

$$z_{\alpha\alpha} = \frac{y_{\beta\beta}}{\Delta},\ z_{\alpha\beta} = -\frac{y_{\alpha\beta}}{\Delta},\ \alpha \neq \beta, \tag{4.18}$$

where $\Delta = y_{\alpha\alpha} y_{\beta\beta} - y_{\alpha\beta} y_{\beta\alpha}$. By using equations (3.33) and (3.34) we find that the superposition coefficients of the impedance parameters are:

$$\gamma^i_{z_{\alpha\alpha}} = z_{\alpha\alpha}\left(\frac{\gamma^i_{y_{\alpha\alpha}}}{y_{\beta\beta}} - \frac{\gamma^i_{\Delta}}{\Delta}\right),\ \gamma^i_{z_{\alpha\beta}} = z_{\alpha\beta}\left(-\frac{\gamma^i_{y_{\alpha\beta}}}{y_{\alpha\beta}} + \frac{\gamma^i_{\Delta}}{\Delta}\right) \tag{4.19}$$

where $\alpha \neq \beta$ and $\gamma^i_{\Delta} = y_{\alpha\alpha}\gamma^i_{y_{\beta\beta}} + y_{\beta\beta}\gamma^i_{y_{\alpha\alpha}} - y_{\alpha\beta}\gamma^i_{y_{\beta\alpha}} - y_{\beta\alpha}\gamma^i_{y_{\alpha\beta}}$. The variances of impedance parameters can be computed using formula (2.11). By using the same line of reasoning, we can compute the variances of other small-signal parameters, such as *h*-, *g*-, *s*- and *ABCD*- parameters. For a detailed definition of these parameters we recommend Ref. [93].

In the following, we present a few simulation results related to the fluctuations of *h* (hybrid) and *z* (impedance) parameters of MOSFET devices. The sensitivity coefficients of the *h*-parameters and *z*-parameters are represented by contour plots in Figure 4.2 and Figure 4.3, respectively. The bias dc point and operating frequency were chosen the same as in the simulations presented in Figure 4.1. It is obvious that

the fluctuations of the doping at different locations inside the semiconductor device contribute differently to the fluctuations of small-signal parameters. In most cases, the fluctuations of the doping in the channel region and the source and drain junctions give the main contribution to the fluctuations of the *h* and *z* parameters.

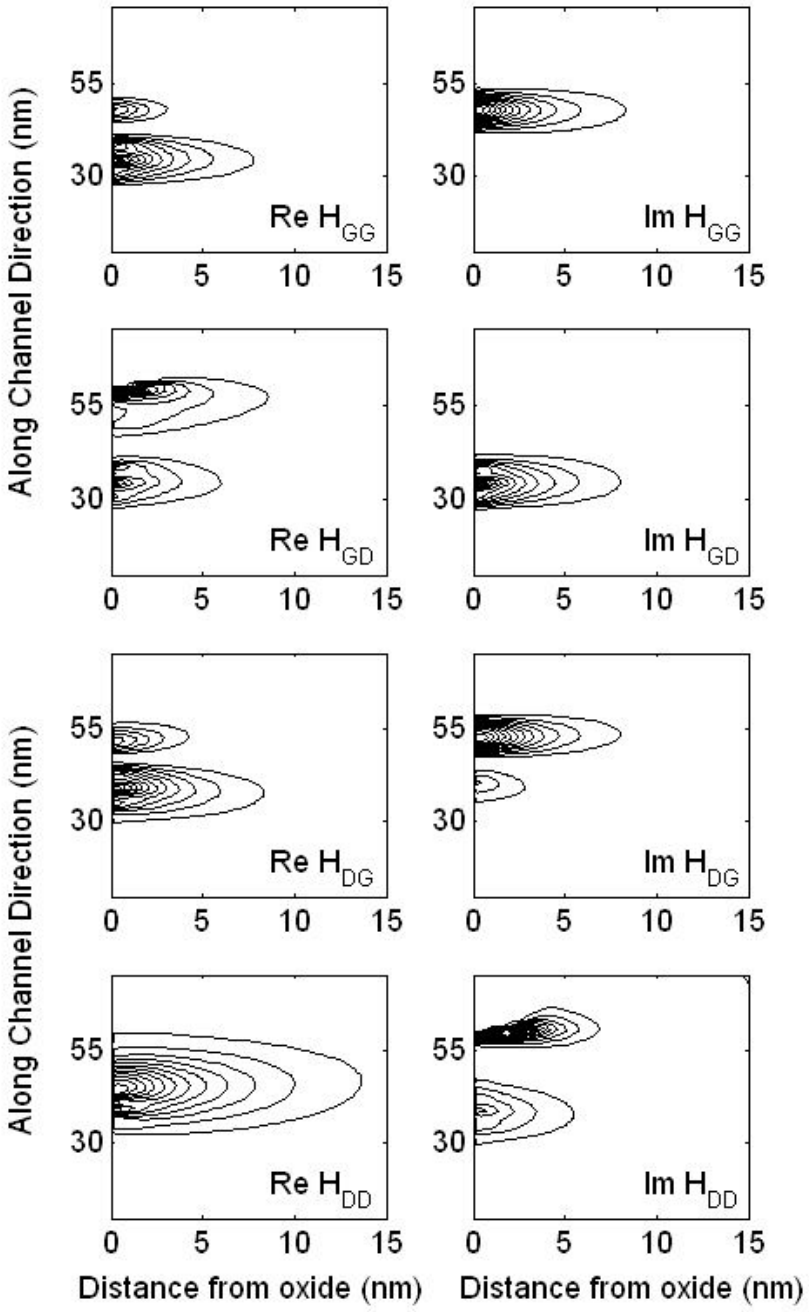

Figure 4.2: Contour plot representation of sensitivity coefficients for *h*-parameters (MOS C).

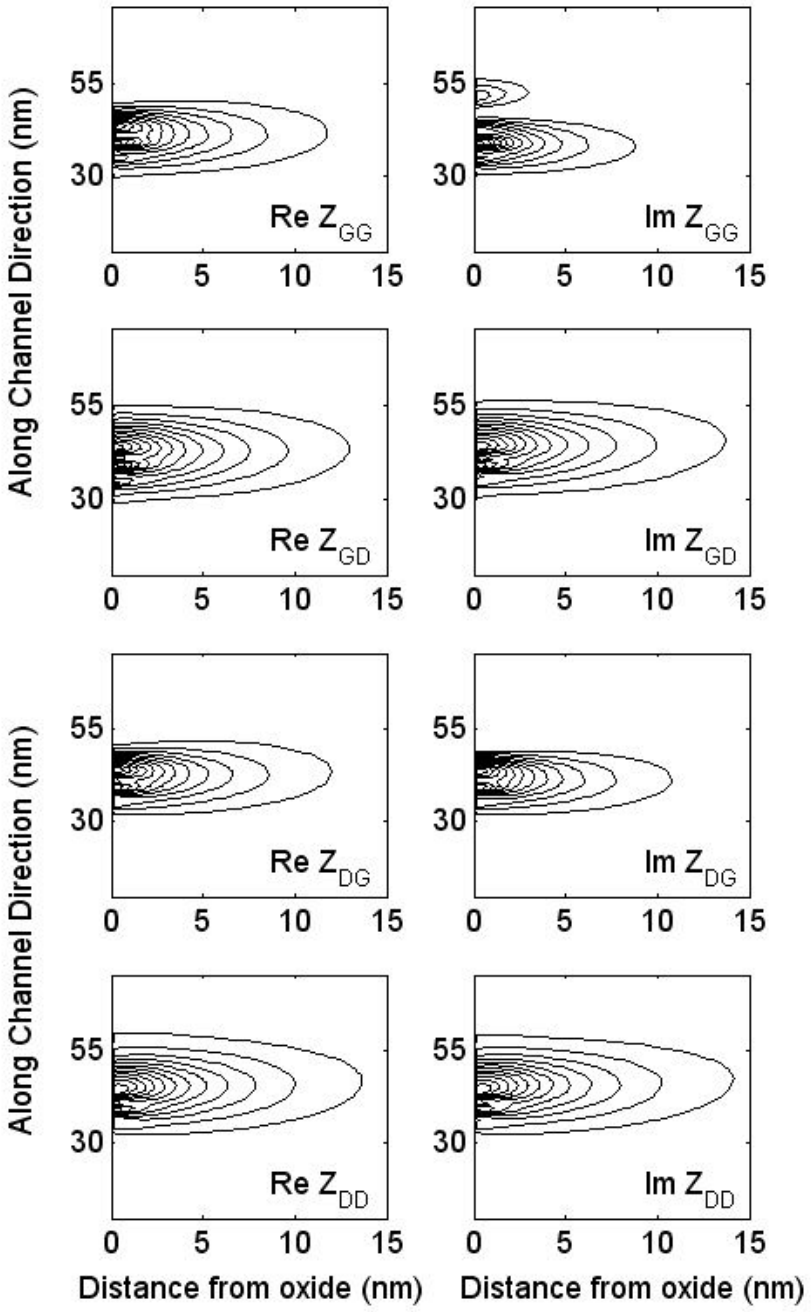

Figure 4.3: Contour plot representation of sensitivity coefficients for *z*-parameters (MOS C).

4.3 Fluctuations of gain factors

Gain factors (current and voltage gain, stability factor, unilateral gain, maximum stable, maximum available and maximum efficiency gains) can also be written as functions of admittance parameters. This section presents results related to the fluctuations of gain factors. Some of these results will be used in the next Section for the analysis of fluctuations of cut-off frequencies.

The current and voltage gain can be written as function of the admittance matrix parameters:

$$A_I = \left|\frac{y_{DG}}{y_{GG}}\right| \text{ and } A_V = \left|\frac{y_{DG}}{y_{DD}}\right|, \tag{4.20}$$

respectively. The sensitivity coefficients of A_I and A_V can be derived from formulas (3.35) and (3.36):

$$\gamma_{A_I}^{i} = \left|\frac{y_{DG}}{y_{GG}}\right| \mathrm{Re}\left(\frac{\gamma_{y_{DG}}^{i}}{y_{DG}} - \frac{\gamma_{y_{GG}}^{i}}{y_{GG}}\right) \text{ and } \gamma_{A_I}^{i} = \left|\frac{y_{DG}}{y_{GG}}\right| \mathrm{Re}\left(\frac{\gamma_{y_{DG}}^{i}}{y_{DG}} - \frac{\gamma_{y_{GG}}^{i}}{y_{GG}}\right). \tag{4.21}$$

The variances of A_I and A_V can be computed by using (2.11):

$$\sigma_{A_I}^2 = \sum_i \left(\gamma_{A_I}^{D_i}\right)^2 \frac{D_{0i}}{\Delta V_i} + \sum_{i,j} \gamma_{A_I}^{t_i} \gamma_{A_I}^{t_j} ACF(i,j), \tag{4.22}$$

and

$$\sigma_{A_V}^2 = \sum_i \left(\gamma_{A_V}^{D_i}\right)^2 \frac{D_{0i}}{\Delta V_i} + \sum_{i,j} \gamma_{A_V}^{t_i} \gamma_{A_V}^{t_j} ACF(i,j), \tag{4.23}$$

respectively.

Similarly, we can find the superposition coefficients and standard deviations of other gain factors. For completeness purposes, we list the gain factors whose random fluctuations were investigated in our research:

- Maximum unilateral gain:

$$U = \frac{\left|y_{21} - y_{12}\right|^2}{4\left(\operatorname{Re} y_{11} \operatorname{Re} y_{22} - \operatorname{Re} y_{12} \operatorname{Re} y_{21}\right)}. \tag{4.24}$$

- Maximum stable gain:

$$MSG = \left|\frac{y_{21}}{y_{12}}\right|. \tag{4.25}$$

- Stability factor:

$$k = \frac{2 \operatorname{Re} y_{11} \operatorname{Re} y_{22} - \operatorname{Re}\left(y_{12} y_{21}\right)}{\left|y_{21}\right|\left|y_{12}\right|}. \tag{4.26}$$

- Maximum available gain:

$$MAG = \left|\frac{y_{21}}{y_{12}}\right| \frac{1}{k + \sqrt{k^2 - 1}}. \tag{4.27}$$

- Maximum efficiency gain:

$$MEG = \frac{\left|y_{21}\right|^2 - \left|y_{12}\right|^2}{4\operatorname{Re}\left(y_{11} y_{22}\right) - 2\operatorname{Re}\left(y_{12} y_{21}\right) - 2\operatorname{Re}\left(y_{12} y_{12}\right)}. \tag{4.28}$$

4.4 Fluctuations of cut-off frequencies

The random doping induced fluctuations of cut-off frequencies (transit frequency f_T, unit voltage gain frequency f_0, and maximum oscillation frequency $f_{\max}$) can also be computed by using the algebra of superposition coefficients presented in Section 3.3.

Consider, for example, the fluctuations of transit frequency f_T (unit current gain frequency), which is defined as the frequency for which the current gain of a semiconductor device is equal to one. Obviously, the current gain A_I is a function of both operating frequency and doping concentration:

$$A_I = A_I\left(f, \boldsymbol{D}\right). \tag{4.29}$$

At cut-off frequency, we can write:

$$A_I\left(f_T, \boldsymbol{D}\right) = 1. \tag{4.30}$$

In the first-order approximation, equation (4.30) implies that the fluctuations of transit frequency $\tilde{f}_T$ can be expressed as a linear combination of the fluctuations of doping $\tilde{\boldsymbol{D}}$:

$$\varepsilon_{A_I}\tilde{f}_T + \sum_{i=1}^{N}\gamma_{A_I}^{i}\tilde{D}_i = 0, \tag{4.31}$$

where $\gamma_{A_I}^{i}$ are the superposition coefficients of the current amplification and ε_{A_I} is a "frequency sensitivity" coefficient. For simplicity, we focus again only on the computations of fluctuations of f_T induced by random doping fluctuations and we neglect oxide thickness fluctuations. From (4.31) we find:

$$\tilde{f}_T = -\sum_{i=1}^{N}\frac{\gamma_{A_I}^{i}}{\varepsilon_{A_I}}\tilde{D}_i, \tag{4.32}$$

which implies that $\gamma_{f_T}^{i} = -\dfrac{\gamma_{A_I}^{i}}{\varepsilon_{A_I}}$. The problem of determining the superposition coefficients of transit frequency is thus reduced to the computation of ε_{A_I}. In order to find it, we observe that ε_{A_I} can be interpreted as the variation of current amplification

A_I caused by a change in the operating frequency of $\Delta f = 1$ Hz, assuming the condition that the doping is constant (not fluctuating) over the semiconductor device. Therefore, consider the angular frequency variation $\Delta\omega$; by introducing the notation $\Delta \boldsymbol{x}_\alpha$ for the variation of the state variable due to the frequency variation $\Delta\omega$, we find from equation (4.2):

$$\left(j\omega \hat{\boldsymbol{J}}_X + \hat{\boldsymbol{F}}_X \right) \Delta \boldsymbol{x}_\alpha = -j\Delta\omega \; \hat{\boldsymbol{J}}_X \boldsymbol{x}_\alpha \,. \tag{4.33}$$

It is apparent that any variation in the operating frequency induces variations in the values of *y*-parameters. One can show from equation (4.8) that the variation in the value of $y_{\beta\alpha}$ due to $\Delta\omega$ is given (in the first-order approximation) by:

$$\Delta y_{\beta\alpha} = \frac{1}{v_G}\left[\left\langle I_X^\beta, \Delta \boldsymbol{x}_\alpha^* \right\rangle + \left\langle I_{X,\omega}^\beta, \boldsymbol{x}_\alpha^* \right\rangle \Delta\omega \right], \tag{4.34}$$

where we have introduced the notation $I_{X,\omega}^\beta = \dfrac{\partial I_X^\beta}{\partial \omega}$.

It is convenient to introduce the following coefficient:

$$\varepsilon_{y_{\beta\alpha}} = \frac{\Delta y_{\beta\alpha}}{\Delta f}, \tag{4.35}$$

which can be interpreted as the sensitivity of $y_{\beta\alpha}$ to frequency. The "frequency sensitivity" coefficient ε_{A_I} can then be written as a function of $\varepsilon_{y_{\beta\alpha}}$ by using an equation similar to (4.21):

$$\varepsilon_{A_I} = \frac{\Delta A_I}{\Delta f} = \left| \frac{y_{DG}}{y_{GG}} \right| \mathrm{Re}\left(\frac{\varepsilon_{y_{DG}}}{y_{DG}} - \frac{\varepsilon_{y_{GG}}}{y_{GG}} \right) = \mathrm{Re}\left(\frac{\varepsilon_{y_{DG}}}{y_{DG}} - \frac{\varepsilon_{y_{GG}}}{y_{GG}} \right), \tag{4.36}$$

where it was taken into account that, at transit frequency, $A_I = \left| \dfrac{y_{DG}}{y_{GG}} \right| = 1$.

Now, the algorithm of the computation of the variance of transit frequency can be summarized as follows:

(1) First, we compute the superposition coefficients of *y*-parameters with the method presented in Section 4.1 and γ_{A_I} by using formula (4.21).

(2) Then, we use equations (4.33)-(4.35) to compute the "frequency sensitivity" coefficients of *y*-parameters ($\varepsilon_{y_{\beta\alpha}}$) and equation (4.36) to determine the "frequency sensitivity" coefficient of A_I, ε_{A_I}.

(3) Finally, we compute the variance of transit frequency f_T by using equations (4.32) and (2.18).

The same approach can be applied to the computation of the variance of voltage gain cut-off frequency f_0. In this case, we should replace A_I in equations (4.29)-(4.36) with the voltage amplification $A_V = \left|\frac{y_{DG}}{y_{DD}}\right|$ and y_{GG} in equation (4.36) with y_{DD}. In the case of $f_{\max}$ (maximum oscillation frequency), which is defined as the frequency for which the unilateral gain

$$U(f_T) = \frac{\left|y_{DG} - y_{GD}\right|^2}{4\left[\mathrm{Re}(y_{GG})\mathrm{Re}(y_{DD}) - \mathrm{Im}(y_{DG})\mathrm{Im}(y_{GD})\right]}, \qquad (4.37)$$

is equal to one, equation (4.36) has a more intricate form, which can be deduced by using the algebra of superposition coefficients.

In Figures 4.4 (a) and (b) we have represented the sensitivity coefficients of transient frequency (f_T) and unit voltage gain frequency (f_0), respectively, for the

MOSFET device and bias conditions used in the previous section. One can see that the sensitivity coefficients of f_T and f_0 are similarly distributed over the semiconductor device. The small differences in the values of their magnitudes originate from the fact that f_T is slightly smaller than f_0 for the given doping concentration and dc bias voltages.

We have also investigated the dependence of the fluctuations of cut-off frequencies on the average doping concentration in the channel and oxide thickness of the device. Figure 4.5 presents the dependence of f_T, f_0, and $f_{\max}$ on the doping concentration. The roll-off of the cut-off frequencies at high values of the average doping concentration is due to the fact that the threshold voltage of the device becomes comparable to the gate voltage $V_G = 0.95$ V for large concentrations of the doping, and, consequently, the operating point of the device changes from the saturation region to the subthreshold region. For low values of the average doping concentration in the channel, the transient frequency and the maximum oscillation frequency decrease, because the voltage gain and the unilateral gain of the device decrease. It is important to note that the relative values of standard deviations of f_0 and $f_{\max}$ increase for low and high values of the average doping concentration. In practical applications, we should choose the optimum value of the doping concentration that will insure a minimum relative fluctuation of the cut-off frequencies. Figure 4.6 presents the dependence of cut-off frequencies on the oxide thickness. We can see that the standard deviations of the cut-off frequencies remain approximately constant for a large range of variation of the oxide thickness. This is

different from the case of threshold voltage [41], [73], where both the threshold voltage and the standard deviation of threshold voltage increase linearly with the thickness of the oxide layer.

It has been proposed in Section 2.5 to control the vertical doping profiles next to the silicon-oxide interface and to use an epitaxial layer of smaller doping concentration in order to suppress the fluctuations of threshold voltage [87], [88]. Hence, we tried to see to what extent the same technique can be applied to suppress the fluctuations of cut-off frequencies. In Figure 4.7 we present the dependence of the standard deviation of cut-off frequencies on the thickness of the epitaxial layer y_0 (see Figure A in the Appendix). We can see that frequency characteristics are more sensitive to doping fluctuations than threshold voltages and that it is more difficult to design doping fluctuation resistant structures for frequency characteristics.

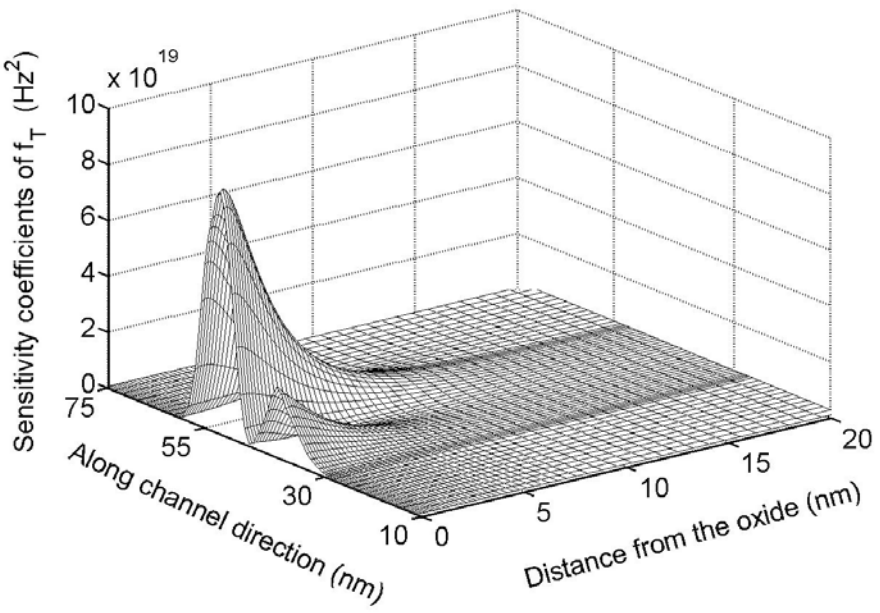

(a)

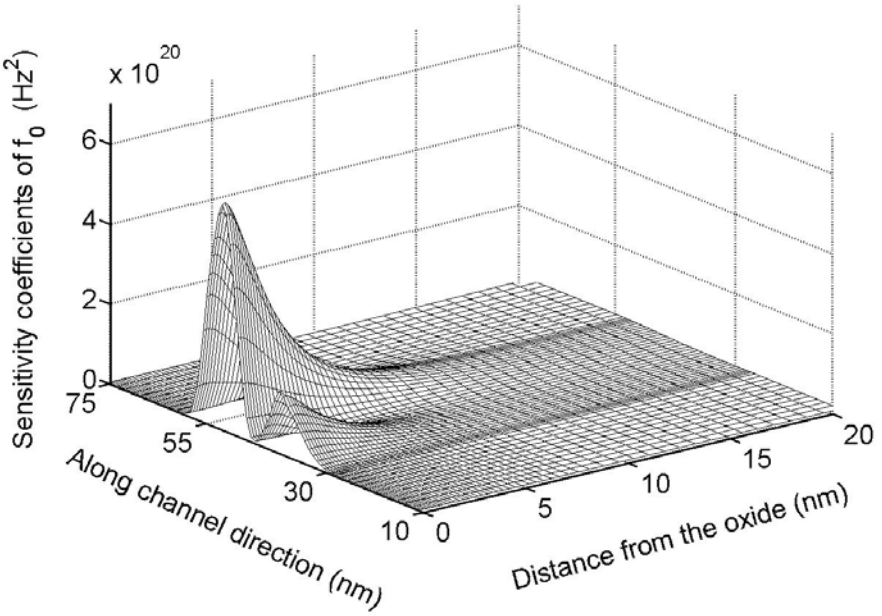

(b)

Figure 4.4: Sensitivity coefficients of transient frequency f_T (a) and unit voltage gain frequency f_0 (b) computed for MOS C.

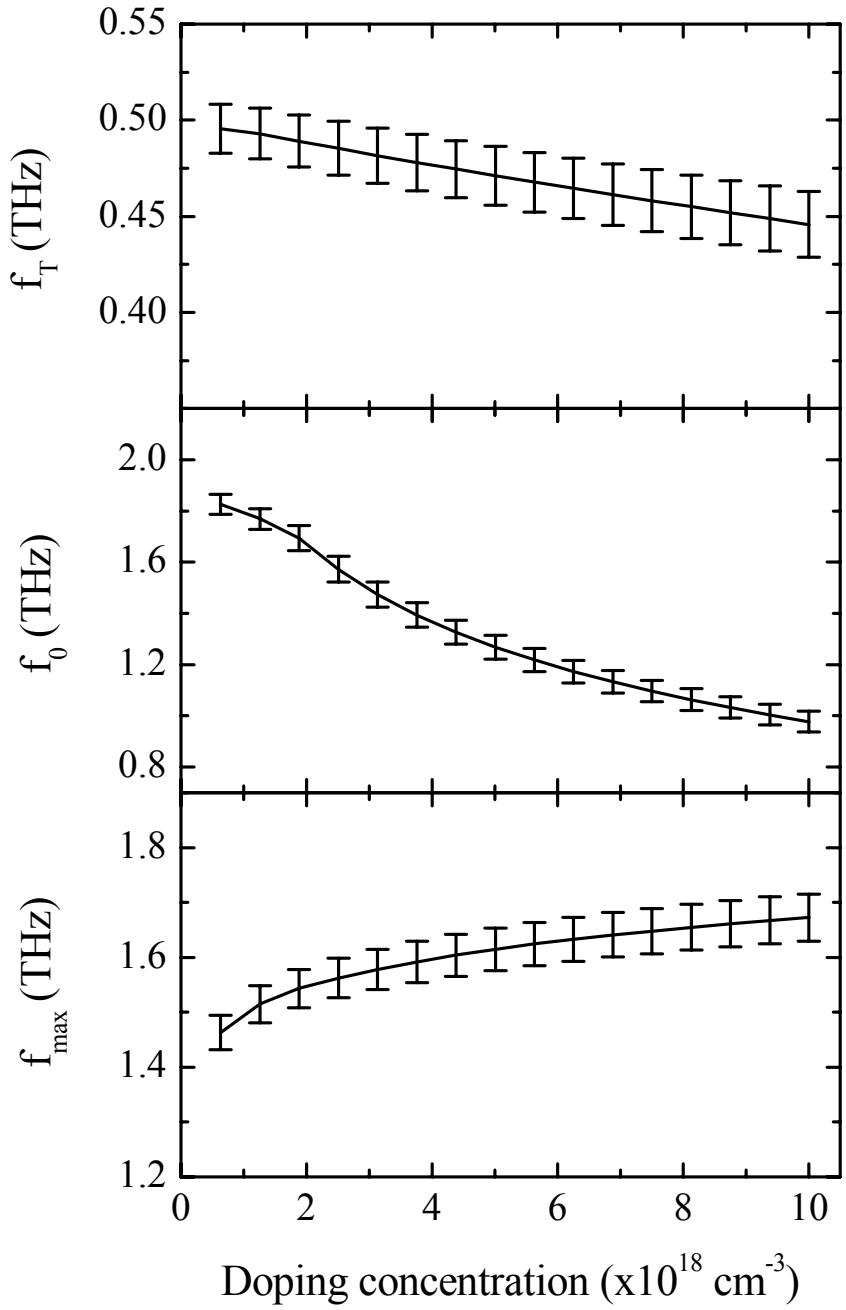

Figure 4.5: Transition frequency (f_T), unit voltage gain cut-off frequency (f_0), and maximum oscillation frequency (f_{max}) as function of average doping in the channel for MOS C. Vertical bars indicate standard deviations.

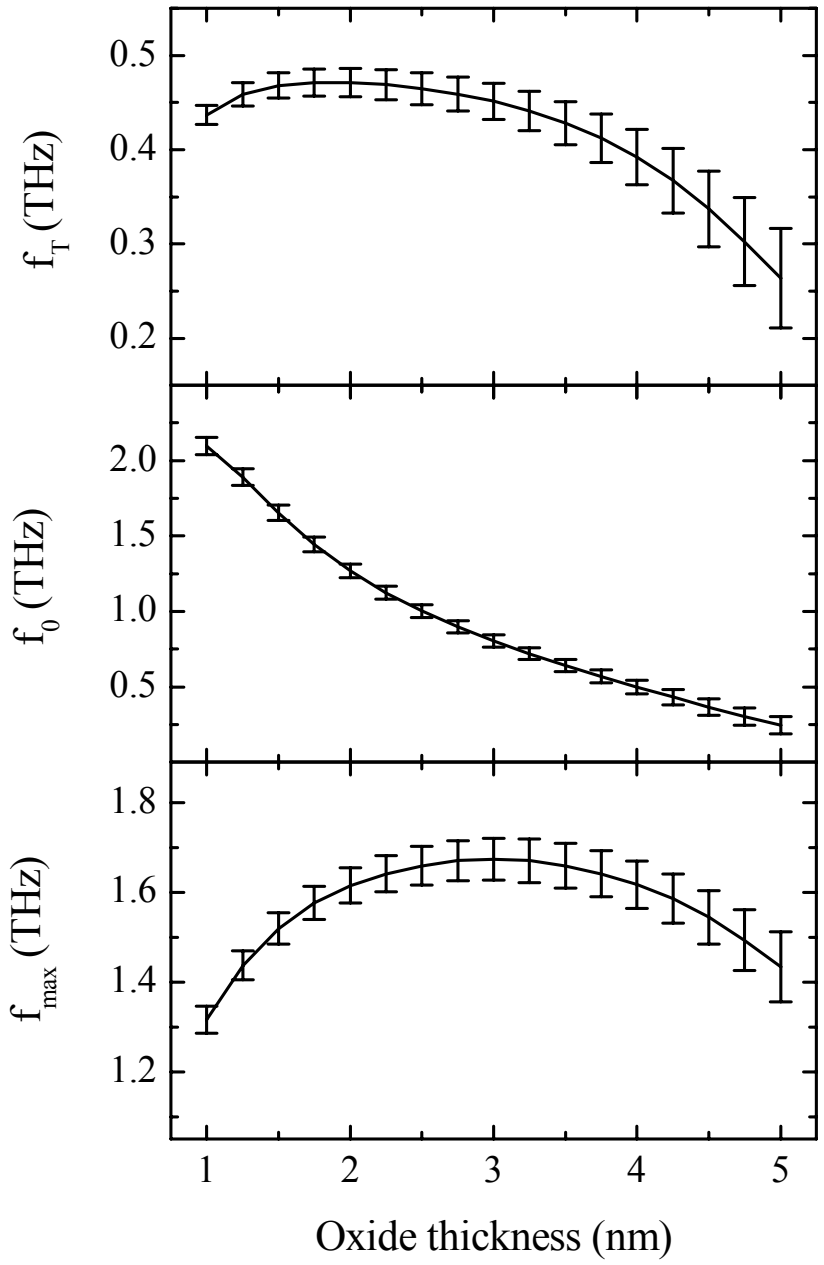

Figure 4.6: Transition frequency (f_T), unit voltage gain cut-off frequency (f_0), and maximum oscillation frequency (f_{max}) of MOS C as function of oxide thickness. Vertical bars indicate standard deviations.

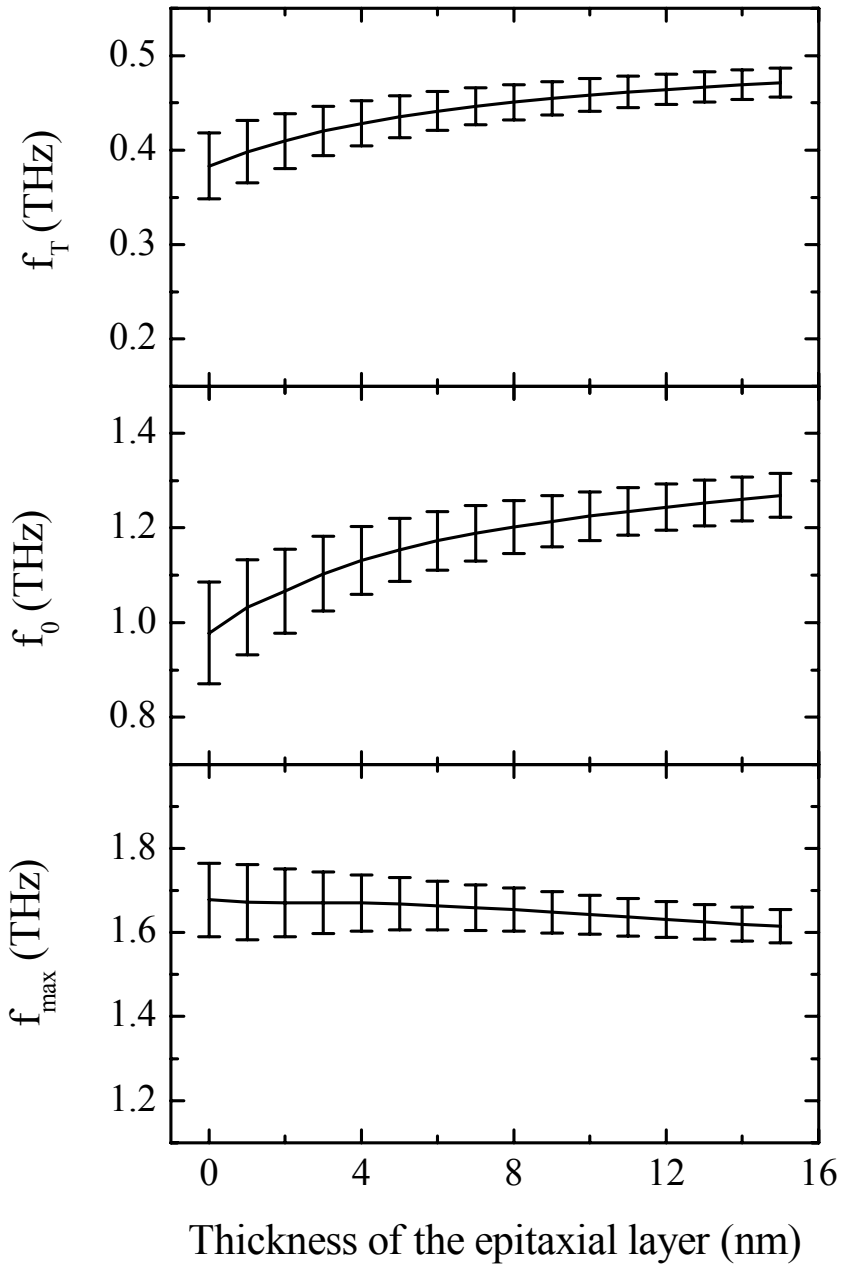

Figure 4.7: Transition frequency, unit voltage gain frequency, and maximum oscillation frequency of MOS C as function of thickness of the epitaxial layer. Vertical bars indicate standard deviations.

Chapter 5

Quantum mechanical induced effects on fluctuations in semiconductor devices

In this chapter we analyze the influence of quantum mechanical effects on the fluctuations of parameters of semiconductor devices. In the first part of the chapter, quantum mechanical effects are taken into consideration in the framework of the Density-Gradient model, while, in the second part, they are analyzed in the context of the perturbed Schrödinger-Poisson equations. We focus mostly on the analysis of fluctuations of threshold voltage of ultrasmall MOSFET devices.

5.1 Analysis of fluctuations in the framework of the Density-Gradient model

The Density-Gradient (DG) model has been extensively used in the literature for the analysis of quantum mechanical induced effects in semiconductor devices [96]-[104]. In the framework of the DG model, the classical drift-diffusion equations are modified in order to account for the quantum mechanical corrections to the electron and hole transport:

$$\boldsymbol{J}_n = -n\mu_n \nabla\varphi + D_n \nabla n - 2\mu_n n \nabla \frac{\nabla \cdot \left(b_n \nabla \sqrt{n} \right)}{\sqrt{n}}, \tag{5.1}$$

$$\boldsymbol{J}_p = -p\mu_p \nabla\varphi - D_p \nabla p + 2\mu_p p \nabla \frac{\nabla \cdot \left(b_p \nabla \sqrt{p} \right)}{\sqrt{p}}. \tag{5.2}$$

In these equations, φ is the electric potential, n, μ_n, D_n and p, μ_p, D_p are the concentration, mobility, and diffusivity of the electrons and holes, respectively. The quantum mechanical effects are "controlled" by the parameters:

$$b_n = \frac{\hbar^2}{4 r_n q m_n^*}, \tag{5.3}$$

$$b_p = \frac{\hbar^2}{4 r_p q m_p^*}, \tag{5.4}$$

where m_n^* and m_p^* denote the effective masses of the electrons and holes, while r_n and r_p are dimensionless parameters that account for the statistics of electrons and holes in semiconductor devices. The values of r_n and r_p vary asymptotically from 1, when only the lowest energy subband is occupied (e.g. at low temperature), to 3 when other subbands become populated as well (e.g. at high temperature). In order to model the carrier transport in semiconductor devices, equations (5.1)-(5.2) are coupled with the Poisson and current continuity equations. By restricting the analysis to the steady state case, the electron and hole transport in semiconductor devices can be described by the following system of nonlinear, second order partial differential equations:

$$\nabla \cdot \left(\varepsilon \nabla\varphi \right) + q\left(p - n + N_D^+ - N_A^- \right) = 0, \tag{5.5}$$

$$\frac{2\nabla\cdot\left(b_n\nabla\sqrt{n}\right)}{\sqrt{n}}+\varphi-\phi_n-\Phi_n\left(T\right)=0\,, \tag{5.6}$$

$$\frac{2\nabla\cdot\left(b_p\nabla\sqrt{p}\right)}{\sqrt{p}}-\varphi+\phi_n+\Phi_p\left(T\right)=0\,, \tag{5.7}$$

$$\nabla\cdot\left(\mu_n n\nabla\phi_n\right)=0\,, \tag{5.8}$$

$$\nabla\cdot\left(\mu_p p\nabla\phi_p\right)=0\,, \tag{5.9}$$

where ϕ_n and ϕ_p are the electron and hole quasi-Fermi potentials, respectively, while $\Phi_n\left(T\right)$ and $\Phi_p\left(T\right)$ are functions that depend on the nature of electron and hole statistics used. For example, for Boltzmann statistics $\Phi_n\left(T\right)=\frac{kT}{q}\ln\frac{n}{n_i}$ and $\Phi_p\left(T\right)=\frac{kT}{q}\ln\frac{n_i}{p}$, where T is the absolute temperature. This system of equations is subject to appropriate boundary conditions and must be solved self-consistently. More details about boundary conditions for equations (5.5)-(5.9) can be found in [102].

5.1.1 Calibration of the Density-Gradient model

Calibration (parameter identification) is one of the most important tasks in the modeling of semiconductor devices. In the case of the DG model, parameters r_n and r_p are unknown and should be regarded as empirical quantities that have to be determined by matching experimental data to microscopic calculations [102]. The same observation is valid for the electron and hole effective masses. Due to the low-order approximations involved in the derivation of equations (5.1) and (5.2), it is

unrealistic to use the experimental values of m_n^* and m_p^*. Instead, these two parameters should also be treated as fitting parameters. Since m_n^* and r_n, as well as m_p^* and r_p appear in (5.3) and (5.4) as products, the identification method can be simplified by letting only one of these two parameters vary, while keeping the other one fixed. It is usually assumed that $r_n = r_p = 3$, so the calibration problem is reduced to the determination of the electron and hole effective masses.

It should be noted that there is no unanimous agreement on the values of m_n^* and m_p^*. In most of the existing methods, m_n^* and m_p^* are found by fitting the results obtained from the DG model to the results obtained by solving the Poisson and Schrödinger equations for long channel MOS devices. For example, by fitting the DG model to the C-V curves found through simulations of 1-D MOS diodes self-consistently, Wettstein *et al*. [103] found $m_n^* = 0.278 m_0$. This value is in reasonably good agreement with the value obtained by Connelly *et al*. [104], $m_n^* = 0.258 m_0$, but it is slightly different from the value obtained by Asenov *et al*. [71] $m_n^* = 0.175 m_0$. The common feature of these identification methods is that they calibrate b_n and/or b_p against results obtained by solving the 1-D Schrödinger equation in the direction perpendicular to the oxide layer (the *z*-direction) of MOSFET devices. In this way, it is tacitly assumed that the motion of electrons and holes is quantized only in the direction perpendicular to the oxide and it is described by classical statistics in the other two directions. While this approach is appropriate for long devices, more accurate methods must be developed for situations when quantum effects are

important in the other two directions. For example, in the case of short channel MOSFET devices, the electric potential can vary significantly in the along-channel direction (the *x*-direction) and one would expect the electron motion in this direction to be quantized as well. A more rigorous approach to the problem is to solve the 2-D Schrödinger equation in the *xz* plane and to calibrate the DG model against these results. An identification method for b_n that is based on this observation is presented below. Parameter b_n is found by fitting the results obtained with the DG model to the results obtained by solving the 2-D Schrödinger equation. In subsequent computations, the (100) surface orientation is assumed for silicon because it is typical for most fabricated MOS devices.

For (100) silicon, the total electron concentration is composed of electron concentrations in six elliptical subbands that correspond to two valleys with $m_{x,i}^* = m_{y,i}^* = m_t$, $m_{z,i}^* = m_l$ (i=1,2), two valleys with $m_{x,i}^* = m_{z,i}^* = m_t$, $m_{y,i}^* = m_l$ (i=3, 4), and two valleys with $m_{y,i}^* = m_{z,i}^* = m_t$, $m_{x,i}^* = m_l$ (i=5, 6). In the above formulas, $m_{x,i}^*$, $m_{y,i}^*$, and $m_{z,i}^*$ denote the principal effective masses of the constant-energy ellipsoid in subband i, associated with the motion parallel to the *x*, *y*, and *z*-direction, respectively, and $m_t = 0.19m_0$ and $m_l = 0.916m_0$ are the transverse and longitudinal effective masses of electrons. As previously argued, the electron motion is quantized in the *x* and *z* directions and it is described by classical statistics in the *y*-direction. In the effective mass approximation, the electron energy can be described by the time-independent Schrödinger equation:

$$\left[-\frac{\hbar^2}{2}\left(\frac{1}{m^*_{x,i}}\frac{\partial^2}{\partial x^2}+\frac{1}{m^*_{z,i}}\frac{\partial^2}{\partial z^2}\right)+\varphi_c(x,z)\right]\Psi_{i,j}(x,z)=E_{i,j}\Psi_{i,j}(x,z), \qquad (5.10)$$

where $\varphi_c(x,z)$ is the confining potential in the *xz* plane measured with respect to the conduction band, while $\Psi_{j,i}(x,z)$ are the envelope wave functions associated with the j eigenvalue $E_{j,i}$ in subband i (i=1,..,6). Once the eigenvalue problem (5.10) is solved, the electron concentration can be found by summing over all energy states:

$$n(x,z)=\sum_{i=1}^{6}\sum_{j}\left|\Psi_{i,j}(x,z)\right|^2\int f_{i,j}(E)D_{i,j}(E)\,dE, \qquad (5.11)$$

where $f_{i,j}(E)$ is the Fermi distribution function and $D_{i,j}(E)=\frac{1}{h}\sqrt{\frac{2m^*_{y,i}}{E-E_{i,j}}}$ is the 1-D density of the states corresponding to electrons in subband i and energy level j. After performing the integration in (5.11), we obtain the following equation for the total electron concentration [105]:

$$n(x,z)=\sum_{i=1}^{6}\frac{2\sqrt{2m^*_{z,i}kT}}{h}\sum_{j}F_{-1/2}\left(\frac{E_F-E_{i,j}}{kT}\right)\left|\Psi_{i,j}(x,z)\right|^2, \qquad (5.12)$$

where E_F is the chemical potential which at room temperature is approximately equal to the Fermi energy and:

$$F_{-1/2}(x)=\int_0^{\infty}\frac{t^{-1/2}}{1+e^{t-x}}\,dt, \qquad (5.13)$$

is the Fermi integral of order $-1/2$.

In order to find parameter b_n, arbitrary (100) silicon systems were simulated by using the 2-D DG model and the 2-D Schrödinger equation. To avoid solving the

Poisson equation many times, we assumed that the potential in equations (5.6) and (5.10) is given a priori and we compared the electron concentration distributions obtained by using these two equations. Parameter b_n was found by using the best fit between the two electron concentration functions.

A special case in which the energy eigenstates can be found analytically is the 2-D rectangular quantum box with infinite walls. In this case,

$$\varphi(x,z)=\begin{cases}V_0, & \text{if } \ 0<x<L_x, \ \text{ and } \ 0<z<L_z,\\ \infty, & \text{otherwise,}\end{cases}, \tag{5.14}$$

$$E_{i,j_x,j_z}=\frac{h^2}{8}\left[\frac{j_x^2}{m_{x,i}^* L_x^2}+\frac{j_z^2}{m_{z,i}^* L_z^2}\right], \tag{5.15}$$

$$\Psi_{i,j_x,j_z}(x,z)=\frac{2}{\sqrt{L_x L_z}}\sin\left(\frac{j_x \pi x}{L_x}\right)\sin\left(\frac{j_z \pi z}{L_z}\right), \tag{5.16}$$

and the electron concentration $n(x,z)$ can be computed directly by using equation (5.12). In Figure 5.1 we use continuous lines to represent cross-sections through the middle plane (x = 6 nm) of the electron concentration obtained by using this approach, for different values of V_0. These values of V_0 correspond to the Fermi levels in bulk silicon with doping concentrations of 10^{16} cm^{-3}, 10^{17} cm^{-3}, and 10^{18} cm^{-3}, respectively. The quantum box is rectangular with dimensions 12×12 nm. Alternatively, $n(x,z)$ can be computed within the framework of the DG model by solving equation (5.6); cross-sections through the electron concentrations are represented in Figure 5.1 with dot lines. The best fit between the Schrödinger and the DG computations was found for $m_n^*=(0.17\pm0.01)m_0$, where m_0 is the free electron mass. The agreement between

the electron concentrations obtained by using the two approaches is remarkably good and proves that the DG model can be successfully used for the modeling of electron and hole concentration in silicon.

It is instructive to note that, in general, the x and z directions in the Schrödinger equation are not equivalent (e.g. in anisotropic systems) due to the different effective mass values in the expression of the Hamiltonian [see equation (5.10)]. These systems can be modeled in the framework of the DG model by using different values for the fitting parameters b_n and b_p along the two directions. This requires calibrating the electron and hole effective masses in both directions, which is a more complicated task. Fortunately, in the case of Si, the x, y, and z directions are equivalent because of the symmetry of the six valleys in the conduction band, and we can consider equal effective masses in these directions (denote them by m_n^*). Figure 5.2 presents the computed values of m_n^* for different dimensions L_x and L_y of the quantum region. The continuous line shows the results obtained by keeping L_y at 15 nm (which is approximately the length of the conduction channel in ultrasmall MOSFET devices) and varying L_x from 3 nm to 15 nm. The dash line shows the values of the electron effective mass in the case when L_x and L_y are equal and vary between 3 and 15 nm. We can observe that, for dimensions of the quantum box larger than 8 nm, the electron effective mass is almost constant and approximately equal to $0.17\,m_0$. For smaller dimensions of the quantum box, m_n^* should be recalibrated. For example, if one dimension of the quantum box decreases to 3 nm while the other one

is larger than 8 nm, $m_n^* \simeq 0.24\, m_0$. In numerical simulations one should use the value of the electron effective mass which corresponds to the approximate size of the quantum region.

We also computed m_n^* for other potential functions and obtained very good agreement between the predictions of the DG model and of the 2-D Schrödinger equation. In these simulations, the Schrödinger equation was discretized by using the finite difference scheme and the eigenvalues and eigenfunctions of the energy were computed by using the LAPACK package [106]. In most cases, grids of 70×70 points were used, resulting in computation times of about five hours on a Pentium 4 (2 GHz) processor. These computation times should naturally be compared with the computation times required to find the electron concentration by using the DG model and which, in our simulations, vary from a few seconds to one minute on the same processor. Figure 5.3(a) illustrates the electron concentration computed by using the Schrödinger equation with the following electric potential:

$$\varphi(x,z) = \begin{cases} V_0 + V_1 \exp\left(\dfrac{5x}{L_x}\right) - V_2 \exp\left(\dfrac{5z}{L_z}\right), & \text{if } x < L_x \text{ and } z < L_z, \\ \infty, \quad \text{otherwise,} \end{cases}, \qquad (5.17)$$

where V_0, V_1, and V_2 are given parameters. In the simulation presented in Figure 3(a) we used: V_0 = 348 mV, V_1 = 0.12 mV, and V_2 = 1.2 mV, while the dimensions of the quantum region were 4×15 nm. This potential was chosen for two reasons:

(a) it closely fits potential distributions in MOSFET channel regions;

(b) it varies significantly in the box region and, in this way, it may reveal the ability of the DG model to describe electron concentrations for a broad class of potentials.

The electron concentration computed by using the DG model is shown in Figure 5.3(b). Figure 5.4 presents cross-sections of electron concentration through the middle plane z = 7.5 nm computed by using the 2-D Schrödinger equation and the DG model, for different values of the width of the quantum region (3, 5, 10 and 15 nm). The good agreement between the Schrödinger and the DG calculations suggests once more that electron concentration can be accurately described by the DG model, provided that one performs proper calibration of the electron effective mass.

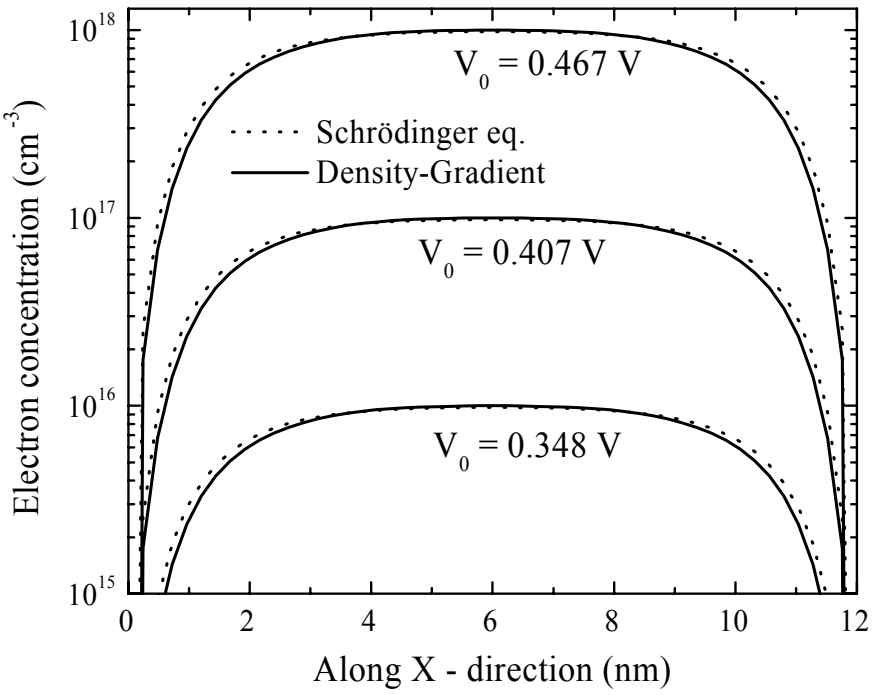

Figure 5.1: Electron concentration cross-sections through the middle plane of a 12x12 nm rectangular quantum box. The best agreement between the 2-D Schrödinger equation (continuous line) and the 2-D DG model (dash line) is obtained for $m_n^* = 0.17\, m_0$.

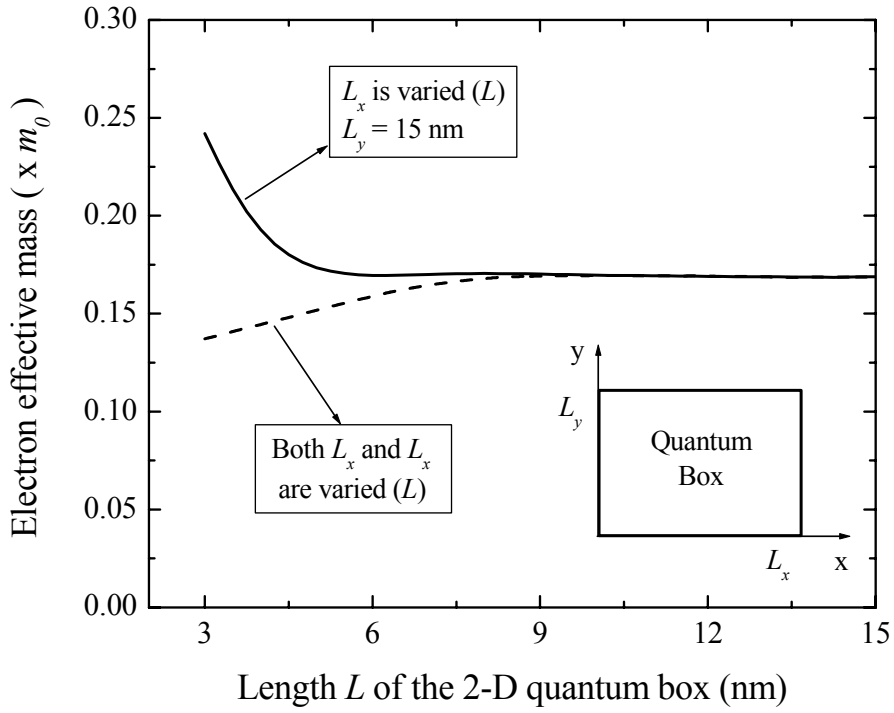

Figure 5.2: Electron effective mass that gives the best agreement between the electron concentrations computed by using the 2-D DG model and the Schrödinger equation for a rectangular quantum box. The dimensions of the box are indicated on the abscissa.

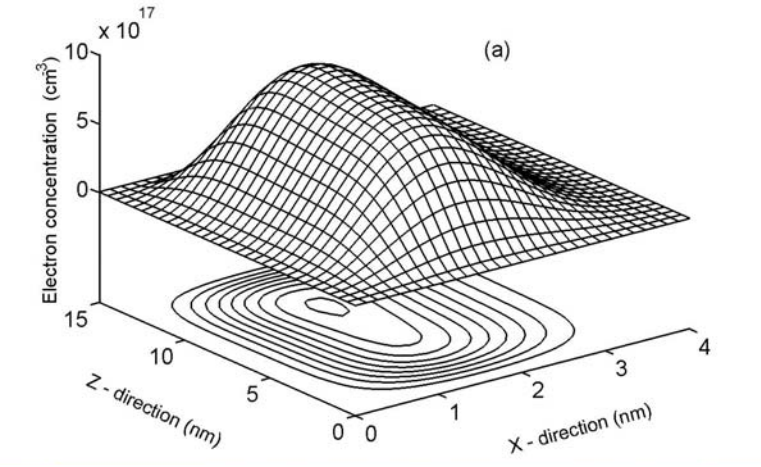

(a)

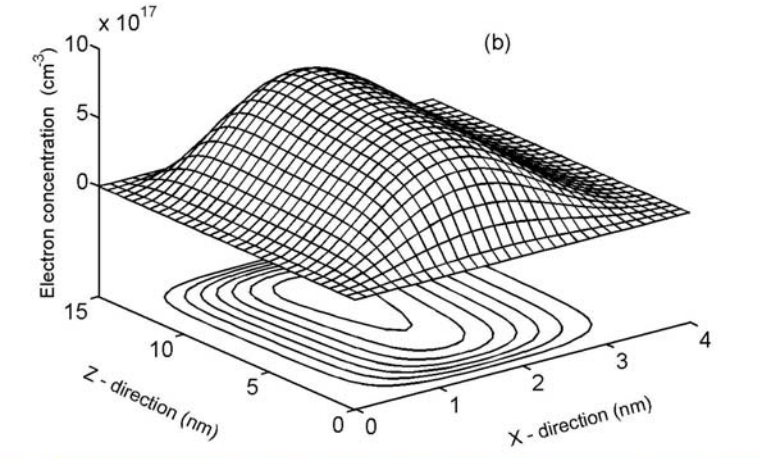

(b)

Figure 5.3: Electron concentration computed by using the 2-D Schrödinger equation (a) and the 2-D DG model (b).

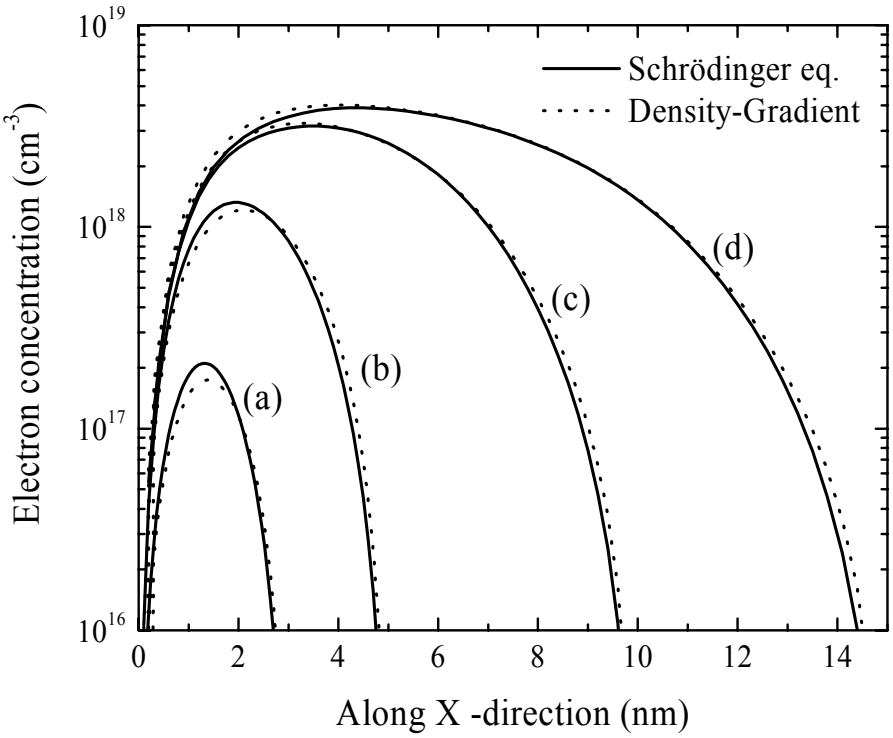

Figure 5.4: Electron concentration cross-sections through the middle plane z = 7.5 nm by using potential (5.17). The four curves correspond to different widths of the quantum region: (a) L_x = 3 nm, (b) L_x = 5 nm, (c) L_x = 10 nm, and (d) L_x = 15 nm.

5.1.2 Random doping induced fluctuations

The linearization technique presented in Chapter 2 has been implemented and used to analyze the influence of quantum effects on the fluctuations of threshold voltages in MOSFET devices. The geometrical characteristics of these devices are presented on pages 157-159. 2D and 3D DG models have been assumed throughout the simulations, with the value of effective electron mass $m_n^* = 0.21 m_0$. For *n*-channel devices, the hole current is very small, hence the total current is not very sensitive to the values of the elective hole mass. In our simulations, we assumed that $m_p^* = 0.49 m_0$ (see Ref. [103]).

The results for the standard deviation of threshold voltage obtained for the 50 nm channel length MOSFET device are presented in Figure 5.5 and compared with those obtained by Asenov *et al.* [71] for various oxide thicknesses. Both classical and quantum results are plotted in Figure 5.5 for easy comparison. The vertical bars in this figure correspond to the absolute value of the statistical errors and they show the range in which σ_{V_T} lies with a probability of 68%. There is very good agreement between our results and those obtained by using statistical method in the case of classical computations. In the case of quantum computations, our values are somewhat smaller than those reported in Ref. [71] because of the different electron masses used in simulations. The effective electron mass used in Ref. [71] $m_n^* = 0.18$ is smaller than the one used in our simulations; consequently, the values of σ_{V_T} reported therein are approximately 15% larger.

Figure 5.6 presents the standard deviation of threshold voltage as a function of the doping concentration in the channel for two MOSFET devices: MOS A and MOS B (see the Appendix for technical specifications). We can see that the variance of threshold voltage for the 30 nm channel device (MOS B) is smaller than the threshold voltage variance of the 50 nm channel device (MOS A) due to the improved doping configuration. The retrograde doping profile not only suppresses the short-channel effects, but also behaves like an epitaxial layer of smaller concentration that causes σ_{V_T} to decrease [81].

Figure 5.7 presents the sensitivity coefficients of threshold voltage of MOS C computed by using the Density-Gradient model as functions of the location in the semiconductor device. Note that, in the framework of classical computations (see Figure 2.3), threshold voltage is most sensitive to the fluctuations of the doping concentration in the region adjacent to the oxide/semiconductor interface. The quantum effects result in a slight shift (approximately 1.3 nm) of the distribution of sensitivity coefficients away from the interface. This distance is approximately equal to the distance from the interface to the peak of electron concentration in the conduction channel, which suggests that the shift of the sensitivity coefficients is due to electron confinement effects.

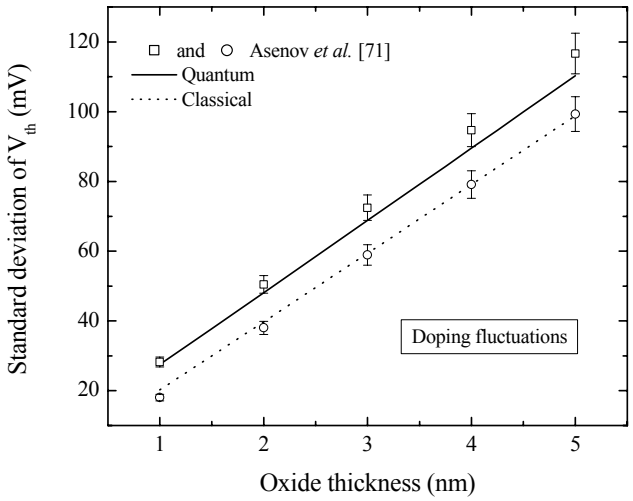

Figure 5.5: Dependence of the standard deviation of threshold voltage of MOS B on oxide thickness. In the case of quantum computations, our values are somewhat smaller than those reported in Ref. [71] because of different electron masses used in simulations.

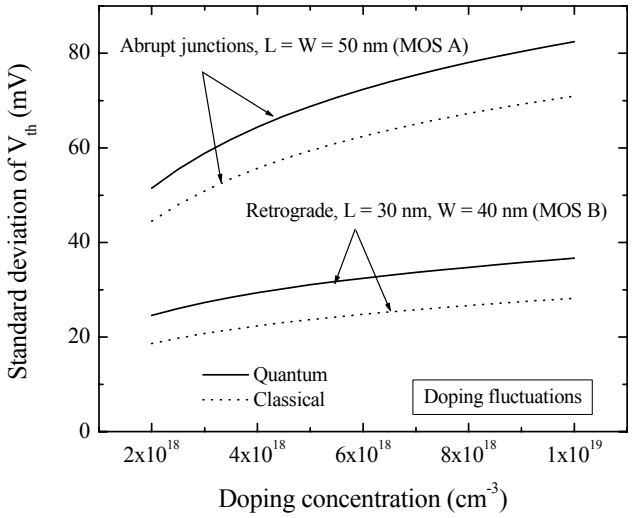

Figure 5.6: Dependence of the standard deviation of threshold voltage on the average doping concentration in the channel.

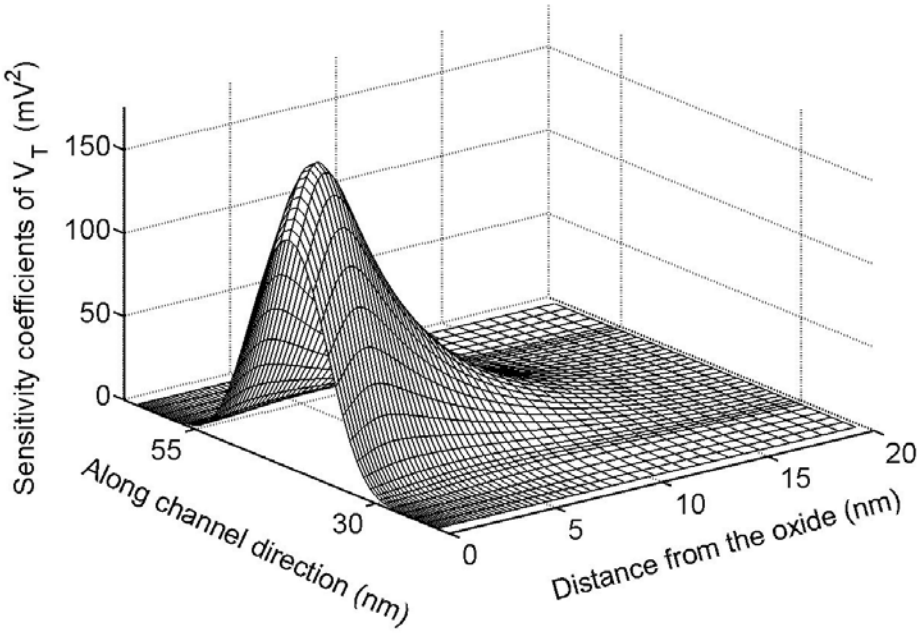

Figure 5.7: Sensitivity coefficients of threshold voltage obtained by using the Density-Gradient model for MOS C. The metallurgical channel length extends from 30 nm to 55 nm in the "along channel" direction. The corresponding classical computations are presented in Figure 2.3.

5.1.3 Random oxide roughness induced fluctuations

Following the analysis presented in Section 2.2.2, we start by presenting the standard deviation of threshold voltage as a function of the characteristic size of MOSFET devices. Two groups of devices are considered for this purpose. In the first group [Figure 5.8(a)], devices are scaled down by using the constant field scaling rule according to which the device dimensions and doping are scaled proportionally, by the same factor. In the second group [Figure 5.8(a)], devices are scaled down by using the constant voltage scaling rule according to which, if dimensions are decreased by a factor *k,* the doping concentration is increased by k^2. In both cases, σ_{V_T} is represented as a function of the metallurgical channel length of the device. One can observe that the effects of quantization are negligible for large devices, but become increasingly important for small device dimensions.

Next, we compare our results for the standard deviation of threshold voltage with those published in [32]. For a 30 nm channel length device with abrupt junctions, $N_a = 5\times10^{18}$ cm^{-3}, $t_{ox} = 1.05$ nm, $x_j = 7$ nm, and by assuming constant electron and hole mobilities and large correlation lengths of oxide thickness fluctuations, our computations give $\sigma_{V_T} = 48$ mV in the case of quantum simulations. This value is very close to the value reported in [32] $\sigma_{V_T} = (49 \pm 2.5)$ mV, which was obtained by using the Monte-Carlo technique.

We also investigated the dependence of the fluctuations of threshold voltage on the doping concentration in the channel, oxide thickness, and channel length. The

results of these simulations are presented in Figures 5.9 (a), (b), and (c), respectively. As in the case of classical computations (see Section 2.2.2), σ_{V_T} increases approximately like $\sqrt{N_a}$ and is independent of the oxide thickness.

Figure 5.10 presents the dependence of σ_{V_T} on the correlation length of oxide thickness fluctuations. These results are computed by using the exponential and the Gaussian autocorrelation functions for the oxide roughness fluctuations. We observe that the quantum mechanical effects result in a relative increase of σ_{V_T} by approximately 15% and that this increase does not depend too much on the shape of the autocorrelation function of oxide roughness.

Finally, we present the analysis of threshold voltage sensitivity to local fluctuations of the oxide thickness at different points on the semiconductor-oxide interface. Figure 5.11 presents the superposition coefficients as a function of the (*x, y*) position on the interface, computed by using the DG method. By comparing these sensitivity coefficients with those obtained by using classical computations (see Figure 2.7), we observe that the effects of quantization are to slightly confine the sensitivity coefficients to the middle of the oxide/semiconductor interface.

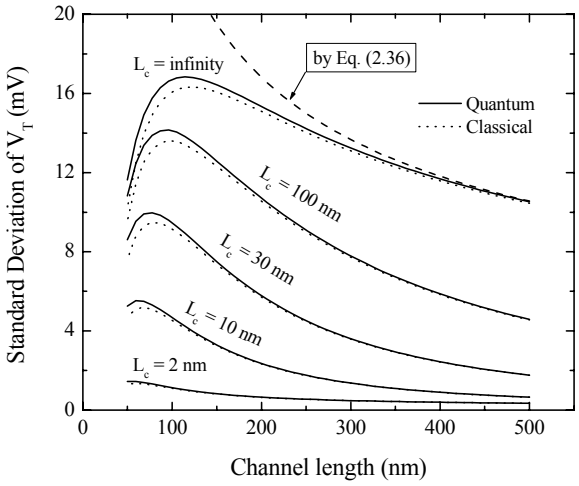

(a)

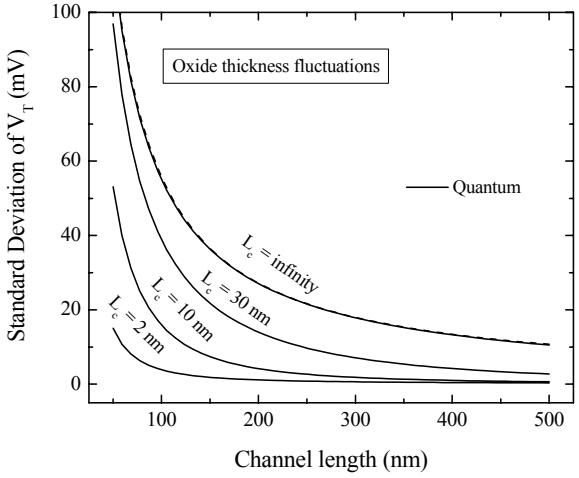

(b)

Figure 5.8: Dependence σ_{V_T} on the channel length by using constant filed (a) and constant potential (b) scaling rules. Dash lines correspond to computations given by equation (2.36).

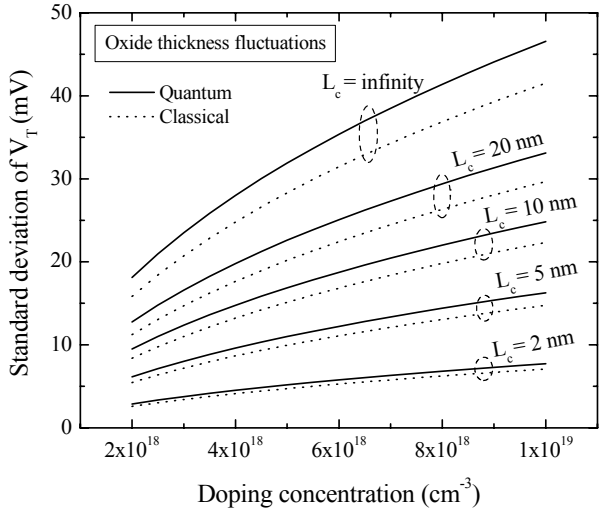
Oxide thickness fluctuations
Quantum
Classical
L_c = infinity
L_c = 20 nm
L_c = 10 nm
L_c = 5 nm
L_c = 2 nm
Standard deviation of V_T (mV)
Doping concentration (cm^{-3})
0
10
20
30
40
50
$2x10^{18}$
$4x10^{18}$
$6x10^{18}$
$8x10^{18}$
$1x10^{19}$

(a)

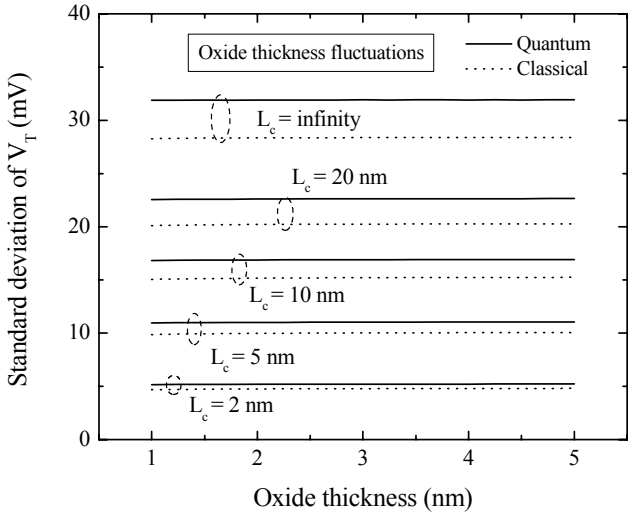
Oxide thickness fluctuations
Quantum
Classical
L_c = infinity
L_c = 20 nm
L_c = 10 nm
L_c = 5 nm
L_c = 2 nm
Standard deviation of V_T (mV)
Oxide thickness (nm)
0
10
20
30
40
1
2
3
4
5

(b)

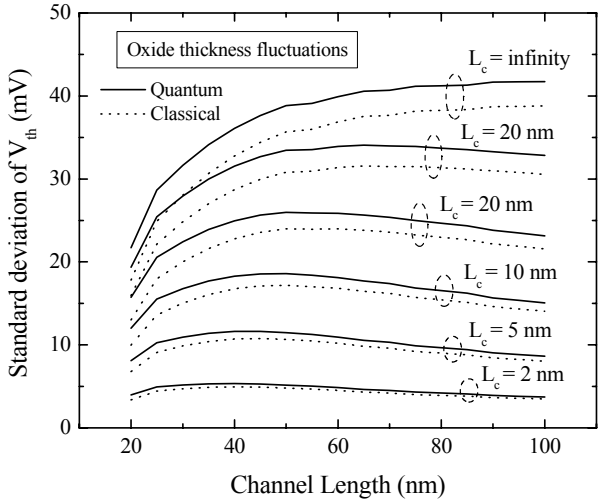

(c)

Figure 5.9: Standard deviation of threshold voltage as a function of the average doping concentration in the channel (a), oxide thickness (b), and metallurgical channel length (c). The effective channel length is larger by approximately 5 nm than the metallurgical channel length, which is indicated on the abscissa on Figure 5.9. Doping is assumed to be constant (i.e. non-fluctuating) and only oxide thickness induced fluctuations are considered (MOS B).

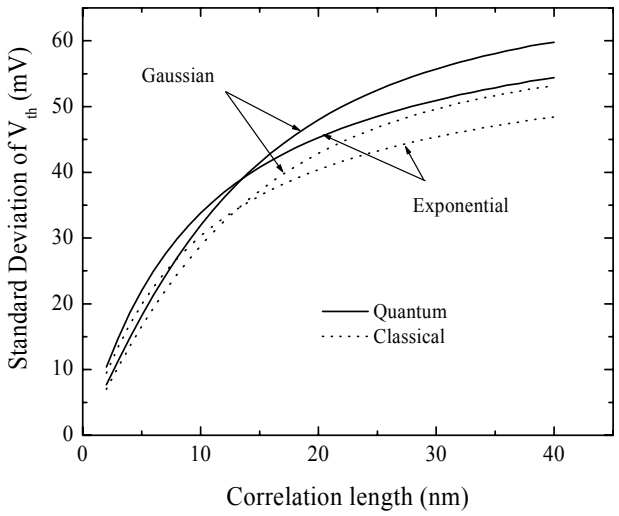

Figure 5.10: Threshold voltage standard deviation for MOS B as a function of correlation length.

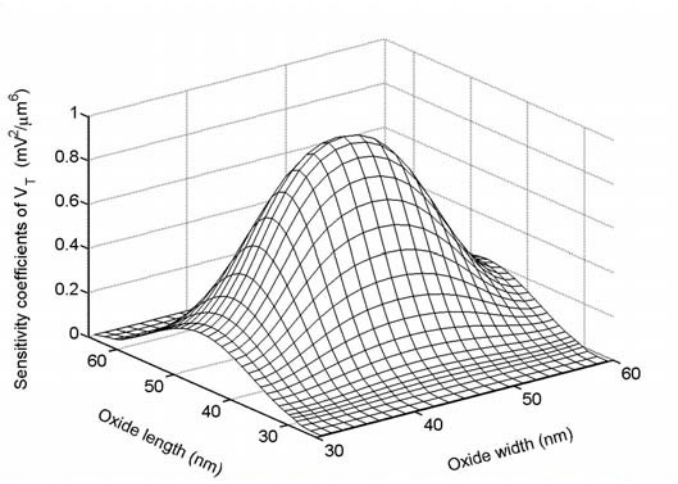

Figure 5.11: Sensitivity coefficients of threshold voltage of MOS B as a function of the position on the semiconductor-oxide interface. These computations are made by using the Density-Gradient model. The results of classical computations are presented in Figure 2.7.

5.2 Analysis of fluctuations in semiconductor devices by using the Schrödinger equation

The Density-Gradient model described in the previous section has some limitations, which make it unsuitable for the modeling of certain quantum phenomena in ultrasmall semiconductor devices. First, the DG model is an approximate model and, even though it provides useful quantitative information about the semiconductor device, it fails to produce reliable quantitative results. Second, this model needs to be recalibrated every time we change the bias conditions of the characteristics of the device. Indeed, as we can see from Figure 5.2, the values of the electron effective mass m_n^* depend on the relative dimensions of the quantum region, i.e. on the dimensions of the depletion region in the case of MOSFET devices. Since the dimensions of the quantum region are usually functions of the applied voltages, the doping concentration, and the geometric structure of the device, m_n^* changes and should be recomputed whenever the bias conditions or the structure of the device are modified.

To avoid the limitations of the DG model, more accurate techniques should be developed for the description of quantum mechanical induced fluctuations in semiconductor devices. In this section we develop a new method for the analysis of fluctuations in semiconductor devices based on exact self-consistent Poisson-Schrödinger computations. Although it is more computationally expensive, this method completely avoids the limitations of the DG model.

5.2.1 One-dimensional analysis

In this section, we present the basic idea of the linearization method for the computation of threshold voltage fluctuations in 1D MOS capacitors. The carrier concentration in *n*-type silicon inversion layers is described by the Poisson and Schrödinger equations [107]-[120]:

$$\nabla\left(\varepsilon\nabla\varphi\right) = -q\left[\, p\left(\varphi\right) - n\left(\varphi\right) + N_a \,\right], \tag{5.18}$$

$$-\frac{\hbar^2}{2}\nabla\left(\frac{1}{m_i^*}\nabla\Psi_{i,n}\right) + \left(\Delta E_c - q\varphi\right)\Psi_{i,n} = E_{i,l}\Psi_{i,n}, \tag{5.19}$$

where q is the absolute value of the electron charge, φ is the electrostatic potential, $\psi_{i,n}$ are the envelope wave functions associated with the n eigenvalue $E_{i,n}$ in subband i, m_i^* is the effective electron mass tensor, ΔE_c is the conduction band off-set, N_a is the ionized donor concentration, and n and p are the electron and hole concentrations, respectively. For the sake of simplicity, in the Poisson equation (5.18) we assume again that all donor atoms are ionized and their concentration N_a is independent of the value of electrostatic potential. The electron concentration $n\left(\varphi\right)$ is found by summing over all energy eigenstates and subbands [107]:

$$n\left(\varphi\right) = \sum_i \sum_n A_D F_{D/2-1}\left(\frac{E_F - E_{i,n}\left(\varphi\right)}{k_B T}\right)\Psi_{i,n}^2\left(\varphi\right), \tag{5.20}$$

where k_B is the Boltzmann constant, T is the temperature, D is the dimensionality of the electron gas (and in our analysis can take the values 1 or 2), and E_F is the Fermi

level. In equation (5.20), $F_{D/2-1}$ is the Fermi integral of order $D/2-1$ and coefficients A_D are given by

$$A_1 = \frac{\sqrt{2m_i^* k_B T}}{\pi\hbar} \quad \text{and} \quad A_2 = \frac{m_i^* k_B T}{\pi\hbar^2}. \tag{5.21}$$

There has been considerable effort to solve equations (5.18)-(5.20) self-consistently. The most common approach is to solve these equations by using the iterative algorithm described in Refs. [121] and [122] (S-P algorithm). However, this algorithm does not necessarily converge and different stabilization techniques have been developed to improve convergence. Another approach to solve equations (5.18)-(5.20) is by using the Newton iteration method [123]-[125]. While it is much faster than the usual S-P algorithms, this method has been implemented by using approximate Jacobian matrices, which can preclude the second order convergence rate of the Newton iteration [123]. In this work we use the exact Jacobian matrix which we calculate through first-order perturbation theory in quantum mechanics by using a method similar to the one presented in Ref. [125]. The Jacobian matrix is then used for the computation of fluctuations of threshold voltages in 1D and quasi-1D MOS systems.

5.2.1.1 Computation of the Jacobian of Poisson equation

In order to compute the Jacobian matrix of the Poisson equation, consider equation (5.18) in discretized form [82]:

$$\boldsymbol{F}\left[\boldsymbol{\varphi}, \boldsymbol{n}(\boldsymbol{\varphi})\right] = 0, \tag{5.22}$$

where $\boldsymbol{\varphi}$ and $\boldsymbol{n}$ are vectors that denote the mesh-point values of electric potential and electron concentration. The Jacobian matrix of system (5.22) is given by:

$$\hat{\boldsymbol{J}} = \frac{d\boldsymbol{F}}{d\boldsymbol{\varphi}} = \frac{\partial \boldsymbol{F}}{\partial \boldsymbol{\varphi}} + \frac{\partial \boldsymbol{F}}{\partial \boldsymbol{n}} \frac{d\boldsymbol{n}}{d\boldsymbol{\varphi}}. \tag{5.23}$$

In this equation, the partial derivatives $\frac{\partial \boldsymbol{F}}{\partial \boldsymbol{\varphi}}$ and $\frac{\partial \boldsymbol{F}}{\partial \boldsymbol{n}}$ can be easily computed because $\boldsymbol{\varphi}$ and $\boldsymbol{n}$ appear explicitly in the expression of the discretized Poisson equation (5.18). However, the computation of $\frac{d\boldsymbol{n}}{d\boldsymbol{\varphi}}$ is not so straight-forward and needs to be explained in more detail.

Consider a small perturbation $\delta\varphi$ of the electrostatic potential in the Schrödinger equation (5.19). This perturbation changes the values of the eigenvalues and eigenfunctions of the Hamiltonian, which, in turn, will induce a perturbation δn in the values of electron concentrations [see equation (5.20)]. By using the first-order perturbation theory, the shifts in the values of the energy eigenvalues and eigenfunctions can be expressed as:

$$\delta E_{i,n} = -q \left\langle \Psi_{i,n} \mid \delta\varphi \mid \Psi_{i,n} \right\rangle, \tag{5.24}$$

and

$$\delta \Psi_{i,n} = -q \sum_{l \neq n} \frac{\left\langle \Psi_{i,l} \mid \delta\varphi \mid \Psi_{i,n} \right\rangle \Psi_{i,l}}{E_{i,l} - E_{i,n}}. \tag{5.25}$$

Be linearizing equation (5.20) with respect to the fluctuating quantities and using equations (5.24) and (5.25), we obtain:

$$\delta n = \frac{q}{k_B T} \sum_i \sum_n A_D F'_{D/2-1} \left(\frac{E_F - E_{i,n}}{k_B T} \right) \left\langle \Psi_{i,l} \mid \delta\varphi \mid \Psi_{i,n} \right\rangle \Psi_{i,n}^2$$

$$-2q\sum_{i}\sum_{n}\sum_{l,l\neq n}A_D F_{D/2-1}\left(\frac{E_F-E_{i,n}}{k_BT}\right)\frac{\left\langle \Psi_{i,n}\,|\,\delta\varphi\,|\,\Psi_{i,l}\right\rangle \Psi_{i,n}\Psi_{i,l}}{E_{i,n}-E_{i,l}}, \qquad (5.26)$$

where $F'_{D/2-1}$ is the derivative of the Fermi integral. It should be noted that equations (5.24)-(5.26) were obtained by assuming that the energy levels are nondegenerate and does not take into account accidental degeneracies that are possible in 2D bound systems. In the case of 1D bound systems, the energy levels are always nondegenerate and these equations can be used safely for the calculation of δn. If we express the scalar products in (5.26) in integral form, we obtain:

$$\delta n(\boldsymbol{r})=\int_{QR} d\boldsymbol{r}'\delta\varphi(\boldsymbol{r}')\sum_{\substack{i,n,l\\ l\neq n}}A_D\Psi_{i,n}(\boldsymbol{r}')\Psi_{i,l}(\boldsymbol{r}')\left[\frac{q}{k_BT}F'_{D/2-1}\left(\frac{E_F-E_{i,n}}{k_BT}\right)\Psi^2_{i,n}(\boldsymbol{r})\delta_{n,l}\right.$$

$$\left.+2qF_{D/2-1}\left(\frac{E_F-E_{i,n}}{k_BT}\right)\frac{\Psi_{i,n}(\boldsymbol{r})\Psi_{i,l}(\boldsymbol{r})}{E_{i,n}-E_{i,l}}\right], \qquad (5.27)$$

where $\delta_{n,l}=0$ if $n\neq l$ and $\delta_{n,n}=1$. The integral in equation (5.27) is taken over the quantum region QR, which is a line for quantum-well problems (1D) and a surface for quantum-wires (2D). The discretization of the kernel in integral (5.27) is the Fréchet derivative of $\boldsymbol{n}$ with respect to $\boldsymbol{\varphi}$. Hence, the elements of matrix $\frac{d\boldsymbol{n}}{d\boldsymbol{\varphi}}$ can be written as follows:

$$\left(\frac{d\boldsymbol{n}}{d\boldsymbol{\varphi}}\right)_{\alpha,\beta}=\sum_{i}\sum_{n}\sum_{l,l\neq n}A_D\Psi^{\beta}_{i,n}\Psi^{\beta}_{i,l}\left[\frac{q}{k_BT}F'_{D/2-1}\left(\frac{E_F-E_{i,n}}{k_BT}\right)\left(\Psi^{\alpha}_{i,n}\right)^2\delta_{n,l}\right.$$

$$\left.+2qF_{D/2-1}\left(\frac{E_F-E_{i,n}}{k_BT}\right)\frac{\Psi^{\alpha}_{i,n}\Psi^{\alpha}_{i,l}}{E_{i,n}-E_{i,l}}\right], \qquad (5.28)$$

where Ψ^{α} and Ψ^{β} denote the values of the wave functions at mesh-points α and β.

In the numerical implementation of matrix $\frac{d\boldsymbol{n}}{d\boldsymbol{\varphi}}$, it should be considered that the summation over indices n and l in (5.28) is usually taken over the first several energy eigenvalues, which decreases the total computational cost significantly. The most computationally expensive part is the evaluation of $F'_{D/2-1}$ and $F_{D/2-1}$. In our simulations, we have computed the derivatives of the Fermi integrals by using the formulas:

$$\frac{dF_{-1/2}(x)}{dx} = -\frac{1}{2}F_{-3/2}(x), \tag{5.29}$$

$$\frac{dF_{0}(x)}{dx} = \frac{1}{1+\exp(-x)}, \tag{5.30}$$

while the Fermi integrals were computed by using the approximate polynomial formulas presented in [126]-[129].

5.2.1.2 Analysis of fluctuations of threshold voltage

Let us now focus on computing the threshold voltage fluctuations induced by random doping and random oxide thickness variations in 1D MOS systems (e.g. MOS capacitor). In the framework of 1D classical computations, threshold voltage is usually defined as the potential on the gate at which the electron concentration at the surface is equal to the hole concentration before inversion. In the framework of quantum computations we adopt the "total inversion charge definition," according to which threshold voltage is defined as the gate voltage at which the net inversion sheet charge Q^{inv} is equal to the value obtained from classical computations.

The basic idea of the method for the computation of fluctuations in semiconductor devices is linearization of the state and transport equations with respect to the fluctuating quantities. For the purpose of our analysis it is convenient to re-write discretized equation (5.22) as:

$$\boldsymbol{F}\left[\boldsymbol{\varphi}, \boldsymbol{n}(\boldsymbol{\varphi}), V_G, \boldsymbol{D}, t\right] = 0, \tag{5.31}$$

where V_G is the gate voltage, $\boldsymbol{D}$ is a vector whose components are the mesh point values of the doping concentration, and t is the oxide thickness. Note that V_G and t enter linearly in the boundary conditions at the semiconductor/oxide interface, which simplifies the analytical form of equation (5.31) considerably. By linearizing (5.31) around the average values of $\boldsymbol{\varphi}$, $\boldsymbol{n}$, V_G, $\boldsymbol{D}$, and t, we obtain:

$$\hat{\boldsymbol{J}}\tilde{\boldsymbol{\varphi}} + \hat{\boldsymbol{F}}_{\boldsymbol{D}}\tilde{\boldsymbol{D}} + \boldsymbol{F}_{V_G}\tilde{V}_G + \boldsymbol{F}_t\tilde{t} = 0, \tag{5.32}$$

where $\hat{\boldsymbol{J}}$ is defined in equation (5.23), $\hat{\boldsymbol{F}}_{\boldsymbol{D}}$, $\boldsymbol{F}_{V_G}$, and $\boldsymbol{F}_t$ are the derivatives of $\boldsymbol{F}$ with respect to $\boldsymbol{D}$, t, and V_G, respectively, and "~" denotes the fluctuating parts of the given parameters. The net inversion charge can be written as the sum of the discretization volumes multiplied by the electron concentration at each mesh point. If we denote this sum by a linear operator $Q^{inv}(\boldsymbol{n})$ on $\boldsymbol{n}$ and we take into consideration that the net inversion charge is constant at threshold voltage, we can write:

$$0 = Q^{inv}_{\boldsymbol{n}}\tilde{\boldsymbol{n}} = Q^{inv}_{\boldsymbol{n}}\frac{d\boldsymbol{n}}{d\boldsymbol{\varphi}}\tilde{\boldsymbol{\varphi}}, \tag{5.33}$$

where $Q^{inv}_{\boldsymbol{n}}$ is a row vector whose elements are the derivatives of Q^{inv} with respect to $\boldsymbol{n}$, i.e. the volumes of the mesh cells at each discretization point. Equations (5.32) and

(5.33) represent a system of coupled equations with unknowns $\tilde{\varphi}$ and $\tilde{V}_T = \tilde{V}_G$. In order to decouple them, we multiply equation (5.32) from the left by $Q_{\boldsymbol{n}}^{inv} \dfrac{d\boldsymbol{n}}{d\boldsymbol{\varphi}} \hat{\boldsymbol{J}}^{-1}$ and then use equation (5.33) to prove that:

$$Q_{\boldsymbol{n}}^{inv} \frac{d\boldsymbol{n}}{d\boldsymbol{\varphi}} \hat{\boldsymbol{J}}^{-1} \hat{\boldsymbol{F}}_{\boldsymbol{D}} \tilde{\boldsymbol{D}} + Q_{\boldsymbol{n}}^{inv} \frac{d\boldsymbol{n}}{d\boldsymbol{\varphi}} \hat{\boldsymbol{J}}^{-1} \boldsymbol{F}_{V_G} \tilde{V}_G + Q_{\boldsymbol{n}}^{inv} \frac{d\boldsymbol{n}}{d\boldsymbol{\varphi}} \hat{\boldsymbol{J}}^{-1} \boldsymbol{F}_t \tilde{t} = 0 . \tag{5.34}$$

By introducing the notation

$$\boldsymbol{g} = Q_{\boldsymbol{n}}^{inv} \frac{d\boldsymbol{n}}{d\boldsymbol{\varphi}} \hat{\boldsymbol{J}}^{-1} , \tag{5.35}$$

we arrive at the following formula for the fluctuations of threshold voltage:

$$\tilde{V}_T = -\frac{\boldsymbol{g}^t \cdot \hat{\boldsymbol{F}}_{\boldsymbol{D}}}{\boldsymbol{g}^t \cdot \boldsymbol{F}_{V_G}} \cdot \tilde{\boldsymbol{D}} - \frac{\boldsymbol{g}^t \cdot \boldsymbol{F}_t}{\boldsymbol{g}^t \cdot \boldsymbol{F}_{V_G}} \tilde{t} . \tag{5.36}$$

In this equation, $\boldsymbol{g}^t$ is the transpose of column vector $\boldsymbol{g}$, which can be found by solving the following linear system of equations:

$$\hat{\boldsymbol{J}}^t \boldsymbol{g} = \left(Q_{\boldsymbol{n}}^{inv} \frac{d\boldsymbol{n}}{d\boldsymbol{\varphi}} \right)^t , \tag{5.37}$$

where superscript "*t*" denotes the transpose of the given matrix or vector.

The superposition coefficients of threshold voltage can be identified from equation (5.34):

$$\gamma_{V_T}^{D_i} = -\frac{\left(\boldsymbol{g}^t \cdot \hat{\boldsymbol{F}}_{\boldsymbol{D}} \right)_i}{\boldsymbol{g}^t \cdot \boldsymbol{F}_{V_G}} , \tag{5.38}$$

and

$$\gamma_{V_T}^{t} = -\frac{\boldsymbol{g}^t \cdot \boldsymbol{F}_t}{\boldsymbol{g}^t \cdot \boldsymbol{F}_{V_G}} . \tag{5.39}$$

These coefficients can be used to compute the standard deviation of threshold voltage due to random doping fluctuations in MOS structures. If we assume again that the fluctuations of the doping concentration at different locations are independent Poisson variables and if we take into account that for Poisson random variables variance is equal to the expected value, we can use equation (2.7) and write:

$$\sigma_{V_T}^2 = \sum_i \left(\gamma_{V_T}^{D_i}\right)^2 \frac{D_{0i}}{\Delta V_i} + \left(\gamma_{V_T}^{t}\right)^2 \sigma_{ox}^2, \tag{5.40}$$

where D_{0i} are the average values of the doping at locations i, ΔV_i are the volumes of the discretization mesh-cells, and σ_{ox}^2 is the variance of oxide thickness fluctuations. In the derivation of formula (5.40), it has been assumed that oxide thickness varies evenly at all points on the oxide/semiconductor interface. Hence, this formula can be used to compute the standard deviation of threshold voltage in the case where the correlation length of oxide thickness fluctuations is much larger than the length of the conduction channel.

Next, the algorithm for the computation of the standard deviation of threshold voltage for 1D MOS systems can be summarized as follows:

1) Solve the coupled Poisson and "effective mass" Schrödinger equations for the average values of the doping and oxide thickness, by using the exact Jacobian matrix defined by formulas (5.23) and (5.28) and the Newton iteration technique;
2) Solve the linear system of equations (5.37) to find vector $\boldsymbol{g}$;

3) Find the superposition coefficients of threshold voltage by using formulas (5.38) for random doping fluctuations and (5.39) for random oxide thickness fluctuations;
4) Compute the standard deviation of threshold voltage by using formula (5.40).

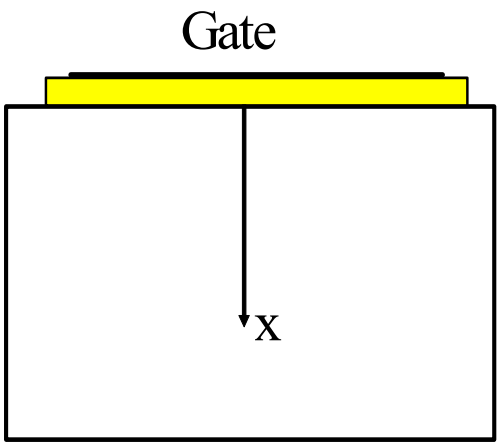

Figure 5.12: 1D MOSFET device. The Schrödinger and Poisson equations were discretized in $N = 200$ points by using the finite discretization skim and the threshold voltage was computed by using the "total inversion charge definition."

5.2.1.3 Computational results

The techniques presented in the previous section were numerically implemented and used for the computation of fluctuations of threshold voltages in MOS capacitors. In all simulations, the eigenvalues and eigenfunctions of the Schrödinger equation were computed by using the LAPACK package [106]. In the case of 1D MOS capacitors, the Schrödinger and Poisson equations have been

discretized by using N = 200 mesh points and standard finite difference schemes and the threshold voltages were computed by using the "total inversion charge definition".

First, we compare the results obtained by using the linearization technique with the results computed by using the Monte-Carlo method. Two MOS capacitors were considered for this purpose. The first one has a simplified architecture with constant average doping concentration N_a = 10^{18} cm^{-3} and oxide thickness of t = 4 nm. The second device has a slightly optimized structure with retrograde doping profile: the channel doping concentration decreases from 10^{18} cm^{-3} at 20 nm (and deeper) to 10^{16} cm^{-3} at the surface, according to a truncated Gaussian distribution function. The average oxide thickness of this device is 5 nm. Since the variance $\sigma^2_{V_T}[DF]$ of the threshold voltage induced by the random doping fluctuations decreases linearly with respect to the area of the semiconductor/oxide interface $L \times W$, where L and W are the length and the width of the MOS capacitor [see formula (5.40)], the values of the $\sigma_{V_T}[DF]$ presented in this section are multiplied by $\sqrt{LW}$. Also, since the variance $\sigma^2_{V_T}[OTF]$ of the threshold voltage induced by random oxide thickness fluctuations increases linearly with respect to the variance of oxide thickness, the values of $\sigma_{V_T}[OTF]$ are divided by σ_{ox}.

Table 1 presents the standard deviations of threshold voltages obtained by using the Monte-Carlo method and our linearization technique for the first MOS capacitor. Statistics for 100, 200, 500, and 1000 of different doping and oxide realizations are accumulated in order to compute σ_{V_T} by using the Monte-Carlo method. It is remarkable that the linearization method predicts fairly accurately the

standard deviation of the threshold voltage induced by random oxide thickness fluctuations and it gives a very good estimate of the standard deviation of the threshold voltage induced by random doping fluctuations. This can be explained by the fact that V_T depends linearly on the oxide thickness and it displays slightly nonlinear behaviour with respect to the doping concentration in the channel. For this reason, the linearization technique gives somewhat more precise results in the case of oxide thickness fluctuations than in the case of random doping fluctuations.

Table 2 presents the standard deviations of threshold voltages for the second device (retrograde doping). Even though this device has a larger oxide thickness and one expects the standard deviation of the threshold voltage induced by random doping fluctuations to be larger than for the first device, the fluctuations of threshold voltage are smaller because of the improved doping configuration. The results presented in these tables show that the linearization technique can be successfully used to compute the fluctuations of threshold voltages in 1D MOS devices.

We have also investigated the dependence of the fluctuations of threshold voltage on the doping concentration and oxide thickness for the MOS capacitor with constant average doping concentration in the channel. Figures 5.3 (a) and (b) present the computed standard deviations of threshold voltage for the case of random doping fluctuations, while Figures 5.14 (a) and (b) present σ_T in the case of random oxide thickness fluctuations. The results presented in these figures are obtained by using the linearization technique described in the previous section. It is interesting to observe that the standard deviation of threshold voltage can be estimated analytically in the

framework of classical calculations, by using the charge-sheet and depletion approximations.

A. For random doping induced fluctuations it can be shown that [81]:

$$\sigma_{V_T}\left[DF\right]=\frac{qt_{ox}}{\varepsilon_{ox}}\sqrt{\frac{N_aW_d}{3LW}}, \tag{5.41}$$

where $W_d=\sqrt{\frac{4\varepsilon_{Si}\phi_B}{qN_a}}$ is the width of the depletion region.

B. For the analysis of random oxide thickness fluctuations, it is convenient to consider the equation of the threshold voltage for long channel devices:

$$V_T=V_{fb}+2\phi_B+\frac{\sqrt{4\varepsilon_{Si}qN_a\phi_B}}{\varepsilon_{ox}}t_{ox}, \tag{5.42}$$

where $2\phi_B=\frac{2kT}{q}\ln\frac{N_a}{n_i}$ is the band bending potential and all other symbols have their usual meaning. Assuming that t_{ox} in (5.42) is a random variable with standard deviation σ_{ox}, the standard deviation of threshold voltage can be computed by using:

$$\sigma_{V_T}\left[OTF\right]=\frac{\sqrt{4\varepsilon_{Si}qN_a\phi_B}}{\varepsilon_{ox}}\sigma_{ox}. \tag{5.43}$$

The values of the σ_{V_T} obtained by using equations (5.41) and (5.43) are represented in Figures 5.13 (a) and (b) and Figures 5.14 (a) and (b) with square symbols. A very good agreement between analytical predictions and classical simulations is observed, which again suggests that the linearization approach gives reliable results. It is important to observe that $\sigma_{V_T}\left[OTF\right]$ is independent of oxide thickness; our

computations show that both quantum and classical results can be approximated by a power low $\sigma_{V_T}\left[OTF\right] \sim N_a^{0.5}$ [in (5.43), the effect of ϕ_B on N_a can be neglected since it enters through a logarithmic term].

	Doping fluctuations		Oxide thickness fluctuations	
N	$\sigma_{V_T} \times \sqrt{LW}$ (mV×μm) Classical	$\sigma_{V_T} \times \sqrt{LW}$ (mV×μm) Quantum	$\sigma_{V_T} / \sigma_{ox}$ (mV/nm) Classical	$\sigma_{V_T} / \sigma_{ox}$ (mV/nm) Quantum
100	2.01	2.23	108	119
200	1.98	2.21	106	110
500	1.90	2.16	105	115
1000	1.92	2.14	106	114
Linearization technique	1.95	2.37	105	111

Table 5.1: Standard deviations of threshold voltage for a MOS capacitor with constant average doping by using the Monte-Carlo and the linearization techniques (N_a = 10^{18} cm^{-3} and t = 4 nm).

	Doping fluctuations		Oxide thickness fluctuations	
N	$\sigma_{V_T} \times \sqrt{LW}$ (mV×μm) Classical	$\sigma_{V_T} \times \sqrt{LW}$ (mV×μm) Quantum	$\sigma_{V_T} / \sigma_{ox}$ (mV/nm) Classical	$\sigma_{V_T} / \sigma_{ox}$ (mV/nm) Quantum
100	1.39	1.59	168	171
200	1.43	1.64	166	168
500	1.42	1.62	164	161
1000	1.39	1.60	161	165
Linearization technique	1.41	1.75	159	166

Table 5.2: Standard deviations of threshold voltage for a MOS capacitor with retrograde doping profile by using the Monte-Carlo and the linearization techniques (N_a = 10^{18} cm^{-3} at y = 20 nm from the oxide, N_a = 10^{16} cm^{-3} at the interface, and t = 5 nm).

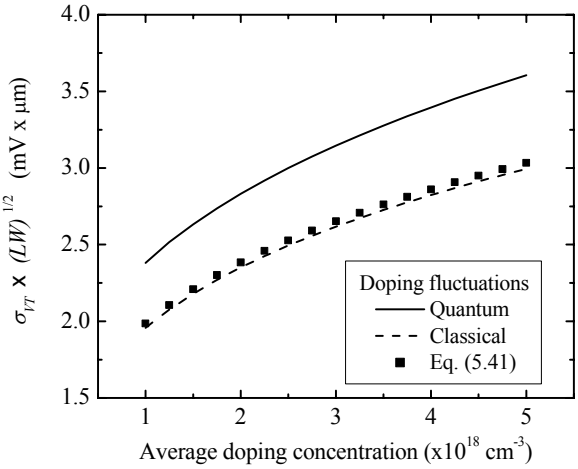

(a)

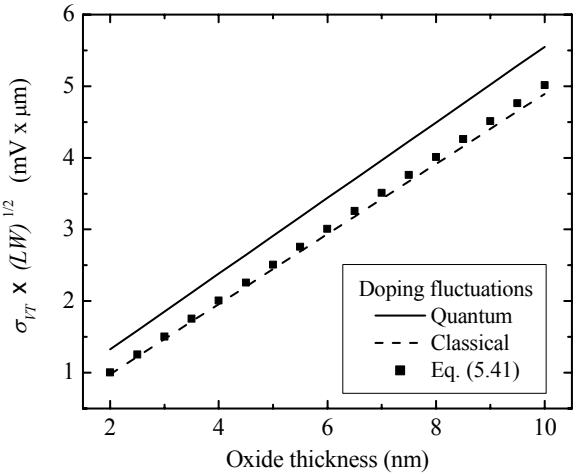

(b)

Figure 5.13: Standard deviation of threshold voltage as a function of average doping concentration (a) and oxide thickness (b) for a MOS capacitor (N_a = 10^{18} cm^{-3} and t = 4 nm). Only random doping induced fluctuations are considered in these simulations.

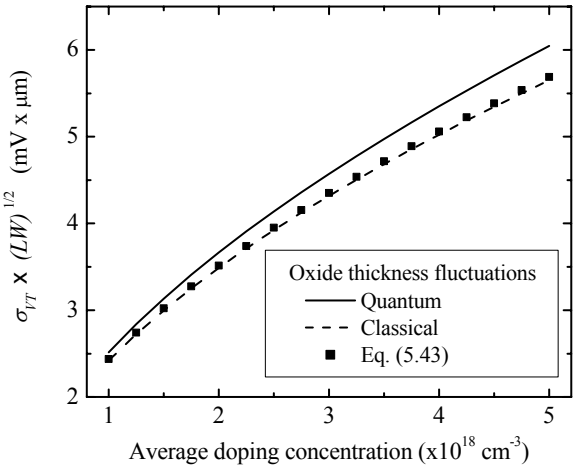

(a)

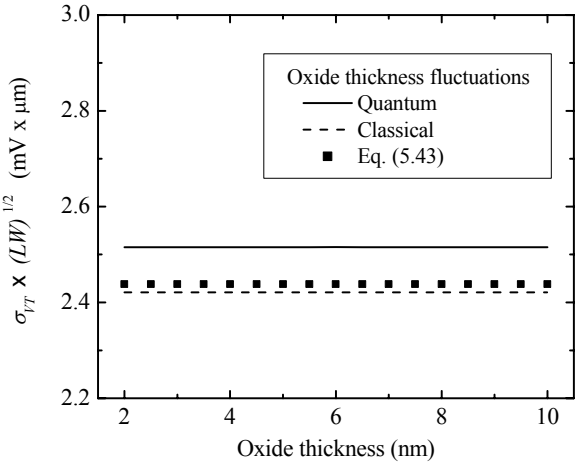

(b)

Figure 5.14: Standard deviation of threshold voltage as a function of average doping concentration (a) and oxide thickness (b) for a MOS capacitor (N_a = 10^{18} cm^{-3} and t = 4 nm). Only random oxide roughness induced fluctuations are considered in these simulations.

5.2.2 Quasi one-dimensional analysis

The model discussed in the previous section accurately describes the inversion regime in 1D-MOS structures (e.g. in MOS capacitors), but it does not capture short channel effects that exist in ultrasmall devices. In order to describe the inversion regime in short channel devices, one should solve both the Schrödinger and the Poisson equations in two or three dimensions. Although a few attempts to solve these equations for the multidimensional case have been made recently [127], [130]-[132], the computational cost is prohibitively high and approximate methods are preferred. Such a method, which can be applied to systems in which the electric potential does not vary significantly over a de Broglie wavelength in two directions, but can vary relatively fast in the third direction, is the quasi-1D method [133]. This method has the advantage that it avoids solving the Schrödinger equation in a multidimensional space, while capturing the main quantization effects that exist in short channel devices. The quasi-1D method has previously been applied to the computation of electron concentrations in MOS capacitors and to the computation of I-V characteristics of MOSFET devices. In this section, we further develop this method to the computation of random doping and random oxide thickness induced fluctuations in MOSFET devices.

Consider the computation of fluctuations of threshold voltages in MOSFET devices. Threshold voltage is defined as the gate voltage at which the drain-to-source current is equal to $10^{-9}\frac{W}{L}$ for an applied potential on the drain of 10^{-3} V ("current definition"), where W and L are the width and the channel length of the device,

respectively. The relatively low value of the applied potential allows us to assume that the Fermi level in the semiconductor is approximately constant and equals its values at the metal contacts. This assumption simplifies the solution of the transport equations significantly. For example, if we use the drift-diffusion model to describe the carrier transport, the Poisson and Schrödinger equations decouple from the current continuity equations, which substantially decreases the total computational cost of computing the threshold voltage. In our simulations, the current continuity and Poisson equations are solved on a rectangular mesh by using the 2D finite discretization technique. The electron concentration is found by considering the grid lines normal to the semiconductor/oxide interface and by solving a set of 1D Schrödinger equations along these lines (see Figure 5.15). In consequence, the Jacobian matrix is semi-sparse, because electron concentration depends on the values of the electric potential only on the same grid line, but it does not depend on the values of the electric potential on other grid lines. This fact can be used to choose a linear solver, which is optimized for low memory overhead in semi-sparse matrix calculations.

To present the main idea of the computation of threshold voltage fluctuations, it is convenient to consider the transport equations in discretized form:

$$\boldsymbol{F}\left[\boldsymbol{\varphi}, \boldsymbol{n}(\boldsymbol{\varphi}), \boldsymbol{\psi}_n, \boldsymbol{\psi}_p, V_G, \boldsymbol{D}, \boldsymbol{t}\right] = 0, \tag{5.44}$$

where $\boldsymbol{F}$ is an operator that consists of $3N$ equations corresponding to the discretized Poisson and electron and hole current continuity equations, and N is the total number of mesh points. In equation (5.44), $\boldsymbol{\psi}_n$ and $\boldsymbol{\psi}_p$ are vectors whose components are equal to the mesh point values of the electron and hole quasi Fermi potentials, while $\boldsymbol{t}$

is a vector that consists of the mesh point values of the oxide thickness. By linearizing equation (5.44), we obtain:

$$\hat{\boldsymbol{J}}\tilde{\varphi}+\hat{\boldsymbol{F}}_{\psi_n}\tilde{\psi}_n+\hat{\boldsymbol{F}}_{\psi_p}\tilde{\psi}_p+\hat{\boldsymbol{F}}_{\boldsymbol{D}}\tilde{\boldsymbol{D}}+\boldsymbol{F}_{V_G}\tilde{V}_G+\hat{\boldsymbol{F}}_{\boldsymbol{t}}\tilde{\boldsymbol{t}}=0\,, \tag{5.45}$$

where $\hat{\boldsymbol{J}}$ is defined by formula (5.23), while $\boldsymbol{F}_{\psi_n}$ and $\boldsymbol{F}_{\psi_p}$ are the derivatives of $\boldsymbol{F}$ with respect to ψ_n and ψ_p, respectively.

The drain-to-source current can be written as a function of the electric potential, electron concentration and quasi Fermi potentials. Denoting this function by a linear operator $I\left(\varphi,n,\psi_n,\psi_p\right)$ and taking into consideration the fact that the drain-to-source current is constant at threshold voltage, we can write:

$$0=\left(I_{\varphi}+I_n\frac{dn}{d\varphi}\right)\tilde{\varphi}+I_{\psi_n}\tilde{\psi}_n+I_{\psi_p}\tilde{\psi}_p\,, \tag{5.46}$$

where I_{φ}, I_{ψ_n}, and I_{ψ_p} are the derivatives of I with respect to φ, ψ_n, and ψ_p, respectively. By using a mathematical reasoning similar to the one we used to obtain equation (5.34), we deduce the following equation for the fluctuations of threshold voltage:

$$\tilde{V}_T=-\frac{\boldsymbol{g}^t\cdot\hat{\boldsymbol{F}}_{\boldsymbol{D}}}{\boldsymbol{g}^t\cdot\boldsymbol{F}_{V_G}}\cdot\tilde{\boldsymbol{D}}-\frac{\boldsymbol{g}^t\cdot\hat{\boldsymbol{F}}_{\boldsymbol{t}}}{\boldsymbol{g}^t\cdot\boldsymbol{F}_{V_G}}\cdot\tilde{\boldsymbol{t}}\,, \tag{5.47}$$

where $\boldsymbol{g}$ is the solution of the following linear system of equations:

$$\left[\hat{\boldsymbol{J}}^t,\hat{\boldsymbol{F}}_{\psi_n}^t,\hat{\boldsymbol{F}}_{\psi_p}^t\right]\cdot\boldsymbol{g}=\begin{bmatrix}I_{\varphi}+I_n\dfrac{dn}{d\varphi}\\ I_{\psi_n}\\ I_{\psi_p}\end{bmatrix}. \tag{5.48}$$

The standard deviation of threshold voltage can be computed with formula (2.7).

Next, we analyze the fluctuations of threshold voltage in short channel MOSFET devices by using the quasi 1D method presented above. The device we simulated corresponds to the device labeled MOS C, which is described in the Appendix. The Poisson and current continuity equations were discretized on rectangular grids of 70x70 mesh points and threshold voltages were computed by using the "current definition" presented in the previous section. The Schrödinger equation was discretized on a set of 1D grid lines only in the region close to the semiconductor/oxide interface, where the quantum effects are significant [134]. Outside this region, the electron concentration was calculated by using classical statistics.

Figures 5.16 (a) and (b) present the sensitivity coefficients as functions of the location in the semiconductor device computed by using the Poisson-Schrödinger approach. The values of these sensitivity coefficients are very close to the ones computed by using the Density-Gradient model (see Figure 5.11), which suggests that the calibration of the DG model presented in Section 5.1.1 is accurate. We observe again that the effect of quantization is to slightly shift the distribution of sensitivity coefficients away from the interface.

Figures 5.17 (a) and (b) present the standard deviation of the threshold voltage induced by random doping fluctuations as a function of the average doping concentration and oxide thickness. There is a trade-off between the doping concentration and the thickness of the oxide layer in the design of fluctuations resistant structures. In order to decrease the fluctuations of threshold voltages, one

should decrease the oxide thickness [see Figure 5.17(b)]. However, the standard scaling rules require increasing the doping concentration in the channel, which leads to an increase of the fluctuations of threshold voltages [see Figure 5.17(a)]. In practical applications, one should use the optimum values of N_a and t_{ox} to minimize the fluctuations of threshold voltages.

Figures 5.18 (a) and (b) present the standard deviation of the threshold voltage induced by random oxide thickness fluctuations as a function of the doping concentration and oxide thickness. In these simulations, the autocorrelation function of oxide thickness fluctuations was considered to be exponential [see equation (2.35)], with autocorrelation length L_c = 10 nm and roughness Δ = 0.15 nm. Our computations show that $\sigma_{V_T}[OTF]$ can be approximated by a power low $\sigma_{V_T}[OTF] \sim N_a^{0.38}$ for both classical and quantum computations. The exponent 0.38 is slightly smaller than in the case of the 1D MOS capacitor and this accounts for the short channel effects in the device.

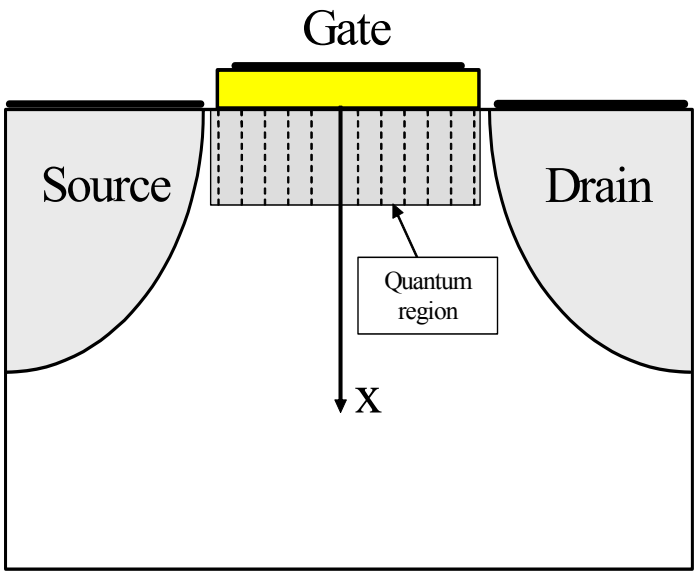

Figure 5.15: 2-D MOSFET device. The electron concentration inside the quantum region was computed by using a set of 1D Schrödinger equations. Outside the quantum region the electron concentration was calculated by using classical statistics.

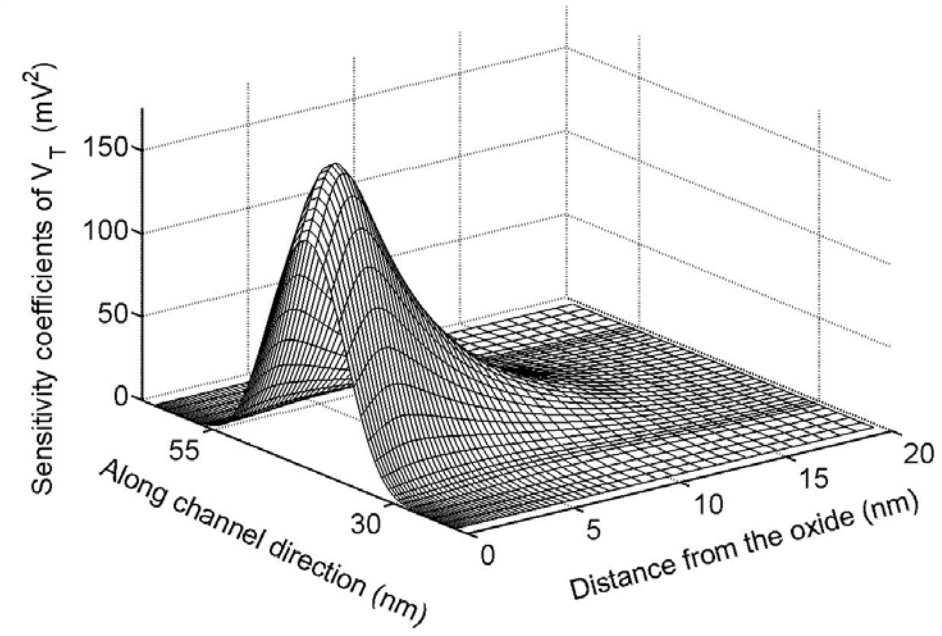

Figure 5.16: Sensitivity coefficients of threshold voltage for MOS C (see the Appendix for technical specifications) computed by using quasi-1D Poisson-Schrödinger computations. The metallurgical channel length extends from 30 nm to 55 nm in the "along channel" direction. Sensitivity coefficients have very close values to those computed by using the Density-Gradient model (see Figure 5.11).

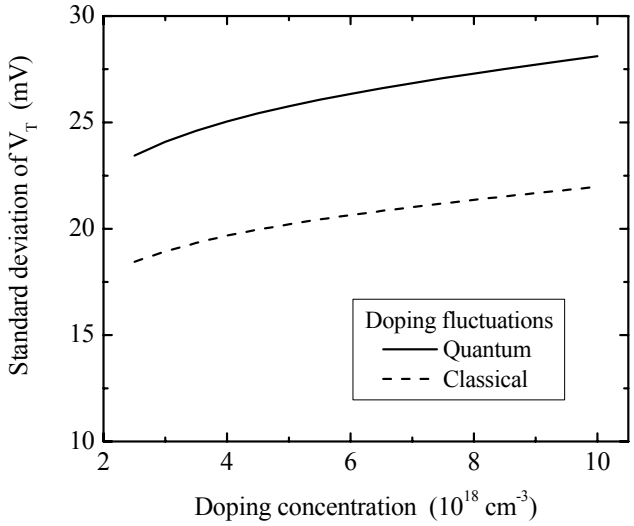

(a)

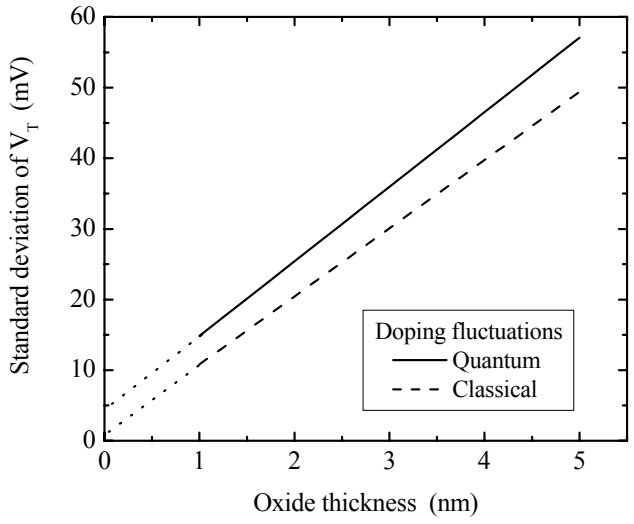

(b)

Figure 5.17: Threshold voltage standard deviation of MOS C as a function of average doping concentration (a) and oxide thickness (b). Only random doping induced fluctuations are considered in these simulations.

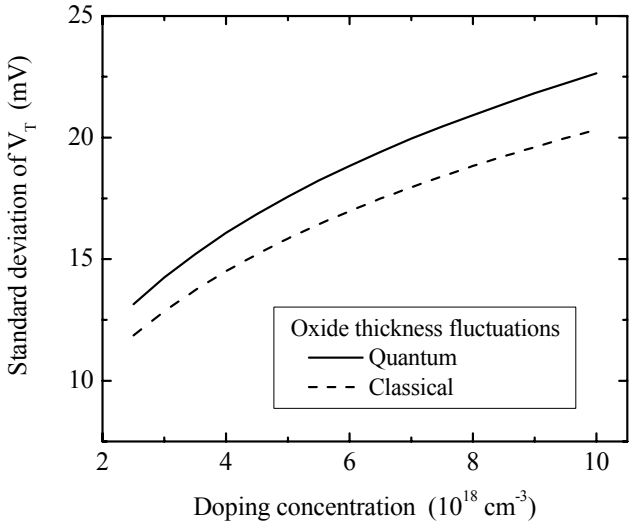

(a)

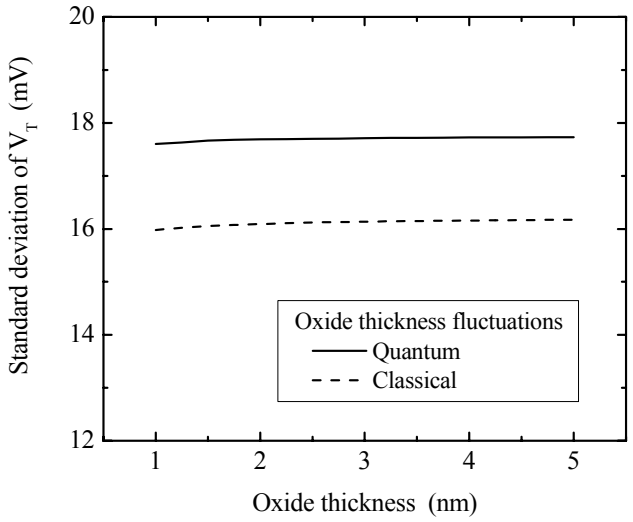

(b)

Figure 5.18: Threshold voltage standard deviation of MOS C as a function of average doping concentration (a) and oxide thickness (b). Only random oxide roughness induced fluctuations are considered in these simulations.

Chapter 6

Conclusions

Intrinsic parameter fluctuations have a negative impact on the reliability and yield of VLSI and ULSI circuits. Due to the aggressive reduction of the characteristic dimensions and to inaccuracies in the fabrication process, the parameters of ultrasmall semiconductor devices fluctuate significantly from one device to another. These fluctuations affect the functionality of the overall circuit and can make the final electronic product non-operational.

In this dissertation we performed a comprehensive analysis of fluctuations in semiconductor devices and a robust numerical technique for the characterization of random doping and random oxide roughness induced fluctuations and for the design of fluctuation-resistant structures. This technique is based on linearization of the transport equations with respect to the fluctuating quantities and completely circumvents extensive computations for numerous device realizations required by the traditional Monte-Carlo methods. For this reason, the proposed method is computationally much (i.e. a few orders of magnitude) more efficient than the Monte-

Carlo methods. For example, if the computational cost for calculating some parameter (e.g. threshold voltage, cut-off frequency, etc.) is about 20 minutes in a 3D simulation, the total computation time to accumulate statistics for a few hundred devices and to extract the standard deviation of that parameter by using the Monte-Carlo method is of the order of days. This computation time should be naturally compared to the total computation time required to compute the standard deviation by using the linearization method, which is approximately 2 minutes.

It has been demonstrated that the linearization technique provides information on the sensitivity of the parameters of interest (threshold voltage, small-signal parameters, cut-off frequencies, etc.) to the fluctuations of oxide thickness and doping concentration at different locations. Hence, this technique is instrumental in the design of doping and oxide thickness fluctuation-resistant structures. For example, it has been shown that most device parameters are particularly sensitive to the random doping fluctuations in the region located next to the oxide/semiconductor interface. Random doping fluctuations in this region induce large variations of threshold voltage and current characteristics, which can be reduced by using a low doping concentration layer (i.e. an epitaxial layer) in the conduction channel. By improving the doping profile in MOSFET devices, we can also reduce the fluctuations of small-signal parameters and cut-off frequencies. Similarly, in the case of oxide thickness fluctuations, threshold voltage is rather sensitive to the variations of thickness in the middle region of the oxide layer, but quite insensitive to edge variations of the oxide thickness. This effect can have positive implications for the fabrication process of the oxide layer, because etching and deposition of polysilicon usually deteriorates the

edges of the oxide, but do not affect too much the thickness of the middle part of the oxide layer.

The linearization technique has been applied to the analysis of fluctuations of threshold voltage, subthreshold, current, and frequency characteristics, as well as to the study of quantum induced effects on fluctuations in semiconductor devices. However, many areas of application have been left for future consideration and in-depth analysis. Following is a list of issues that need to be addressed in the near future:

(a) The linearization method has only been applied to the analysis of fluctuations in *n*MOSFETs and MOS capacitors. In the future we plan to apply this technique to other semiconductor devices, such as bipolar junction transistors (BJT), fin field-effect transistors (FinFET), silicon-on-insulator (SOI) devices, and high electron-mobility transistors (HEMT).

(b) Our analysis has so far concentrated on the fluctuations of admittance matrix elements and of *h* and *z*-parameters, gain factors, and cut-off frequencies. In the future this analysis should be extended to fluctuations of other small-signal parameters with more immediate practical use, such as drain resistance, source and gate capacitances.

(c) The present dissertation includes studies of mechanical induced effects on the fluctuations of threshold voltage. Future work should also address the influence of quantum effects on the current and frequency characteristics of semiconductor devices.

(d) The linearization method should be extended to the analysis of fluctuations induced by gate-polysilicon line edge roughness (LER). Such an analysis would

be the natural continuation of our study of random doping and oxide thickness induced fluctuations.

(e) It has been demonstrated that the linearization technique can be accurately applied to the analysis of fluctuations in semiconductor devices with characteristic dimensions larger than 20 nm (the channel length of the smallest MOSFET presented in the thesis was 25 nm, while the largest was about 1 μm). Future work should investigate to what extent the same linearization technique can be applied to smaller semiconductor devices (with channel length under 10 nm). Due to the very small device dimensions, we expect the linearization technique to fail to provide exact quantitative results and second order terms to be considered in the series expansion of transport equations.

The linearization technique is a powerful tool for the study of fluctuations in semiconductor devices. We hope that future developments and improvements will greatly extend its area of applicability and will make it an indispensable tool in both device and circuit design.

APPENDIX

Unless otherwise stated, the following *n*-channel MOSFET devices are analyzed in the thesis:

MOS A: This device has a very simplified structure that is similar to the one presented in Ref. [68]. The source and drain junctions are abrupt and the doping concentration in the channel and at the polysilicon gate is constant. The channel length and width are 50 nm, the oxide thickness is $t = 3$ nm, the doping concentration in the channel is $N_a = 5 \times 10^{18}$ cm^{-3}, the doping concentrations of the source and drain junctions are $N_d = 10^{20}$ cm^{-3}, while the electron and hole mobilities are assumed to be constant.

MOS B: This device has a more realistic structure that is similar to the retrograde model presented in Ref. [135]. The channel doping concentration decreases from $N_a = 5 \times 10^{18}$ cm^{-3} at $y_0 = 20$ nm (and deeper), to $N_a/10 = 5 \times 10^{16}$ cm^{-3} at the surface according to a truncated Gaussian distribution function (see Figure A). The source and drain profiles have a Gaussian distribution with a n-type peak surface concentration of 10^{20} cm^{-3} and vertical struggles

of about 8.2 nm that correspond to a junction depth of about 20 nm. The lateral source and drain struggles (in the directions parallel to the conduction channel) are about 1.34 nm and the source and drain extensions under the gate are 4.4 nm. The metallurgical channel length is 30 nm and this corresponds to an effective channel length of about 34 nm (the effective channel length is defined [135] by the points where the source-drain doping concentrations fall to $2\text{x}10^{19}$ cm^{-3}). The thickness of the oxide is 2 nm and the width of the device is 40 nm. In the reported simulations, one of the above parameters is usually varied, while the other ones are held constant. The electron and hole mobilities are described by the model presented in Ref. [89] and [90].

MOS C: The third device has a structure similar to MOS B but has slightly smaller dimensions. The channel doping concentration decreases from $N_a = 5\times10^{18}$ cm^{-3} at $y_0 = 15$ nm (and deeper) to $N_a/100 = 5\times10^{16}$ cm^{-3} at the surface, according to a truncated Gaussian distribution function (see Figure A). The source and drain profiles have a Gaussian distribution with a n-type peak surface concentration of 10^{20} cm^{-3} and vertical struggles of about 2.5 nm that correspond to junction depths of about 7 nm. The lateral source and drain struggles (in the directions parallel to the conduction channel) are about 1.05 nm and the source and drain extensions under the gate are 3.2 nm. The metallurgical channel length is 25 nm and this corresponds to an effective channel length of about 29.9 nm (the effective

channel length is defined [135] by the points where the source-drain doping concentrations fall to $2x10^{19}$ cm^{-3}). The thickness of the oxide is 2 nm and the width of the device is 50 nm. In the reported simulations, one of the above parameters is usually varied, while the other ones are held constant. The electron and hole mobilities are described by the model presented in Ref. [89] and [90].

Usually one of the characteristic dimensions of MOSFET devices is varied, while the others are kept constant.

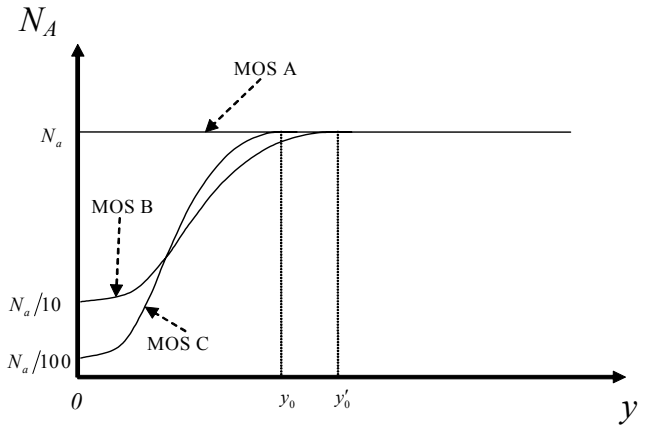

Figure A: Doping profiles for MOS A, MOS B, and MOS C.

PUBLICATIONS RELATED TO THE DISSERTATION

JOURNAL PUBLICATIONS

[1] **P. Andrei** and I. D. Mayergoyz, "Analysis of fluctuations in semiconductor devices through self–consistent Poisson–Schrödinger computations," submitted for publication to *J. Appl. Phys.*

[2] **P. Andrei** and I. D. Mayergoyz, "Quantum mechanical effects on random oxide thickness and doping fluctuations in ultra small semiconductor devices," *J. Appl. Phys*., vol. 94, pp. 7163-7172, Dec. 2003.

[3] **P. Andrei** and I. D. Mayergoyz, "Sensitivity of frequency characteristics of semiconductor devices to random doping fluctuations," *Solid-State Electron.*, vol. 48, pp. 133-141, Jan. 2004.

[4] **P. Andrei** and I. D. Mayergoyz, "Random doping-induced fluctuations of subthreshold characteristics in MOSFET devices," *Solid-State Electron.*, vol. 47, pp. 2055-2061, Nov. 2003.

[5] **P. Andrei** and I. D. Mayergoyz, "Analysis of random dopant-induced fluctuations of frequency characteristics of semiconductor devices," *J. Appl. Phys*., vol. 93, no. 8, pp. 4646-4652, April 2003.

[6] I. D. Mayergoyz and **P. Andrei**, "Numerical analysis of random dopant-induced effects in semiconductor devices," *Int. J. High Speed Electronics and Systems*, vol. 12, pp. 551-562, June 2002.

[7] I. D. Mayergoyz and **P. Andrei**, "Statistical analysis of semiconductor devices," *J. Appl. Phys*., vol. 90, no. 6, pp. 3019-3029, Sept. 2001.

[8] I. D. Mayergoyz, **P. Andrei**, and I. Filipovich, "Analysis of random dopant-induced effects through numerical solution of randomly perturbed nonlinear Poisson equation," *IEEE Trans. Magn*., vol. 37, no. 5, pp. 3155-3158, Sept. 2001.

PUBLICATIONS IN CONFERENCE PROCEEDINGS

[9] **P. Andrei** and I. D. Mayergoyz, "Analysis of fluctuations in ultra-small semiconductor devices," *2003 International Conference on Simulation of Semiconductor Processes and Devices (SISPAD)*, Boston MA, September3-5, 2003.

[10] I. D. Mayergoyz and **P. Andrei**, "Numerical analysis of random dopant-induced effects in semiconductor devices," *Workshop on Frontiers in Electronics (WOFE)*, St. Croix, Virgin Islands, January 6-11, 2002.

[11] I. D. Mayergoyz, **P. Andrei**, and I. Filipovich, "Analysis of random dopant-induced effects through numerical solution of randomly perturbed nonlinear Poisson equation," *IEEE Conference on Electromagnetic Field Computation (CEFC)*, Milwaukee WI, June 4-7, 2000.

BOOK CHAPTER

Co-author one chapter in *Handbook of Semiconductor Nanostructures and Devices*, to be published in multi-volumes by the American Scientific Publishers (2004).

REFERENCES

[1] "International roadmap for semiconductors (ITRS)," http://public.itrs.com, 2003 edition.

[2] P. J. Silverman, "The Intel lithography roadmap," http://developer.intel.com, pp. 55–61, 2002.

[3] R.W. Keys, "Physical limits in digital electronics," Proc. IEEE, vol. 63, pp. 740–766, 1975.

[4] Y. Taur, D. A. Buchanan, W. Chen, D. J. Frank, K. E. Ismail, S.–H. Lo, A. A. Sai–Hakasz, R. G. Viswanathan, H. J. C. Wann, S. J. Wind, and H.–S. Wong, "CMOS scaling into the nanometer regime," Proc. IEEE, vol. 85, pp. 486–504, Apr. 1997.

[5] D. J. Frank, R. H. Dennard, E. Nowak, P. M. Solomon, Y. Taur, and H.-S. P. Wong, "Device scaling limits of Si MOSFETs and their application dependencies," Proc. IEEE, vol. 89, no. 3, pp. 259–288, 2001.

[6] J. D. Plummer and P. B. Griffin, "Material and process limits in silicon VLSI technology," Proc. IEEE, vol. 89, no. 3, pp. 240–258, 2001.

[7] D. Hisamoto, "FD/DG–SOI MOSFET—a viable approach to overcoming the device scaling limit," IEDM Tech. Dig., 2001, pp. 429–532.

[8] D. J. Frank and Y. Taur, "Design considerations for CMOS near the limits of scaling," Solid–State Electron., vol. 46, pp. 315–320, 2002.

[9] R. W. Keyes, "Effect of randomness in the distribution of impurity ions on FET thresholds in integrated electronics," IEEE J. Solid–State Circuits, vol. SSC–10, pp. 245–247, 1975.

[10] T. Hagivaga, K. Yamaguchi, and S. Asai, "Threshold voltage variation in very small MOS transistors due to local dopant fluctuations," Proc. Sympp. VLSI Technol. Tech. Dig., 1982, pp. 46–47.

[11] T. Mikolajick and H. Ryssel, “Influence of statistical dopant fluctuations on MOS transistors with deep submicron channels,” Microelectron. Eng., vol. 21, pp. 419–433, 1993.

[12] T. Mizuno, M. Iwase, H. Niiyama, T. Shibata, K. Fujisaki, T. Nakasugi, A. Toriumi, and U. Ushiku, “Performance fluctuations 0.1 μm MOSFETs — Limitation of 0.1 μm ULSI’s,” Proc. VLSI Sympp., 1994, pp. 13–14.

[13] T. Mizuno, J. Okamura, and A. Toriumi, “Experimental study of threshold voltage fluctuation due to statistical variation of channel dopant number in MOSFETs,” IEEE Trans. Electron Devices, vol. 41, pp. 2216–2221, Nov. 1994.

[14] J.–R. Zhou and D. K. Ferry, “Three–dimensional simulation of the effect of random dopant distribution on conductance for deep submicron devices,” Proc. 3rd Int. Workshop on Comput. Electron.,New York, 1994, pp. 74–77.

[15] P. A. Stolk and D. B. M. Klaasen, “The effect of statistical dopant fluctuations on MOS device performance,” IEDM Tech. Dig., 1996.

[16] P. A. Stolk, F. P. Widdershoven, and D. B. M. Klaassen, “Device modeling of statistical dopant fluctuations in MOS transistors,” Proc. SISPAD, 1997, pp. 153–156.

[17] D. Vasileska, W. J. Gross, and D. K. Ferry, Modeling of deep–submicrometer MOSFETs: random impurity effects, threshold voltage shifts and gate capacitance attenuation, in Extended Abstracts IWCE–6, Osaka, pp. 259–262, 1998.

[18] A. Thean, M. Sadd, and B. White, “The effect of dopant granularity on superhalo–channel MOSFETs according two–dimensional and three dimensional computer simulations,” Proc. IEEE Silicon Nanoelectron. Workshop, Honolulu, HI, 2002, pp. 25–26.

[19] T. Ezaki, T. Ikezava, A. Notsu, K. Tanaka, and M. Hane, “3D MOSFET simulation considering long–range Coulomb potential effects for analysing statistical dopant induced fluctuations associated with atomistic process simulation,” Proc. SISPAD, 2002, pp. 91–94.

[20] T. H. Ning and C. T. Sah, “Effects of inhomogeneities of surface–oxide charges and the electron energy levels in a semiconductor surface–inversion layer,” Phys. Rev. B, vol. 9, pp. 527–535, 1974.

[21] S. M. Goodnick, D. K. Ferry, C.W.Wilmsen, Z. Liliental, D. Fathy, and O. L. Krivanek, “Surface roughness at the Si(100)–SiO2 interface,” Phys. Rev. B, vol. 32, pp. 8171–8186, 1985.

[22] T. Yoshinobu, A. Iwamoto, and H. Iwasaki, "Scaling analysis of SiO2/Si interface roughness by atomic force microscopy," Jpn. J. Appl. Phys., vol. 33, pp. 383-387, 1994.

[23] T. Yoshinobu, A. Iwamoto, K. Sudoh and H. Iwasaki, "Scaling of Si/SiO2 interface roughness" J. Vac. Sci. Technol. B, vol. 13, pp. 1630-1634, 1995.

[24] T. Yoshinobu, A. Iwamoto, K. Sudoh and H. Iwasaki, "Scaling analysis of a- and poly-Si surface roughness by atomic force microscopy," Mat. Res. Soc. Symp. Proc., vol. 367, pp. 329-334, 1995.

[25] R. M. Feenstra, M. A. Lutz, F. Stern, K. Ismail, P. M. Mooney, F. K. LeGoues, C. Stanis, J. O. Chu, and B. S. Meyerson, "Roughness analysis of Si/SiGe heterostructures," J. Vac. Sci. Tech. B, vol. 13, pp. 1608–1612, 1995.

[26] S. Yamakawa, H. Ueno, K. Taniguchi, C. Hamaguchi, K. Masali, and U. Ravioli, "Study of interface roughness dependence of electron mobility in Si inversion layers using Monte-Carlo method," J. Appl. Phys., vol. 79, pp. 911–916, 1996.

[27] D. Z.–Y. Ting, E. S. Daniel, and T. C. McGill, "Interface roughness effects in ultra–thin gate oxides," VLSI Des., vol. 8, pp. 47–51, 1998.

[28] A. Pirovano, A. L. Lacaita, G. Gidini, and G. Talarida, "On the correlation between surface roughness and inversion layer mobility in Si–MOSFETs," IEEE Electron Device Lett., vol. 21, pp. 34–36, Jan. 2000.

[29] E. Cassan, P. Dollfus, S. Galdin, and P. Hesto, "Calculation of direct tunnelling gate current through ultra–thin oxide and oxide/nitride stacks in MOSFETs and H–MOSFETs," Microel. Reliability, vol. 40, pp. 585–588, 2000.

[30] A. Asenov and S. Kaya, "Effect of oxide roughness on the threshold voltage fluctuations in decanano MOSFETs with ultrathin gate oxide," Proc. SISPAD, 2000, pp. 135–138.

[31] M. Koh,W. Mizubayashi, K. Ivamoto, H. Murakami, T. Ono, M. Tsuno, T. Mihara, K. Shibahara, S. Miyazaki, and M. Hirose, "Limit of gate oxide thickness scalling in MOSFETs due to apparent threshold voltage fluctuation introduced by tunneling leakage current," IEEE Trans. Electron Devices, vol. 48, pp. 259–264, 2001.

[32] A. Asenov, S. Kaya, and J. H. Davies, "Intrinsic threshold voltage fluctuations in decanano MOSFETs due to local oxide thickness variations," IEEE Trans. Electron Devices, vol. 49, pp. 112–119, Jan. 2002.

[33] S. Mori, T. Morisawa, N. Matsuzawa, Y. Kaimoto, M. Endo, T. Matsuo, K. Kuhara, and M. Sasago, "Reduction of line edge roughness in the top surface imaging process," J. Vac. Sci. Tech. B, vol. 16, pp. 3739–3743, 1998.

[34] T. Linton, M. Giles, and P. Packan, "The impact of line edge roughness on 100 nm device performance," Proc. Silicon Nanoelectronics Workshop, 1998, pp. 82.

[35] P. Oldiges, Q. Lin, K. Pertillo, M. Sanchez, M. Ieong, and M. Hargrove, "Modeling line edge roughness effects in sub 100 nm gate length devices," Proc. SISPAD, vol. 31, 2000.

[36] C. H. Diaz, H.–J. Tao, Y.–C. Ku, A. Yen, and K. Young, "An experimentally validated analytical model for gate line edge roughness (LER) effects on technology scaling," IEEE Electron Device Lett., vol. 22, pp. 287, June 2001.

[37] S. Kaya, A. R. Brown, A. Asenov, D. Magot, and T. Linton, "Analysis of statistical fluctuations due to line edge roughness in sub 0.1 μm MOSFETs," in Simulation of Semiconductor Processes and Devices, D. Tsoukalas and C. Tsamis, Eds. Vienna, Austria: Springer–Verlag, 2001, pp. 78–81.

[38] J.Wu, J. Chen, and K. Liu, "Transistor width dependence of LER degradation to CMOS device characteristics," Proc. SISPAD, Japan, 2002, pp. 95–98.

[39] S.–D. Kim, S. Hong, J.–K. Park, and J. C. S. Woo, "Modeling and analysis of gate line edge roughness effect on CMOS scaling toward deep nanoscale gate length," in Extended Abstracts Int. Conf. Solid–State Devices Materials, 2002, pp. 20–21.

[40] T. D. Linton, S. Yu, and R. Shaheed, "3D modeling of fluctuation effects in highly scaled VLSI devices," VLSI Des., vol. 13, pp. 103–109, 2002.

[41] A. Asenov, S. Kaya, and A. R. Brown, "Intrinsic parameter fluctuations in decananometer MOSFETs introduced by gate line edge roughness," IEEE Trans. Electron Devices, vol. 50, pp. 1254–1260, May 2003.

[42] K. S. Ralls, W. J. Skocpol, L. D. Jackel, R. E. Howard, L. A. Fetter, R. W. Epworth, and D. M. Tennant, "Discrete resistance switching in submicron silicon inversion layers: individual interface traps and low frequency (1/f) noise," Phys. Rev. Lett., vol. 52, pp. 228–231, 1984.

[43] M. J. Kirton and M. J. Uren, "Noise in solid state microstructures: a new perspective on individual defects, interface states and low frequency (1/f) noise," Adv. Phys., vol. 38, pp. 367–468, 1989.

[44] K. K. Hung, P. K. Ko, C. Hu, and Y. C. Cheng, "Random telegraph noise of deep–submicrometer MOSFETs," IEEE Electron Device Lett., vol. 11, pp. 90–92, Feb. 1990.

[45] E. Simoen, B. Dierickx, C. L. Claeys, and G. J. Declerck, "Explaining the amplitude of RTS noise in submicrometer MOSFETs," IEEE Trans. Electron Devices, vol. 39, pp. 422–429, Feb. 1992.

[46] Z. Shi, J.–P. Miéville, and M. Dutoit, "Random telegraph signals in deep submicron n–MOSFETs," IEEE Trans. Electron Devices, vol. 41, pp. 1161–1168, July 1994.

[47] M.–H. Tsai and T.–P. Ma, "The impact of device scaling on the current fluctuations in MOSFETs," IEEE Trans. Electron Devices, vol. 41, pp. 2061–2068, Nov. 1994.

[48] S. T. Martin, G. P. Li, E.Worley, and J. White, "The gate bias and geometry dependence of random telegraph signal amplitudes," IEEE Electron Device Lett., vol. 18, pp. 444–446, Sept. 1997.

[49] A. Godoy, F. Gámiz, A. Palma, J. A. Jiménez–Tejada, J. Banqueri, and J. A. López–Villanueva, "Influence of mobility fluctuations on random telegraph signal amplitude in n–channel metal–oxide–semiconductor field–effect transistors," J. Appl. Phys., vol. 82, pp. 4621–4628, 1997.

[50] H. H. Mueller and M. Schulz, "Random telegraph signal: an atomic probe of the local current in field–effect transistors," J. Appl. Phys., vol. 83, pp. 1734–1741, 1998.

[51] A. Asenov, R. Balasubramaniam, A. R. Brown, and J. H. Davies, "Effect of single–electron interface trapping in decanano MOSFETs: a. 3D atomistic simulation study," Superlattices Microstructures, vol. 27, pp. 411–416, 2000.

[52] H. M. Bu, Y. Shi, X. L. Yuan, Y. D. Zheng, S. H. Gu, H. Majima, H. Ishicuro, and T. Hiramoto, "Impact of the device scaling on the low frequency noise in n–MOSFETs," Appl. Phys. A, vol. 71, pp. 133–136, 2000.

[53] A. Asenov, R. Balasubramaniam, A. R. Brown, J. H. Davies, and S. Saini, "Random telegraph signal amplitudes in sub 100 nm (decanano) MOSFETs: a 3D 'atomistic' simulation study," IEDM Tech. Dig., 2000, pp. 279–282.

[54] A. Avellan, W. Krautschneider, and S. Schwantes, "Observation and modeling of random telegraph signals in the gate and drain currents of tunnelling metal–oxide–semiconductor field–effect transistors," Appl. Phys. Lett., vol. 78, pp. 2790–2792, 2001.

[55] A. R. Brown, A. Asenov, and J. R.Watling, "Intrinsic fluctuations in sub 10 nm double–gate MOSFETs introduced by discreteness of charge and matter," IEEE Trans. Nanotechnol., vol. 1, pp. 195–200, 2002.

[56] A. Asenov, R. Balasubramaniam, A. R. Brown, and J. H. Davies, "RTS amplitudes in decananometer MOSFETs: a 3D simulation study," IEEE Trans Electron Devices, vol. 50, pp. 839–845, Mar. 2003.

[57] K. R. Lakshmikumar, R. A. Hadaway, and M. A. Copeland, "Characterization and modeling of mismatch in MOS transistors for precision analogue design," IEEE J. Solid–State Circuits, vol. SC–21, pp. 1057–1066, 1986.

[58] M. Steyaert, J. Bastos, R. Roovers, P. Kinget, W. Sansen, B. Graindourse, A. Pergot, and E. Janssens, "Threshold voltage mismatch in short–channel MOS transistors," Electron. Lett., vol. 30, pp. 1546–1548, 1994.

[59] O. R. dit Buisson and G. Morin, "MOSFET matching in deep submicron technology," Proc. ESSDERC,G. Baccarani and M. Rudan, Eds., 1996, pp. 731–734.

[60] J. T. Horstmann, U. Hilleringmann, and K. F. Goser, "Matching analysis of deposition defined 50–nm MOSFETs," IEEE Trans. Electron Devices, vol. 45, pp. 299–306, Jan. 1998.

[61] D. Burnett, K. Erington, C. Subramanian, and K. Baker, "Implications of fundamental threshold voltage variations for high density SRAM and logic circuits," in VLSI Sympp. Tech Dig., 1994, pp. 15–16.

[62] M. Eisele, J. Berthold, R. Thewes, E.Wohlrabh, D. Schmitt–Landsiedel, and W. Weber, "Intra–die device parameter variations and their impact on digital CMOS gates at low supply voltages," IEDM Tech. Dig., 1995, pp. 67–70.

[63] A. Tanabe, M. Umetani, I. Fujiwara, T. Ogura, K. Kataoka, M. Okihara, H. Sakuraba, T. Endoh, and F. Masuoka, "0.18–μm CMOS 10–Gb/s Multiplexer/Demultiplexer ICs Using Current Mode Logic with Tolerance to Threshold Voltage Fluctuation," IEEE J, Solid State Circuits, vol. 36, pp. 988, 2001.

[64] H. P. Tuinhout, "Impact of parametric mismatch and fluctuations on performance and yield of deep–submicron CMOS technologies," Proc. ESSDERC, Florence, Italy, 2002, pp. 95–101.

[65] K. Nishinohara, N. Shigyo, and T. Wada, "Effects of microscopic fluctuations in dopant distributions of MOSFET threshold voltage," IEEE Trans. Electron Devices. vol. 39, no. 3, pp. 634–639, 1992.

[66] H.–S. Wong and Y. Taur, "Three dimensional 'atomistic' simulation of discrete random dopant distribution effects in sub–0.1 mm MOSFETs," IEDM Tech. Dig., 1993, pp. 705–708.

[67] A. Asenov, "Random dopant induced threshold voltage lowering and fluctuations in sub 0.1 μm MOSFETs: a 3D "atomistic" simulation study," IEEE Trans. Electron Devices, vol. 45, pp. 2505–2513, Dec. 1998.

[68] A. Asenov, A. R. Brown, J. H. Davies, and S. Saini, "Hierarchical approach to "atomistic" 3D MOSFET simulation," IEEE Trans. Comput.– Aided Des. Integrated Circuits Syst., vol. 18, pp. 1558–1565, Nov. 1999.

[69] D. J. Frank, Y. Taur, M. Ieong, and H.–S. P. Wong, "Monte-Carlo modeling of threshold variation due to dopant fluctuations," in Sympp. VLSI Technol. Dig., 1999, pp. 169–170.

[70] A. Asenov and S. Saini, "Polysilicon gate enhancement of the random dopant induced threshold voltage fluctuations in sub 100 nm MOSFETs with ultrathin gate oxides," IEEE Trans. Electron Devices, vol. 47, pp. 805–812, Apr., 2000.

[71] A. Asenov, G. Slavcheva, A. R. Brown, J. H. Davies, and S. Saini, "Increase in the random dopant induced threshold fluctuations and lowering in sub 100 nm MOSFETs due to quantum effects: a 3–D density–gradient simulation study," IEEE Trans. Electron Devices, vol. 48, pp. 722–729, Apr. 2001.

[72] J. T. Watt and J. D. Plummer, "Dispersion of MOS capacitance-voltage characteristics resulting from the random channel dopant ion distribution," IEEE Trans. Electron Devices, vol. 41, no. 11, pp. 2222–2232, 1994.

[73] I. D. Mayergoyz and P. Andrei, "Statistical analysis of semiconductor devices," J. Appl. Phys., vol. 90, no. 6, pp. 3019–3029, Sept. 2001.

[74] I. D. Mayergoyz, P. Andrei, and I. Filipovich, "Analysis of random dopant–induced effects through numerical solution of randomly perturbed nonlinear Poisson equation," IEEE Trans. Magn., vol. 37, no. 5, pp. 3155–3158, Sept. 2001.

[75] P. Andrei and I. D. Mayergoyz, "Analysis of random dopant–induced fluctuations of frequency characteristics of semiconductor devices," J. Appl. Phys., vol. 93, no. 8, pp. 4646–4652, April 2003.

[76] I. D. Mayergoyz and P. Andrei, "Numerical analysis of random dopant–induced effects in semiconductor devices," Int. J. High Speed Electronics and Systems, vol. 12, pp. 551–562, June 2002.

[77] P. Andrei and I. D. Mayergoyz, "Random doping–induced fluctuations of subthreshold characteristics in MOSFET devices," Solid–State Electron., vol. 47, pp. 2055–2061, Nov. 2003.

[78] P. Andrei and I. D. Mayergoyz, "Quantum mechanical effects on random oxide thickness and doping fluctuations in ultrasmall semiconductor devices," J. Appl. Phys., vol. 94, pp. 7163–7172, Dec. 2003.

[79] P. Andrei and I. D. Mayergoyz, "Sensitivity of frequency characteristics of semiconductor devices to random doping fluctuations," Solid–State Electron., vol. 48, pp. 133–141, Jan. 2004.

[80] P. Andrei and I. D. Mayergoyz, "Analysis of fluctuations in semiconductor devices through self–consistent Poisson–Schrödinger computations," submitted for publication to J. Appl. Phys.

[81] Y. Taur and T. H. Ning, Fundamentals of modern VLSI devices (Cambridge University Press, 1998).

[82] S. Selberherr, Analysis and simulation of semiconductor devices (Springer–Verlag, 1984).

[83] http://crd.lbl.gov/~xiaoye/SuperLU/, software for solving linear sparse systems of equations.

[84] http://www.computational.unibas.ch/cs/scicomp/software/pardiso/, software for solving linear sparse systems of equations.

[85] I. D. Mayergoyz, "Solution of the nonlinear Poisson equation of semiconductor device theory," J. Appl. Phys., vol. 59, no. 1, pp. 195–199, 1986.

[86] I. D. Mayergoyz, "A globally convergent algorithm for the solution of the steady-state semiconductor device equations," J. Appl. Phys., vol. 68, no. 3, pp. 1324–1334, 1990.

[87] Takeuchi, T. Tatsumi, and A. Furukawa, "Channel engineering for the reduction of random–dopant–placement–induced threshold voltage fluctuations," IEDM Tech. Dig., 1996.

[88] A. Asenov and S. Saini, "Suppression of random dopant induced threshold voltage fluctuations in sub–0.1 μm MOSFETs with epitaxial and doped channels," IEEE Trans. Electron Devices, vol. 46, pp. 1718–1723, 1999.

[89] D. B. M. Klaassen, "A unified mobility model for device simulation," Solid–State Electron., vol. 35, pp. 953-967, 1992.

[90] M. N. Darwish, J. L. Lentz, M. R. Pinto, P. M. Zeitzoff, J. Krutsick, and H. H. Vuong, An improved electron and hole mobility model for general purpose device simulation," IEEE Trans. Electron Devices., vol 44, pp. 1529-1538, Sept. 1997.

[91] J. R. Brews, "Sensitivity of subthreshold current to profile variations in long-channel MOSFETs," IEEE Trans. Electron Devices, vol. 43, no.12, pp. 2164–2171, 1996.

[92] J. R. Brews, "Surface potential fluctuations generated by interface charge inhomogeneities in MOS devices," J. Appl. Phys., vol. 43, pp. 2306–2313, 1972.

[93] R. S. Carson, High-frequency amplifiers (Wiley, New York, 1982).

[94] S. E. Laux, "Techniques for small-signal analysis of semiconductor devices," IEEE Trans. Electron Devices, vol. 32, pp. 2028–2037, 1985.

[95] A. Papoulis, Probability, random variables, and stochastic processes (McGraw-Hill, New York, 1984)

[96] M. G. Ancona and H. F. Tiersen, "Fully macroscopic description of bounded semiconductors with an application to the Si–SiO2 interface," Phys. Rev. B, vol. 27, no. 12, pp. 6104–6199, 1980.

[97] M. G. Ancona and H. F. Tiersen, "Fully macroscopic description of electrical conduction in metal–insulator–semiconductor structures," Phys. Rev. B, vol. 22, no. 12, pp. 7018–7045, 1983.

[98] M. G. Ancona and H. F. Tiersen, "Macroscopic physics of the silicon inversion layer," Phys. Rev. B, vol. 35, no. 15, pp. 7959–7965, 1987.

[99] M. G. Ancona and G. I. Iafrate, "Quantum correction to the equation of state of an electron gas in a semiconductor," Phys. Rev. B, vol. 39, pp. 9536–9540, 1989.

[100] C. S Rafferty, B. Biegel, Z.Yu, M.G. Ancona, J. Bude, and R.W. Dutton, "Multi–dimensional quantum effects simulation using a density–gradient model and script–level programming technique," Proc. SISPAD 1998, pp. 137–140.

[101] M. G. Ancona, "Equations of state for the silicon inversion layer," IEEE Trans. Electron Devices, vol. 47, no. 7, pp. 1449–1456, July 2000.

[102] M. G. Ancona, Z. Yu, R. W. Dutton, P. J. V. Voorde, M. Cao, and D. Vook, "Density–Gradient analysis of MOS tunneling," IEEE Trans. Electron Devices, vol. 47, pp. 2310, 2000.

[103] A. Wettstein, A. Schenk, and W. Fichtner, "Quantum device–simulation using the density–gradient model on unstructured grids," IEEE Trans. Electron Devices, vol. 48, pp. 279–284, Feb. 2001.

[104] D. Connelly, Z. Yu, and D. Yergeau, "Macroscopic simulation of quantum mechanical effects in 2–D MOS devices via the Density–Gradient method," IEEE Trans. Electron Devices, vol. 49, no. 4, pp. 619–626, April 2002.

[105] S. E. Laux and F. Stern, "Electron states in narrow gate–induced channels in Si," Appl. Phys. Lett., vol. 49, no. 2, pp. 91–93, 1986.

[106] http://www.netlib.org/lapack/, software for computing matrix eigenvalues and eigenvectors.

[107] F. Stern and W. E. Howard, "Properties of semiconductor surface inversion layer in the electric quantum limit," Phys. Rev., vol. 163, no. 3, pp. 816–838, 1967.

[108] T. Ando, A. B. Fowler, and F. Stern, "Electronic properties of two–dimensional systems," Rev. Mod. Phys., pp. 437–672, 1982.

[109] M. J. van Dort, P. H. Woerlee, A. J. Walker, C. A. H. Juffermans, and H. Lifka, "Quantum-mechanical threshold voltage shifts of MOSFET's caused by high levels of channel doping," IEDM Tech. Dig., 1991, pp. 495-498.

[110] M. J. van Dort, P. Woerlee, and A. Walker, "A simple model for quantization effects in heavily-doped silicon MOSFET's at inversion conditions," Solid-State Electron., vol. 37, pp. 411, 1994.

[111] A. Abou-Elnour and K. Schünemann, "Determination of electronic states in low dimensional heterostructure and quantum wire devices," in SISPAD Tech. Dig., 1995, pp. 178.

[112] S. Takagi and A. Toriumi, "Quantitative understanding of inversion layer capacitance in Si MOSFET's," IEEE Trans. Electron Devices, vol. 42, pp. 2125, 1995.

[113] K. Krisch, J. Bude, and L. Manchanda, "Gate capacitance attenuation in MOS devices with thin gate dielectrics," IEEE Electron Device Lett., vol. 17, pp. 521, 1996.

[114] S. A. Hareland, S. Krishnamurthy, S. Jallepalli,C. F. Yeap, K. Hasnat, A. F. Tasch, and C. M. Maziar, "A computationally efficient model for inversion layer quantization effects in deep submicron n-channel MOSFET's," IEEE Trans. Electron Devices, vol. 43, pp. 90-96, 1996.

[115] C. Bowen, C. Fernando, G. Klimeck, A. Chatterjee, D. Blanks, R. Lake, J. Hu, J. Davis, M. Kulkarni, S. Hattangady and I-H Chen, "Physical oxide thickness extraction and verification using quantum mechanical simulation," IEDM Tech. Dig., 1997, pp. 869-872.

[116] S. Jallepalli, J. Bude, W.-K. Shih, M. R. Pinto, C. M. Maziar, A. F. Tasch, "Electron and hole quantization and their impact on deep submicron p- and n-MOSFET characteristics," IEEE Trans. Electron Devices, vol. 44, pp. 297–303, 1997.

[117] S.-H. Lo, D. Buchanan, Y. Taur, and W. Wang, "Quantum-mechanical modeling of electron tunneling current from the inversion layer of ultrathin-oxide nMOSFET's," IEEE Electron Device Lett., vol. 18, pp. 209, 1997.

[118] B. Ip and J. Brews, "Quantum effects upon drain current in a biased MOSFET," IEEE Trans. Electron Devices, vol. 45, pp. 2213, 1998.

[119] C. Fiegna and A. Abramo, "Analysis of quantum effects in nonuniformly doped MOS structures," IEEE Trans. Electron Devices, vol. 45, pp. 877, 1998.

[120] W. Magnus and W. Schoenmaker, "Full quantum mechanical treatment of charge leakage in MOS capacitors with ultra-thin oxide layers," in ESSDERC Tech. Dig., 1999, pp. 248.

[121] F. Stern, "Iteration methods for calculating self-consistent fields in semiconductor inversion layers," J. Comput. Phys., vol. 6, pp. 56–67, 1970.

[122] J. Suňé, P. Olivo, and B. Riccó, "Iteration methods for calculating self-consistent fields in semiconductor inversion layers," J. Appl. Phys. vol. 70, pp. 337-345, 1991.

[123] A. Kumar, S. E. Laux, and F. Stern, "Electron states in a GaAs quantum dot in magnetic field," Phys. Rev. B., vol. 42, no. 8, pp. 5166–5175, 1990.

[124] A. Pacelli, "Self-consistent solution of the Schrödinger equation in semiconductor devices by implicit iteration," IEEE Trans. Electron Devices, vol. 44, pp. 1169-1171, 1997.

[125] A. Trellakis, A. T. Galick, A. Pacelli, and U. Ravaioli, "Iteration scheme for the solution of the two-dimensional Schrödinger-Poisson equations in quantum structures," J. Appl. Phys., vol. 81, no. 12, pp. 7880–7884, 1997.

[126] A. Trellakis, A. T. Galick, and U. Ravaioli, "Rational Chebyshev approximation for the Fermi-Dirac integral F(-3/2)," Solid-State Electron., vol. 21, no. 5, pp. 771–773, 1997.

[127] Abramo A., Cardin A., Selmi L, and Sangiorgi E., "Two-dimensional quantum mechanical simulation of charge distribution in silicon MOSFETs," IEEE Trans. Electron Devices., vol. 47, pp. 1858–1862, 2000.

[128] X. Aymerich-Humet, F. Serra-Mestres, and J. Millan, "An analytical approximation for the Fermi–Dirac integral F(3/2)," Solid State-Electron., vol. 24, pp. 981, 1981.

[129] V. C. Aguilera-Navarro, G. A. Estevez, and A. Kostecki, "A note on the Fermi-Dirac integral function," J. Appl. Phys., vol. 63, no. 8, pp. 2848–2850, 1988.

[130] M. Fischetti and S. Laux, "Monte-Carlo study of electron transport in silicon inversion layers," Phys. Rev. B, vol. 48, pp. 2244, 1993.

[131] A. Spinelli, A. Benvenuti, and A. Pacelli, "Self-consistent 2-D model for quantum effects in n-MOS transistors," IEEE Trans. Electron Devices, vol. 45, pp. 1342, 1998.

[132] C. S. Rafferty, B. Biegel, Z. Yu, M. G. Ancona, J. Bude, and R. W. Dutton "Multi-dimensional quantum effect simulation using a density-gradient model and script-level programming techniques," in SISPAD Tech. Dig., 1998, pp. 137-140.

[133] B. Winstead; and U. Ravaioli, "A quantum correction based on Schrodinger equation applied to Monte-Carlo device simulation," IEEE Trans. Electron Devices, vol. 50, pp. 440-446, 2003.

[134] A. Pirovano, A. L. Lacaita, and A. S. Spinelli, "Two-dimensional quantum effects in nanoscale MOSFETs," IEEE Trans. Electron Devices, vol. 49, no. 1, pp. 25-31, 2002.

[135] Y. Taur, C. H. Wann, and D. J. Frank, "25 nm CMOS considerations," IEDM Tech. Dig., 1998, pp. 789–792.

PETRU ANDREI

EDUCATION

Ph.D., Electrical Engineering, May 2004
University of Maryland, College Park, USA
Overall GPA = 4.0

- Major/minor: electrophysics/microelectronics
- Research Assistant (Department of Electrical and Computer Engineering, January 2000–May 2004)
- Teaching Assistant (Department of Physics, "Quantum Physics," Fall 1999)

M.S., Physics, June 1999
Alexandru Ioan Cuza University, Iasi, Romania
Overall GPA = 4.0

- Major: electricity and magnetism

B.S., Physics, June 1997
Alexandru Ioan Cuza University, Iasi, Romania
Overall GPA = 4.0

FELLOWSHIPS AND HONORS

- Distinguished Graduate Research Assistant, Department of Electrical and Computer Engineering, University of Maryland, College Park, USA, June 2000–present
- Valedictorian of the 1999 (M.S. degree) and 1997 classes (B.S. Degree)
- Socrates Fellowship, Technical University of Vienna, Austria, March–May 1999
- Tempus Fellowship, Paris-Sud University, Orsay, France, March–May 1997
- Scholarship for academic excellence, Alexandru Ioan Cuza University, Iasi, Romania, September 1993–June 1999

MISCELLANEOUS

- Served as reviewer for the Journal of Applied Physics and Applied Physics Letters
- IEEE, Student Member

DISSERTATIONS

- **Ph.D. Dissertation**:

"Analysis of fluctuations in semiconductor devices", University of Maryland, College Park.

- **M.S. Dissertations**:

"Magnetization processes in micro- and nano-particule systems," Alexandru Ioan Cuza University, Iasi, Romania, pp. 1-101, 1999.

"Energetic model of magnetic hysteresis. Exact calculations and identification methods," Technical University of Vienna, Austria, pp. 1-78, 1999.

- **B.S. Dissertations:**

"Phenomenological models for the study of magnetization processes of ferromagnetic and ferritic materials," Alexandru Ioan Cuza University, Iasi, Romania, pp. 1-250, 1999.

"Proprietes physiques des couches minces magnetiques: une revue theorique et une etude experimentale d'une couche mince de permalloy" (in French), Paris-Sud University, Paris, France, pp. 1-72, 1997.

PUBLICATIONS IN JOURNALS

[1] **P. Andrei** and I. D. Mayergoyz, "Analysis of fluctuations in semiconductor devices through self-consistent Poisson- Schrödinger computations," submitted for publication to *J. Appl. Phys.*

[2] **P. Andrei** and I. D. Mayergoyz, "Quantum mechanical effects on random oxide thickness and doping fluctuations in ultra small semiconductor devices," *J. Appl. Phys*., vol. 94, pp. 7163-7172, Dec. 2003.

[3] **P. Andrei** and I. D. Mayergoyz, "Sensitivity of frequency characteristics of semiconductor devices to random doping fluctuations," *Solid-State Electron.*, vol. 48, pp. 133-141, Jan. 2004.

[4] **P. Andrei** and I. D. Mayergoyz, "Random doping-induced fluctuations of subthreshold characteristics in MOSFET devices," *Solid-State Electron.*, vol. 47, pp. 2055-2061, Nov. 2003.

[5] **P. Andrei**, M. Dimian, C. Krafft, I. D. Mayergoyz, D. I. Mircea, and R. Rojas, "Anisotropy characterization of garnet films by using VSM measurements," *J. Appl. Phys*., vol. 93, no. 10, pp. 7065-7067, May 2003.

[6] I. D. Mayergoyz, **P. Andrei**, and M. Dimian, "Nonlinear magnetostatic calculations based on fast multipole method," *IEEE Trans. Magn,* vol. 39, no. 3, pp. 1103-1106, May, 2003.

[7] **P. Andrei** and I. D. Mayergoyz, "Analysis of random dopant-induced fluctuations of frequency characteristics of semiconductor devices," *J. Appl. Phys*., vol. 93, no. 8, pp. 4646-4652, April 2003.

[8] I. D. Mayergoyz, C. Tse, C. Krafft, D. I. Mircea, and **P. Andrei**, "Extraction of the response function of GMR head for spin-stand imaging," *IEEE Trans. Magn*., vol. 38, no. 5, pp. 2453-2455, Sept. 2002.

[9] I. D. Mayergoyz and **P. Andrei**, "Numerical analysis of random dopant-induced effects in semiconductor devices," *Int. J. High Speed Electronics and Systems*, vol. 12, pp. 551-562, June 2002.

[10] I. D. Mayergoyz and **P. Andrei**, "Preisach modeling of clockwise hysteresis and its application to front propagation problems," *J. Appl. Phys*., vol. 91, no. 10, pp. 7645-7647, May 2002.

[11] C. Tse, D. I. Mircea, I. D. Mayergoyz, and **P. Andrei**, "Spatial and vectorial characterization of thermal relaxation using the spin-stand imaging technique," *J. Appl. Phys*., vol. 91, no. 10, pp. 8846-8848, May 2002.

[12] I. D. Mayergoyz, **P. Andrei**, and B. Hakim, "A new time-domain approach to the analysis of scattering problems," *IEEE Trans. Magn*., vol. 38, no. 2, pp. 327-332, March 2002.

[13] I. D. Mayergoyz and **P. Andrei**, "Statistical analysis of semiconductor devices," *J. Appl. Phys*., vol. 90, no. 6, pp. 3019-3029, Sept. 2001.

[14] I. D. Mayergoyz, **P. Andrei**, and I. Filipovich, "Analysis of random dopant-induced effects through numerical solution of randomly perturbed nonlinear Poisson equation," *IEEE Trans. Magn*., vol. 37, no. 5, pp. 3155-3158, Sept. 2001.

[15] O. Caltun, **P. Andrei**, and Al. Stancu, "Modeling the temperature dependence of magnetization processes in soft ferrite cores," *Int. J. Appl. Electrom.,* vol. 13, no. 4, pp. 335-338, 2001.

[16] R. Grossinger, H. Hauser, L. Stoleriu, and **P. Andrei**, "Hysteresis modeling of anisotropic barium ferrite," *IEEE Trans. Magn*., vol. 36, no. 5, pp. 3357-3359, Sept. 2000.

[17] **P. Andrei**, L. Laurentiu, and H. Hauser, "Hysteresis model identification for particulate media," *J. Appl. Phys*., vol. 87, no. 9, pp. 6555-6557, May 2000.

[18] **P. Andrei** and Al. Stancu, "Identification method analysis for the scalar generalized moving Preisach model using major hysteresis loops," *IEEE Trans. Magn*., vol. 36, no. 4, pp. 1982-1989, July 2000.

[19] **P. Andrei** and Al. Stancu, "Hysteresis in particulate recording media. Experiment and simulation with Preisach and Jiles-Atherton models," *J. Magn. Mag. Mat.*, vol. 206, pp. 160-164, 1999.

[20] **P. Andrei**, O. Caltun, C, Papusoi, Al. Stancu, and M. Feder, "Losses and magnetic properties of Bi2O3 doped MnZn ferrites," *J. Magn. Mag. Mat.*, vol. 196-197, pp. 362-364, 1999.

[21] **P. Andrei**, Al. Stancu, and O. Caltun, "Differential Preisach model for the description of dynamic magnetization processes," *J. Appl. Phys*., vol. 83, no. 11, pp. 6359-6361, June 1998.

[22] **P. Andrei**, O. Caltun, and Al. Stancu, "Differential phenomenological models for the magnetization processes in soft MnZn ferrites," *IEEE Trans. Magn*., vol. 34, no. 1, pp. 231-241, Jan. 1998.

[23] Al. Stancu, O. Caltun, and **P. Andrei**, "Models of hysteresis in magnetic cores," *J. Phys. IV*, vol. 7, pp. 209-210, 1997.

PUBLICATIONS IN CONFERENCE PROCEEDINGS

[24] **P. Andrei** and I. D. Mayergoyz, "Analysis of fluctuations in ultra-small semiconductor devices," *Proc. of SISPAD 2003*, IEEE Electron Society, pp. 95-98, 2003.

[25] O. Caltun, **P. Andrei**, and Al. Stancu, "Initial permeability, hysteresis and total losses measurements," *Proc. of MMDE'01*, Bucharest, Romania, pp. 99-102, 2001.

[26] **P. Andrei**, Al. Stancu, and O. Caltun, "Reversible and irreversible magnetisation processes in phenomenological models," *Proc. of ISEM'99 (International Symposium on Non-Linear Electromagnetic Systems)*, IOS Press, pp. 129-132, 1999.

[27] O. Caltun, Al. Stancu, C. Papusoi, and **P. Andrei**, "On the distortions in RL circuits with fine-grained MnZn ferrite cores," *Proc. of ISEM'99 (International Symposium on Non-Linear Electromagnetic Systems),* IOS Press, pp. 31-34, 1999.

[28] O. Caltun, C. Papusoi, Al. Stancu, and **P. Andrei**, "ME sensor based on electron diffusion in low electric resistive ferrites," *Proc. of ISEM'99 (International Symposium on Non-Linear Electromagnetic Systems)*, IOS Press, pp. 637-640, 1999.

[29] O. Caltun, C. Papusoi, Al. Stancu, and **P. Andrei**, "Spectral analysis of the induced signal in RL circuits with ferrite cores," *Proc. of MMDE'99*, Bucharest, Romania, pp. 77-84, 1999.

[30] **P. Andrei**, L. Stoleriu, Al. Stancu, and H. Hauser, "Hysteresis simulation for particle assemblies using the Preisach and the energetic models," *Proc. of CCMP'99*, Timisoara, Romania, P2-55, pp. 97, 1999.

[31] **P. Andrei**, O. Caltun, and Al. Stancu, "On the modeling of temperature dependent magnetization processes in soft ferrite," *Proc. of CCMP'99*, Timisoara, Romania, P2-56, pp. 98, 1999.

[32] O. Caltun, C. Papusoi, Al. Stancu, and **P. Andrei**, "Correlation between magnetization processes in soft ferrite cores and amplitude spectra of induced signals," *Proc. of CCMP'99*, Timisoara, Romania, O1-5, pp. 16, 1999.

[33] O. Caltun, M. Tasca, M. Feder, Al. Stancu, and **P. Andrei**, "The influence of milling time on the microstructure and on the magnetic properties of some Mn-Zn ferrites*," Proc. of CCMP'99*, Timisoara, Romania, P1-65, pp. 60, 1999.

[34] Al. Stancu, **P. Andrei**, and O. Caltun, "Simulation of non-linear inductor circuits in phenomenological models," *Non-linear electromagnetic systems - Advanced techniques and mathematical methods*, IOS Press, pp. 503-505, 1998.

[35] O. Caltun, Leonard Spinu, **P. Andrei**, and Al. Stancu, "Fundamental frequency influence on harmonic content of circular Barkhausen effect induced signal," *Non-linear electromagnetic systems - Advanced techniques and mathematical methods*, IOS Press, pp. 547-549, 1998.

[36] O. Caltun, C. Papusoi, Al. Stancu, **P. Andrei**, and W. Kappel, "Magnetic cores diagnosis," *Non-linear electromagnetic systems - Advanced techniques and mathematical methods*, IOS Press, pp. 594-596, 1998.

BOOK CHAPTER

Co-author one chapter in *Handbook of Semiconductor Nanostructures and Devices*, to be published in multi-volumes by the American Scientific Publishers (2004).

CONFERENCES, TALKS, AND PRESENTATIONS

[1] *The 2003 IEEE International Conference on Simulation of Semiconductor Processes and Devices*, Boston, MA, September 3-5, 2003.

[2] *The 14th Conference on Computation of Electromagnetic Fields*, Saratoga Springs, NY, July 13-17, 2003.

[3] *The 47th Annual Conference on Magnetism and Magnetic Materials*, Tampa FL, November 11-15, 2002.

[4] *The 10th Biennial IEEE Conference on Electromagnetic Field Computation*, Perugia, Italy, June 16-19, 2002.

[5] *The INTERMAG 2003*, Amsterdam, Netherlands, April 28-May 2, 2002.

[6] *The 2002 Workshop on Frontiers in Electronics*, St. Croix, Virgin Islands, USA, January 6-11, 2002.

[7] *The 46th Annual Conference on Magnetism and Magnetic Materials*, Seattle WA, November 12-16, 2001.

[8] *The 1st International Conference on Spintronics and Quantum Information Technology,* Maui HI, May 15-18, 2001.

[9] *The 10th International Symposium on Non-Linear Electromagnetic Systems*, Tokyo, Japan, May 14-16, 2001.

[10] *The INTERMAG 2000*, Toronto, Canada, April 9-13, 2002.

[11] *The 9th Biennial IEEE Conference on Electromagnetic Field Computation*, Milwaukee, WI, June 4-7, 2000.

[12] *The 44th Annual Conference on Magnetism and Magnetic Materials*, San Jose CA, November 15-18, 1999.

[13] *The 3rd Conference on Condensed Matter Physics*, Timisoara, Romania, September 17-19, 1999.

[14] *The 9th International Symposium on Non-Linear Electromagnetic Systems*, Pavia, Italy, May 10-12, 1999.

[15] *The 7th Joint MMM-INTERMAG Conference*, San Francisco CA, USA, January 6-9, 1998.

[16] *The 3rd General Conference of the Balkan Physical Union*, Cluj-Napoca, Romania, September 2-5, 1997.

[17] *The 8th International Symposium on Non-Linear Electromagnetic Systems*, Braunschweig, Germany, May 12-14, 1997.

[18] *The 7th International Conference on Ferrite*, Bordeaux, France, September 3-6, 1996.